

Important Notice

This copy may be used only for the purposes of research and private study, and any use of the copy for a purpose other than research or private study may require the authorization of the copyright owner of the work in question. Responsibility regarding questions of copyright that may arise in the use of this copy is assumed by the recipient.



View towards southwest from Wildcat Hills.

THE UNIVERSITY OF CALGARY

Geophysical Investigation of the Triangle Zone Structure
in the Jumpingpound-Wildcat Area,
Southern Alberta Foothills

by

Robin Tage Slotboom

A THESIS

SUBMITTED TO THE FACULTY OF GRADUATE STUDIES
IN PARTIAL FULFILLMENT OF THE REQUIREMENTS FOR THE
DEGREE OF MASTER OF SCIENCE

DEPARTMENT OF GEOLOGY and GEOPHYSICS

CALGARY, ALBERTA

OCTOBER, 1992

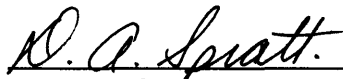
© Robin Tage Slotboom 1992

THE UNIVERSITY OF CALGARY
FACULTY OF GRADUATE STUDIES

The undersigned certify that they have read, and recommend to the Faculty of Graduate Studies for acceptance, a thesis entitled, "Geophysical Investigation of the Triangle Zone Structure in the Jumpingpound-Wildcat Area, Southern Alberta Foothills", submitted by Robin Tage Slotboom in partial fulfillment of the requirements for the degree of Master of Science.



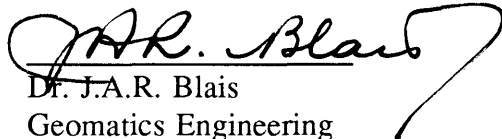
Supervisor, Dr. D.C. Lawton
Geology and Geophysics



Dr. D.A. Spratt
Geology and Geophysics



Dr. R.J. Brown
Geology and Geophysics



Dr. J.A.R. Blais
Geomatics Engineering

October 6, 1992

Abstract

Balanced vertical geological cross-sections, constrained by abundant seismic, well, and surface data from the Jumpingpound-Wildcat Hills area, show the triangle zone to be a NW-SE trending antiformal stack of duplexes involving Cretaceous rocks that have been forced eastward into foreland strata between two bedding-parallel detachments. The lower of these detachments carries carbonate rocks of Mississippian age in its hanging wall. It rises from a flat near the base of the Banff Formation, and flattens out beneath the Edmonton Group, near the top of the Belly River Formation. The upper detachment rides within the Edmonton Group, and the two detachments are not observed to merge at a simple branch point near the triangle zone. Gravity data acquired in the area have a subtle, but identifiable response to the carbonate rocks that have been thrust into the clastic sedimentary section.

Acknowledgements

Many thanks go to Dr. D.C. Lawton for his support, guidance, and encouragement in his supervision of this work. Dr. R.R. Stewart and Dr. R.J. Brown of the CREWES project are thanked for their feedback and input into my foray into elastic-wave seismology. Dr. D.A. Spratt and Dr. P. MacKay are thanked for sharing their insight into the triangle zone.

Mssrs. Eric Gallant, Carl Gunhold, Jon Greggs, Dave Harvey, and in particular, Mr. Malcom Bertram are thanked for the assistance that they have provided in the acquisition and processing of the various data used in this study. Dr. S. Cheadle is thanked for the use of his beam steering program.

Chevron Canada Resources and Shapiro Management are thanked for the release of data used in this study.

My colleagues in the halls of the graduate studenthood are thanked for sharing their enthusiasm for learning as well as for the various shared amusements that made working the long hours of graduate school more fun.

I thank my family for their support and encouragement, and most importantly, special thanks to Ninna for helping me and for putting with me in the completion of this thesis.

To Ninna,
to Christian,
and to any more that may come.

Table of Contents

Title Page	i
Approval Page	ii
Abstract	iii
Acknowledgements	iv
Dedication	v
Table of Contents	vi
List of Tables	viii
List of Figures	ix
Chapter 1 Introduction	1
1.1 Introduction	1
1.2 Objectives	2
1.3 Methodology	4
1.4 Database	4
Chapter 2 Geological Review	7
2.1 Regional Geological Setting	7
2.2 Study Area	8
2.3 Review of the Triangle Zone	12
2.4 Previous Structural Interpretations	16
Chapter 3 Seismic Data Processing	21
3.1 Introduction	21
3.2 Acquisition	21
3.3 Processing - General	29
3.4 Preliminary Processing	33
3.5 Static Corrections	35
3.6 Beam Steering	37
3.7 NMO and Residual Static Corrections	40
3.8 Imaging	42

Chapter 4 Seismic Interpretation	44
4.1 Introduction	44
4.2 Line CX91	44
4.3 Line 12X	49
4.4 Line 18XC	53
4.5 Line FS86-3 and FS84-1	56
4.6 Line FS86-1	58
4.7 Line FS85-1	61
4.8 Line FS86-2	61
4.9 Pull-up Anomalies	66
 Chapter 5 Gravity Analysis	 68
5.1 Introduction	68
5.2 Study Area Density Values	69
5.3 Fieldwork Description	69
5.4 Gravity Reduction	70
5.5 Anomaly Isolation	77
5.6 Interpretation	78
5.7 Error Analysis	81
5.8 Discussion	82
 Chapter 6 Structural Interpretation	 83
6.1 Introduction	83
6.2 Structure	83
6.3 Discussion	93
 Chapter 7 Conclusions	 96
 References	 98
 Appendix I - Gravity Data	 102

List of Tables

Table 3.1	Acquisition parameters of Line FS86-2.	23
Table 3.2	Acquisition parameters of Line FS85-1.	23
Table 3.3	Acquisition parameters of Line CX91.	24
Table 3.4	Acquisition parameters of Line 18XC.	24
Table 3.5	Acquisition parameters of Line 12X.	25
Table 3.6	Acquisition parameters FS86-2.	25
Table 3.7	General processing flow	32
Table 5.1	Gravity profile data analysis sequence.	70

List of Figures

Figure 1.1	Location Map.	3
Figure 1.2	Seismic and gravity database.	6
Figure 2.1	Table of formations.	9
Figure 2.2	Geological map of the study area.	13
Figure 2.3	Triangle zone schematic cross section.	14
Figure 2.4	Charlesworth (1985) model.	15
Figure 2.5	Jones (1982) model	15
Figure 2.6	Fox interpretation of Jumpingpound	17
Figure 2.7	Ollerenshaw interpretation of Jumpingpound	18
Figure 2.8	Jones interpretation of Jumpingpound	19
Figure 3.1	Unfiltered shot records	26
Figure 3.2	Constraints upon recordable dip.	28
Figure 3.3	Image degradation due to an inadequate aperture.	30
Figure 3.4	Image degradation due to spatial aliasing	31
Figure 3.5	Filtered shot records.	34
Figure 3.6	Improvement given by the static corrections.	36
Figure 3.7	Beam steering example	39
Figure 3.8	Difference records	41
Figure 3.9	F-X filtering example	43
Figure 4.1	Synthetic seismic trace	45
Figure 4.2	CX91 final migrated seismic stack	46
Figure 4.3	Interpretation of CX91	47
Figure 4.4	12X final migrated seismic stack	50
Figure 4.5	Interpretation of 12X	51
Figure 4.6	18XC final migrated stack	54
Figure 4.7	Interpretation of 18XC	55
Figure 4.8	FS86-3 and FS84-1 interpreted data	57
Figure 4.9	FS86-1 final migrated stack	59
Figure 4.10	Interpretation of FS86-1	60
Figure 4.11	FS85-1 final migrated stack	62
Figure 4.12	Interpretation of FS85-1	63
Figure 4.13	FS86-2 final migrated stack	64
Figure 4.14	Interpretation of FS86-2	65
Figure 5.1	Gravity Line 89G Bouguer anomaly.	73
Figure 5.2	Gravity Line 88G Bouguer anomaly.	74
Figure 5.3	Logarithmic-power spectrum	75
Figure 5.4	Interpretation of Logarithm-Power spectrum.	76
Figure 5.5	Observed and theoretical gravity responses of Line 88G.	79

Figure 5.6	Observed and theoretical responses of Line 89G.	80
Figure 5.7	Theoretical gravity response of Turner Valley structure.	81
Figure 6.1	Cross-section locations	84
Figure 6.2	Jumpingpound cross-section	85
Figure 6.3	Stoney cross-section	86
Figure 6.4	Bow River cross-section	87
Figure 6.5	Wildcat Hills cross-section	88
Figure 6.6	Structural elements map	92
Figure 6.7	Development of synclines	95

Chapter 1 Introduction

1.1 Introduction

The aim of this thesis is to provide a well-constrained interpretation of geophysical and geologic data from the triangle zone in the Rocky Mountain Foothills west of Calgary. The triangle zone is found at the leading edge of the disturbed belt, where thrust and fold structures of the Canadian Cordillera terminate as a foreland-tapering wedge within foreland basin strata. It is a type of buried thrust front, and has been recognised at the leading edge of several thrust belts around the world (Banks and Warburton, 1986; Gordy et al., 1977; Morley, 1986; Vann et al., 1986).

A key feature of a triangle zone is the presence of two major faults with opposing vergence that bound a foreland-directed intercutaneous wedge that has been forced into a foreland molasse. Strata overlying this wedge are deformed into a foreland-dipping frontal monocline that is juxtaposed against hinterland-dipping strata within and behind the wedge. Flat autochthonous strata underlie the foreland- and hinterland-dipping strata to form a roughly triangular structural geometry. Because triangle zones may be important regular features of thrust fronts, and because they are prospective for hydrocarbons, there is much interest and debate over their development. Currently there are two main models for the genesis of a triangle zone, although there are few published studies in which these models have been critically tested.

In this study, good-quality seismic data, well-log data, surface geological data, and

gravity data have been analyzed and interpreted to provide a detailed structural picture of the triangle zone in the Jumpingpound-Wildcat area, about 30 km west of Calgary (Figure 1.1). The region is the site of two major gas fields, the Jumpingpound and Wildcat Hills gas fields, that are trapped within the hanging wall of a thrust fault that has detached a thin slice of carbonate rocks of Paleozoic age. Hence, a good database of well data complements the surface control and seismic data, and has allowed for a well constrained interpretation. The interpretation of these data reveals a structure that contains elements that both challenge and support the current ideas about the development of triangle zones. These observations, and their interpretations, are the main new contributions of this thesis towards an improved understanding of the development of triangle zones.

This thesis is organised as follows: in this introductory chapter the research objectives and methodologies are specified, and the database is described. A review of the triangle zone and of the regional geology follow in Chapter two. In Chapter three, details of the seismic data acquisition and processing are given, and in Chapter four, the interpretation of the seismic data is presented. In Chapter five, the acquisition, processing, and interpretation of gravity data are described. Finally, Chapter six focuses on the integration of the data and discussion of the results.

1.2 Objectives

The primary objective of this work was to integrate reflection seismic, borehole,

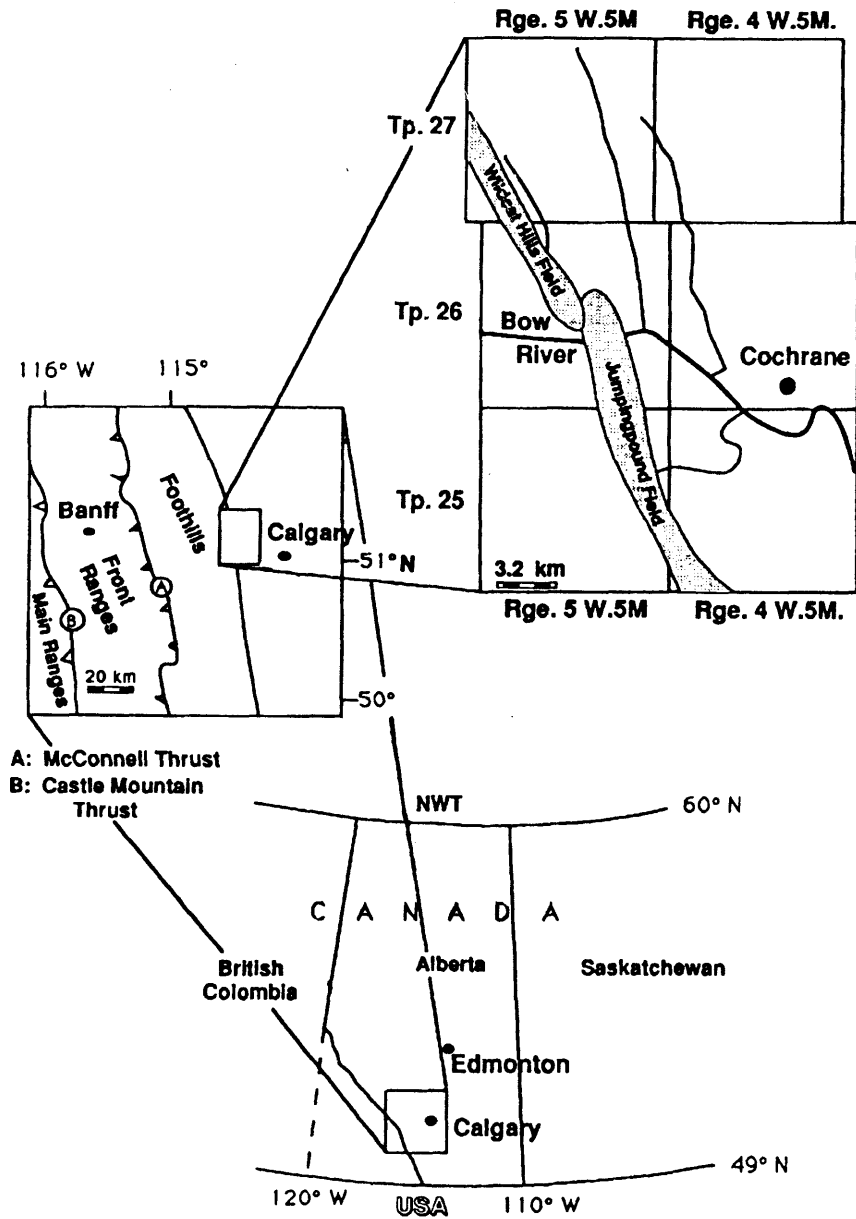


Figure 1.1 Map showing location of study area.

surface-geologic, and gravity data to construct a well-constrained interpretation of the geologic structures in the thesis area, with particular interest in resolving the structures at shallow depths. Subsidiary objectives were to find methods of improving reflection-seismic imaging of the triangle zone, and to evaluate the efficacy of the gravity method for the delineation of Foothills structures.

1.3 Methodology

Reflection seismology provides the key data of this study. Careful reprocessing of these data was thus an important step of the research work. Ancillary work included the acquisition, processing, and interpretation of gravity data, the retrieval of well-log data, and some limited geological mapping.

1.4 Database

Approximately 60 km of reflection seismic data, some acquired by The University of Calgary since 1985 and the remainder donated by industry for the project, form the core of the database. Due to the proprietary nature of the donated seismic data, no specific shotpoint locations can be provided. Approximately 26 km of gravity data were acquired along two profiles, and numerous wells provided further subsurface control. The locations of the seismic lines, gravity profiles and well positions are shown in Figure 1.2. Surface geologic control was provided by Geological Survey of Canada maps 1419

(Jumpingpound Creek East) and 652A (Wildcat Hills, East Half), and mapping was done by students at The University of Calgary (D. Spratt, pers. comm.).

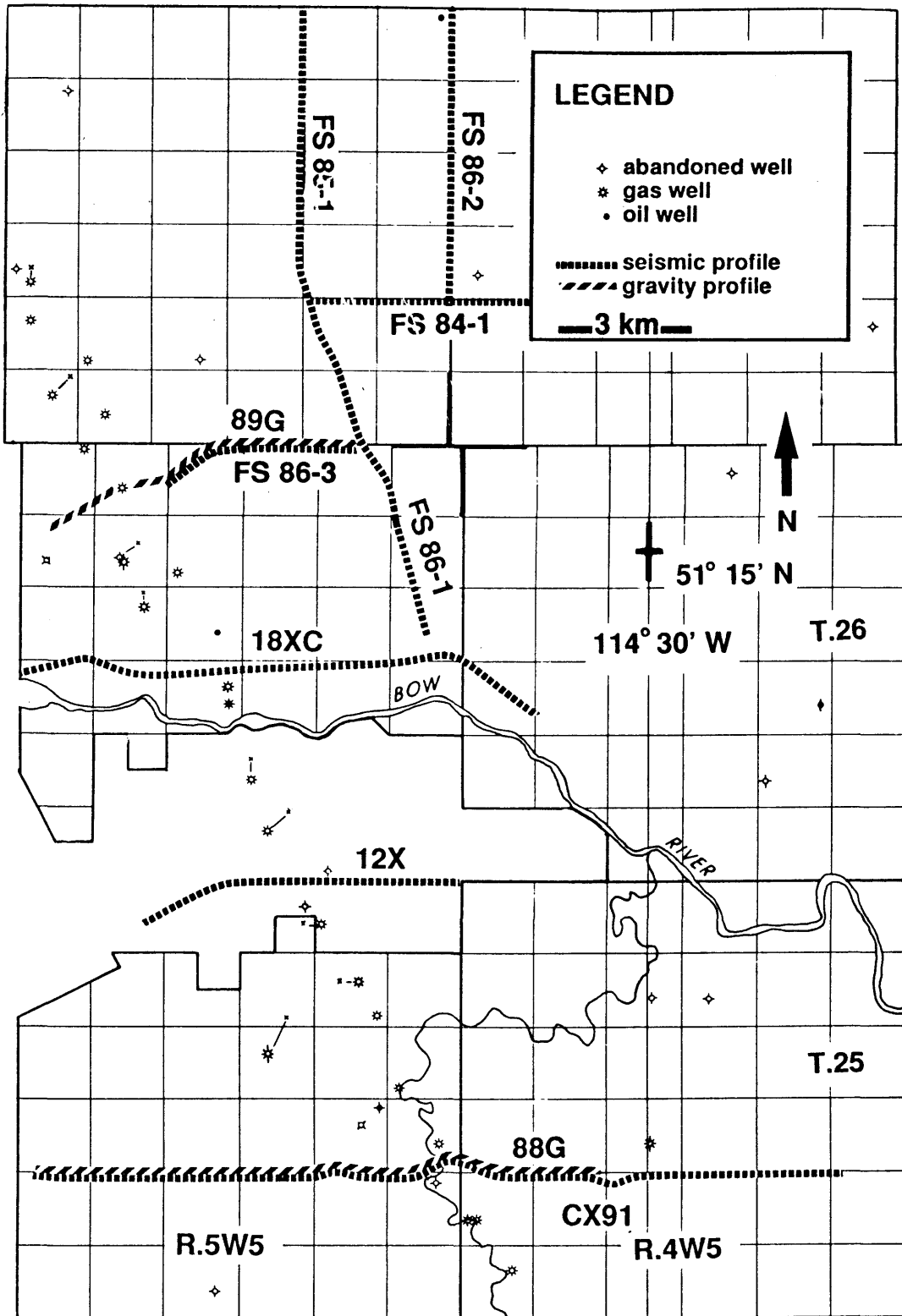


Figure 1.2 Seismic and gravity lines used in the study.

Chapter 2 Geological Review

2.1 Regional Geological Setting

The Western Canada Sedimentary Basin (WCSB) comprises two genetically and lithologically distinct sedimentary packages that overlie a gently west-dipping crystalline basement. The older of these packages is composed mainly of calcareous rocks of Paleozoic age that are a manifestation of a miogeoclinal basin (McCrossan, 1964). The younger package contains rocks of Mesozoic age. It comprises foreland molasse sediments: shales, sandstones, and coals, which were derived from the west and deposited after uplift occurred as a series of terranes collided with the western margin of the North American Craton (Monger et al., 1982). These two major sedimentary sequences thin from west to east.

Compressional stresses of the Columbian and Laramide orogenies deformed and shortened the sedimentary package, creating the Canadian Cordillera (Bally et al., 1966). Although the structuring is deeply rooted to the west, it is generally accepted that the crystalline basement was not involved in the deformation in the Rocky Mountain Foothills (Dahlstrom, 1970). Deformation was hence "thin-skinned", and the Foothills are dominated by east-verging listric thrust faults in the Mesozoic sedimentary section, which occasionally involve the carbonate rocks of the Paleozoic sedimentary section. Bally et al. (1966) and Dahlstrom (1970) give a comprehensive overview on the tectonic evolution and structural style of the region.

2.2 Study Area

The physiography of the area is typical of the Foothills belt, being characterised by broad ridges and valleys. The ridges are in general formed by more resistant sandstones, and valleys have been carved into the less resistant shales exposed at the surface. Maximum relief is approximately five hundred metres, with elevations ranging from 1200 metres above mean sea level in the east, to 1700 metres above mean sea level in the west. The sedimentary section is in total about four kilometres thick in the study area, with the pre-Cretaceous unconformity between the primarily clastic Mesozoic section and the primarily calcareous Paleozoic section at approximately two and a half to three kilometres depth. The major geological formations in the study area are detailed in Figure 2.1.

Rocks of the Mississippian Rundle Group and Banff Formation are the oldest and deepest rocks involved in the triangle zone in the study area. The Rundle Group is made up of carbonate rocks that conformably overlie the Banff Formation. The Banff Formation is an open marine, calcareous shale with limestone stringers (Workum, 1978). It overlies the Exshaw Formation, a black shale that is an important seismic marker. The Rundle Group and Banff formations range from 300 to 400 m and 150 to 200 m respectively, and have sonic log velocities that range from 5500 to 6000 m/s. The Mississippian top is an important seismic reflection marker. It is a composite event, a result of interference between two reflections: (1) the reflection generated by the negative acoustic impedance contrast between the Blairmore Formation and the Kootenay

Era	Period	Formation or Group	Lithology	Average Seismic Velocities (m/s)	
MESOZOIC	Tertiary	Paskapoo		3300-3700	
	Cretaceous	Upper	Edmonton		
			Bearpaw shale		
		Lower	Belly River	3800-4100	
	Alberta Group	Lower	Wapiabi		3900-4150
			Cardium		
			Blackstone		
	Lower	Lower	Blairmore		4200-4400
			Kootenay		4100-4300
	PALEOZOIC	Jurassic	Fernie		5500-6000
Mount Head					
Missippian		Runde Group	Turner Valley		
			Shunda		
			Pekisko		
			Bant		
			Essex		
Devonian		Devonian	Palliser		
			Fairholme		
Cambrian		Cambrian			

Figure 2.1 Table of formations in study are (modified from Gordy et al.,1975). Major glide Horizons are indicated by arrows.

Formation, and (2) the reflection resulting from the positive acoustic impedance contrast between the Fernie Formation and the Rundle Group. At the base of the Banff Formation, most likely in the Exshaw Formation, is the lowermost detachment observed in the area.

The Kootenay Group conformably and abruptly overlies the Jurassic Fernie Formation, a black marine shale. The Fernie Formation ranges from 15 to 150 m thick, and is an important detachment zone. It has a sonic log velocity of approximately 4200 m/s.

The Lower Cretaceous Blairmore Group is dominated by continental and marine interbedded sandstones, siltstones, and shales. These rocks have sonic log velocities of 3950 to 4250 m/s, and thicknesses ranging from 300 to 400 m. The Blairmore Group disconformably overlies the Jura-Cretaceous Kootenay Group, which is also made up of interbedded sandstones, siltstones, and shales. It ranges from 0 to 350 m in thickness and has sonic log velocities that range from 4250 to 4850 m/s.

The Alberta Group, which is made of the Wapiabi, Cardium, and Blackstone formations, overlies the Blairmore Group with a contact that is abrupt and disconformable (Stott, 1963). The Blackstone and Wapiabi formations are marine shales, and are both important detachment horizons. Their sonic log velocities range from 3800 to 4000 m/s, and their thicknesses range from 300 to 450 m. The Wapiabi and Blackstone shales sandwich the Cardium Formation, which is primarily made up of sandstones and conglomerates, and is approximately 100 m thick. It has a sonic log velocity of up to 4200 m/s, and is an important seismic marker in the area. The marine shales of the

Wapiabi Formation grade conformably into the overlying massive sandstones of the Belly River Formation. These sandstones range from 350 to 450 m in thickness and have sonic log velocities that range from 3800 to 4360 m/s.

Where present, the Bearpaw shale separates the Edmonton Group from the underlying Belly River Formation. Where the Bearpaw does not exist, the Belly River Formation and Edmonton Group are lumped into the Brazeau Group, with fluvial- deltaic strata as Lower Brazeau and continental strata as Upper Brazeau. The deltaic facies of the Edmonton Group is approximately 600 m thick and the continental sequence is about 450 m thick. Bulk sonic log velocities for the Edmonton Group range from 3500 to 3800 m/s. With its heterogeneous sequence of lithologies, in particular the presence of coals, the Edmonton Group contains two important detachment zones (Figure 2.1).

Unconformably lying over the Edmonton Group is the Paskapoo Formation which is of Tertiary age. It is dominated by sandstones, but also has shales, some coals, and conglomerates (Workum, 1978). It ranges from 750 to 1200 m in thickness and has sonic log velocities from 3300 to 3800 m/s.

The velocities annotated in the Table of Formations (Figure 2.1) are seismic velocities averaged over major lithological intervals. They were calculated by dividing the known formation thicknesses into the observed seismic travel times at well-seismic tie locations. The values shown are averaged values from several well-seismic tie locations in the study area. These values are slightly lower than the sonic log derived velocities. This is due to the characteristic of seismic energy, which has frequencies in the Hz range, to propagate through the earth at a slower velocity than sonic energy, which

has frequencies in the kHz range.

A geological map of the study area (Figure 2.2) shows the surface anticline of the triangle zone at Wildcat Hills that trends along the NW-SE regional strike. To the east of this anticline are gently east-dipping rocks of the Alberta syncline. Typical Foothills west-dipping strata flank the west side of the triangle zone.

2.3 Review of the Triangle Zone

The triangle zone is found at the leading edge of this disturbed belt, where thrust and fold structures of the Canadian Cordillera terminate as a foreland tapering wedge within foreland basin strata. A generalised cross-section of a triangle zone is shown in Figure 2.3. In this thesis, the uppermost fault is referred to as the *upper detachment*. It separates overlying west-verging rock from underlying east-verging rock. The lower fault, which is defined as the *lower detachment*, is a basal, or sole fault, that cuts upsection from west to east, and flattens out at a higher stratigraphic level. It is easterly verging, and it is thought to merge with the upper detachment at a point called a *branch point*. It is a blind fault, as it does not cut up to the surface. The region between these two faults is called the *intercutaneous wedge* (Charlesworth et al., 1987). It typically is composed of an antiformal stack of duplex structures, reaching maximum thickness at the *main culmination*.

The genesis of the upper detachment is the key difference between two models for the evolution of triangle zones. Charlesworth and Gagnon (1985) suggest that the upper

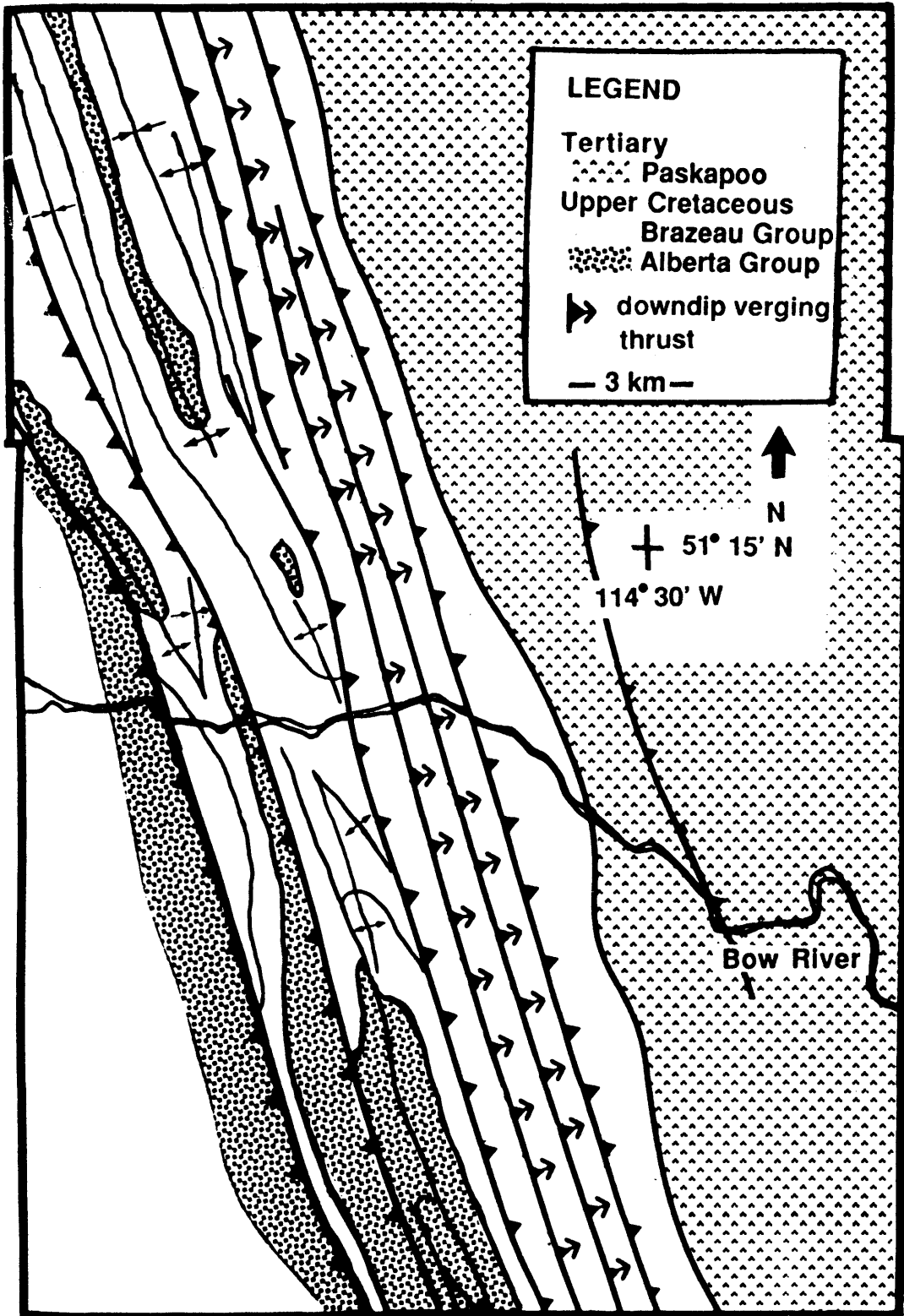


Figure 2.2 Geological map of the study area (modified from Lawton and Spratt, 1991).

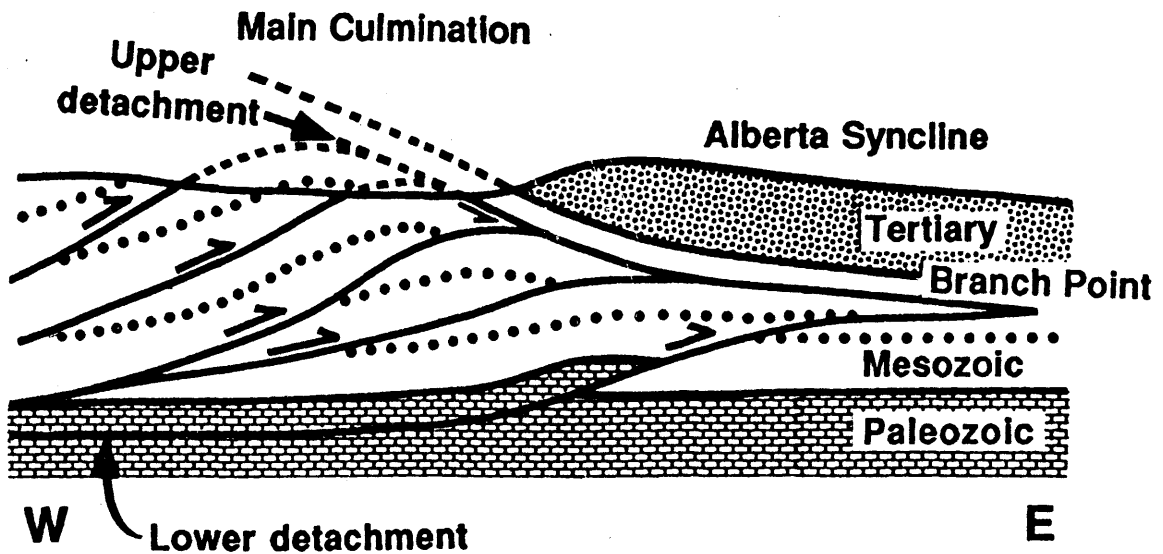


Figure 2.3 Schematic cross section of a triangle zone.

detachment initiates as a conjugate backthrust (Figure 2.4). Furthermore, they suggest that triangle zones propagate in a series of cycles, with triangle zones abandoned as new detachment surfaces develop.

Jones (1982), however, suggests that the upper backthrust is initially parallel to the sole thrust, and is displaced vertically with the emplacement of the intercutaneous wedge, deforming the hanging wall such that it dips toward the foreland, forming the flank of a syncline (Figure 2.5).

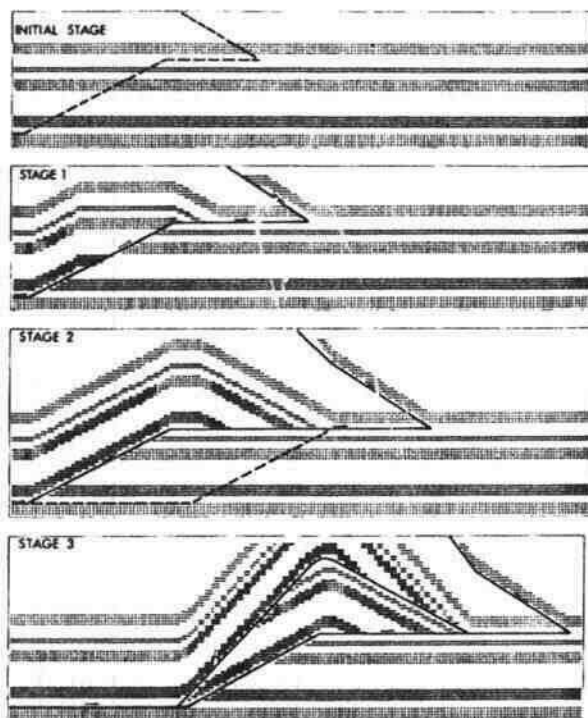


Figure 2.4 Charlesworth model for the development of a triangle zone (after Charlesworth and Gagnon, 1985).

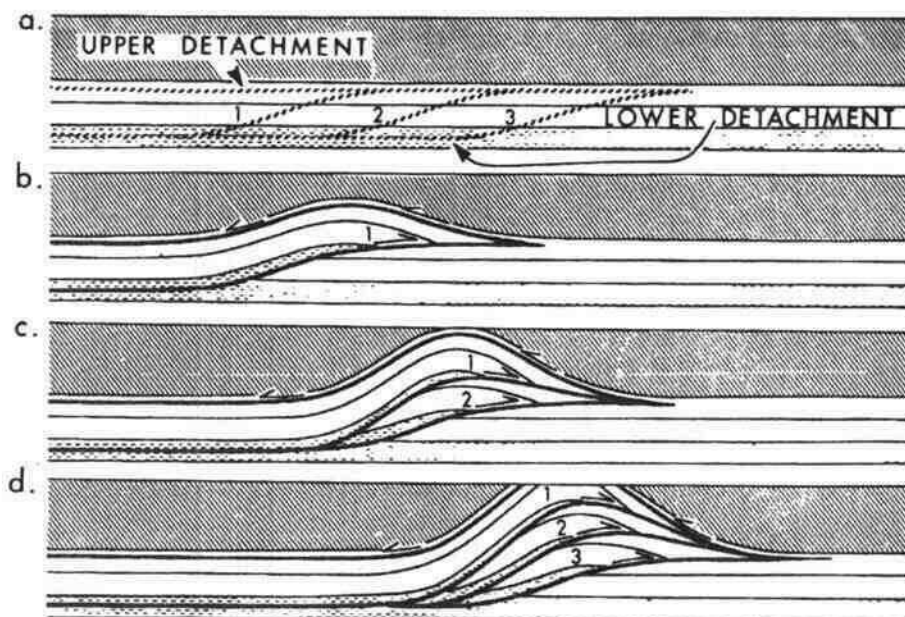


Figure 2.5 Jones model for the development of a triangle zone (after Jones, 1982)

2.4 Previous Structural Interpretations

Initial interpretations by Hume (1927), of the structure in the Jumpingpound-Wildcat area were based upon surface geology, and were rather simplistic. Seismic investigation and drilling followed the publication of Hume's (1927) work and a new interpretation was published by Link (1949). It was a more complex interpretation; however, it was not until later, when a cross-section was published by Fox (1959), that the blind nature of the lower detachment was realised (Figure 2.6).

Ollerenshaw (1976) published a more detailed cross-section also with a blind basal detachment (Figure 2.7). However only the cross-sections of Gordy et al. (1977), and Jones (1989) (Figure 2.8) show the triangle zone as being composed of a series of vertically stacked duplexes wedged between an upper and lower detachment. This is consistent with the current models of a triangle zone. However, the cross-section of Gordy et al. (op. cit.) is largely schematic in the region of the thrust front. The Jones cross-section (Figure 2.8), a reinterpretation of the Ollerenshaw cross-section (Figure 2.7), gives a reasonable generalised view of the triangle zone in the area. However, its structural details were found to be inconsistent with the results contained in this thesis.

Recent work on triangle zones in other parts of southern Alberta by students at The University of Calgary is providing additional insight on the triangle zone. MacKay (1991) interpreted a triangle zone at Turner Valley, southwest of Calgary, as an antiformal stack that has been wedged into the foreland between upper and lower detachment surfaces. He argues the recent seismic data preclude the applicability of the fault

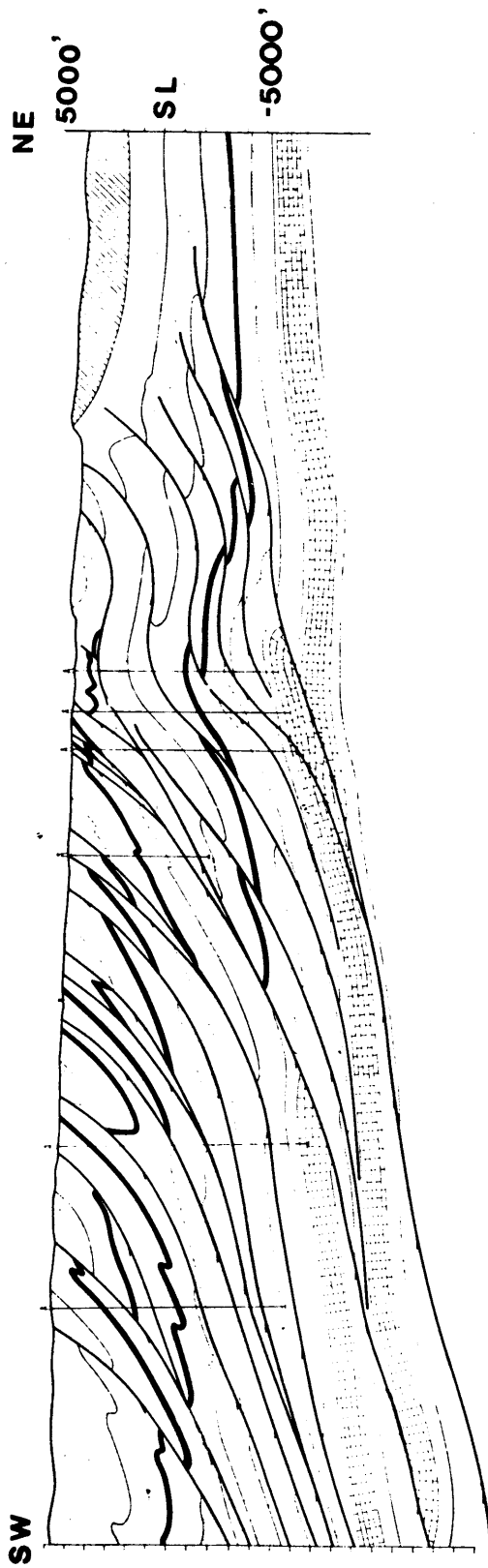


Figure 2.6 Interpretation in Jumpingpound area (after Fox, 1959).

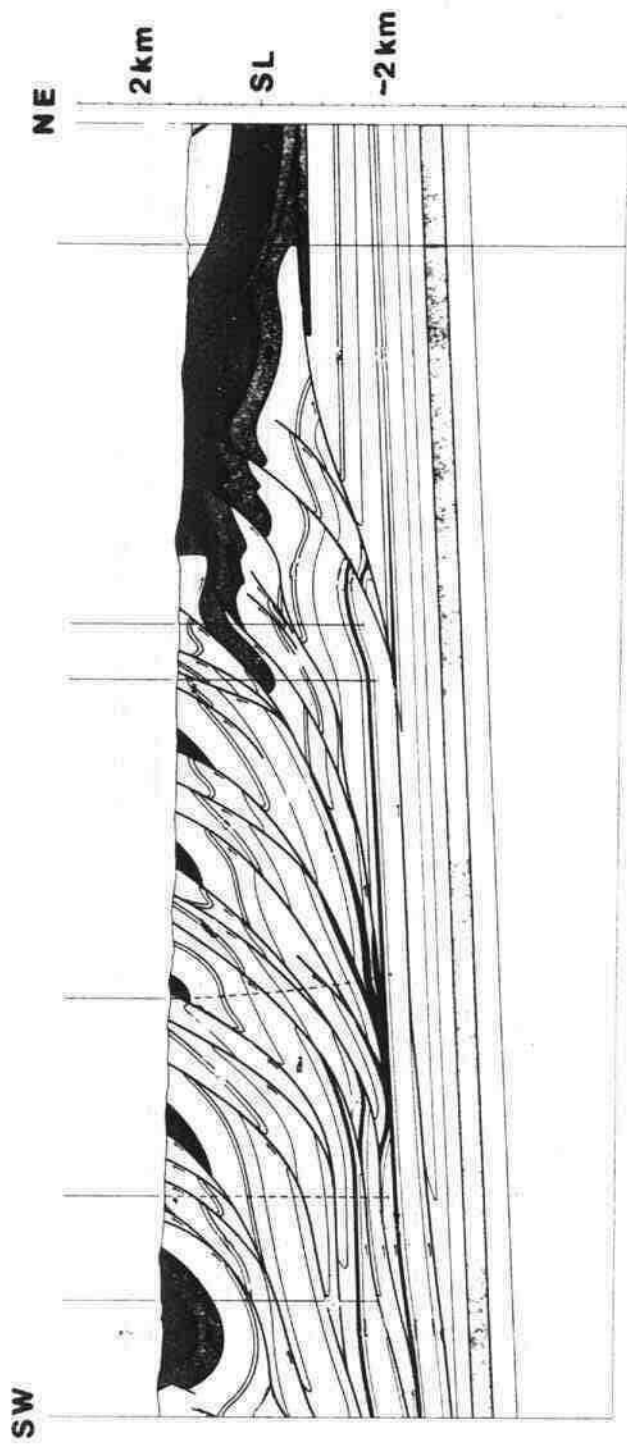


Figure 2.7 Interpretation of Jumpingpound structure (after Ollerenshaw, 1979).

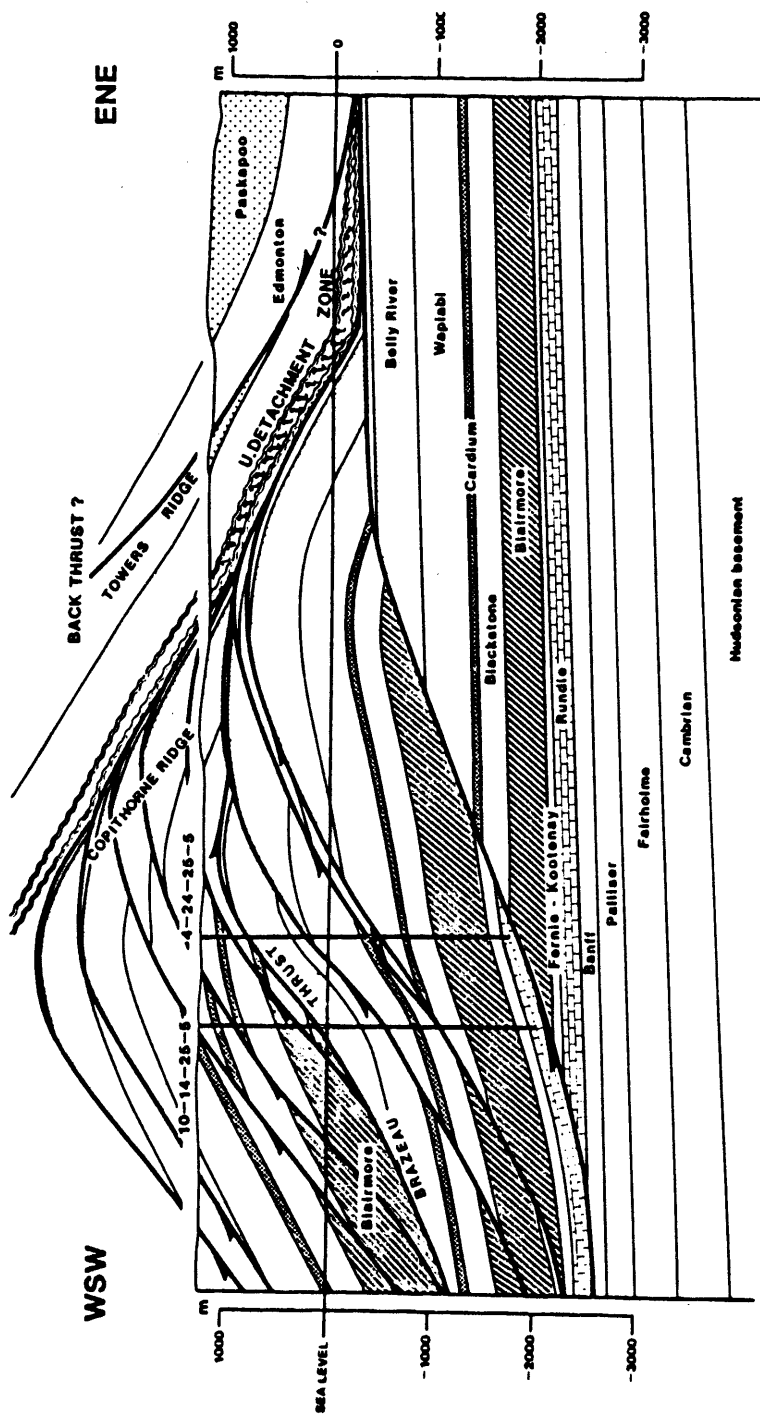


Figure 2.8 Interpretation of Jumpingound structure (after Jones, 1989).

propagation fold models for the Turner Valley structure that have gained acceptance in the literature. Furthermore, he has interpreted the structure at Turner Valley to have an abandoned upper detachment, or relic, which would fit the Charlesworth et al. (1987) model. Sanderson and Spratt (1992) interpret the existence of a triangle zone relic in the Rocky Mountains, west of the Turner Valley structure, which also supports the model of Charlesworth et al. (1987) in terms of the advancement of the triangle zone into the foreland basin. Hiebert and Spratt (1991) interpreted a series of transverse features in the Pincher Creek area as several duplexes occurring within a single major thrust sheet, with both the floor and roof thrusts exposed at the surface. Skuce et al. (1992) interpret a triangle zone in central Alberta to be a passive-roof duplex, and report deformation to have propagated under the foreland 30 km beyond the main triangle zone structure. A similar feature is noted by Hiebert (1992) 65 km east of the triangle zone, near the town of Monarch, in southern Alberta.

Chapter 3 Seismic Data Processing

3.1 Introduction

The processing of the seismic data, undertaken for this thesis, produced very good-quality images of the subsurface structure in the study area. This processing is described in this chapter, with focus given to the key processes that led to good results. Furthermore, an examination of the limitations on data quality posed by specific acquisition parameters, primarily that of acquisition geometry, is presented. It is shown that instrumental to the achievement of good-quality images were the application of beam steering (applied to shot records) and f - x filtering (applied to stacked sections), two signal enhancement techniques that enhance spatially correlatable signals. It is also shown that those data acquired with high spatial sampling density gave the best results.

In this chapter the acquisition parameters are provided along with an analysis of their effectiveness in recording reflections from dipping geological strata. Recommendations for the optimal acquisition parameters are made; the hardware and software used are listed; and the general processing flow used is provided, with a detailed description of the key processing steps of static corrections, noise reduction, and imaging.

3.2 Acquisition

The data were acquired with parameters that were typical for seismic data acquired

in Alberta in the late 1970's and early 1980's. The acquisition took place between 1976 and 1986, using vibroseis, dynamite, and land airguns as sources. The parameters used for the acquisition of each line are detailed in Tables 3.1 to 3.6.

Figure 3.1 shows examples of shot records from the thesis dataset. These data, acquired with a dynamite source, have a reasonably good signal-to-noise ratio. However, the data acquired with vibroseis and airguns as sources tended to have stronger ground-roll noise.

Acquisition parameters pose constraints upon the range of dips that can be recorded on a migrated zero-offset section. Three acquisition parameters that place important limits upon the recordable range of geologic dips are the receiver group interval, the recording aperture, and the listening time.

The receiver group interval is the parameter that is the most important in recording reflections from within the triangle zone, which can have steep dips (up to 75°) at shallow depths (less than 1000 m). The group interval determines the spatial aliasing limit which in turn places boundaries on the range of geologic dip that can be recorded in the seismic survey. The maximum unaliased dip (θ_s) for a given dominant frequency (f) and a constant velocity medium is given by:

$$\theta_s = \sin^{-1}\left(\frac{V}{4f\Delta X}\right), \quad (3.1)$$

where V is the medium velocity and ΔX is the spatial sample interval (Yilmaz, 1987). A small spatial sample interval is thus desirable to maximise the range of recordable dip. As an example, for line CX91 with $V = 4000$ m/s, $f = 30$ Hz, and $\Delta X = 50$ m, the dip

Table 3.1

Acquisition parameters of Line FS86-2.

Acquisition date
August, 1986

Source
Airgun
number: 3
volume: 983 cm³
vertical stack: 8
source interval: 60 m

receivers
type: 14 Hz (MD 40)
number: 9
array: in line (3.3 m)
group interval: 30 m

instrument
DFS V MSP
number of channels: 120
sample rate: 2 ms
recording time: 4 s

recording filters
12-128 Hz bandpass
60 Hz notch

spread
1800-30 * 30 - 1800 m

coverage
3000%

Table 3.2

Acquisition parameters of Line FS85-1.

Acquisition date
August, 1985

Source
Dynamite
charge: 1 kg
source interval: 60 m

receivers
type: 14 Hz (MD 40)
number: 9
array: in line 3.3 m
group interval: 30 m

instrument
DFS III
number of channels: 48
sample rate: 2 ms
recording time: 5 s

recording filters
12-128 Hz bandpass
60 Hz notch

spread
1500-60 m *

coverage
1200%

Table 3.3

Acquisition parameters of Line CX91.

Acquisition date

September, 1986

Source

Vibroiseis (4)

sweep spectrum: 56-14 Hz

sweep length: 10 s

vertical stack: 16 sweeps

source interval: 100.2 m

receivers

type: 10 Hz

number: 10

array: in line (10 m)

group interval: 50.1 m

instrument

type: unknown

number of channels: 48

sample rate: four ms

recording time: 15 s

recording filters

0-62 Hz bandpass

60 Hz notch

spread

1659-503 * 503-1659 m

coverage

1200%

Table 3.4

Acquisition parameters of Line 18XC.

Acquisition date

July, 1981

Source

Vibroiseis (4 Mertz 10s)

sweep spectrum: 52-12 Hz

sweep length: 13 s

vertical stack: 16 sweeps

source interval: 152 m

receivers

type: 10 hz (L28)

number: 9

array: in line (4.75 m)

group interval: 38 m

instrument

type: Geosource MDS 10

number of channels: 96

sample rate: 4 ms

recording time: 16 s

recording filters

15-62.5 Hz bandpass

60 Hz notch

spread

1900-114 * 114-1900 m

coverage

1200%

Table 3.5

Acquisition parameters of Line 12X.

Acquisition date
August, 1981

Source
Vibroseis (4 Mertz 10s)
sweep spectrum: 52-12 Hz
sweep length: 13 s
vertical stack: 16
sweeps
source interval: 152 m

receivers
type: 10 hz (L28)
number: 9
array: in line (4.75 m)
group interval: 38 m

instrument
type: Geosource MDS 10 Sum
number of channels: 96
sample rate: 4 ms
recording time: 16 s

recording filters
15-62.5 Hz bandpass
60 Hz notch

spread
1900-114 * 114-1900 m

coverage
1200%

Table 3.6

Acquisition parameters FS86-2.

Acquisition date
August, 1986

Source
Airgun
number: 3
volume: 983 cm³
vertical stack: 8
pops
source interval: 60 m

receivers
type: 14 Hz (MD 40)
number: 9
array: in line (3.3 m)
group interval: 30 m

instrument
DFS V MSP
number of channels: 120
sample rate: 2 ms
recording time: 4 s

recording filters
12-128 Hz bandpass
60 Hz notch

spread
1800-30 * 30 - 1800 m

coverage
3000%

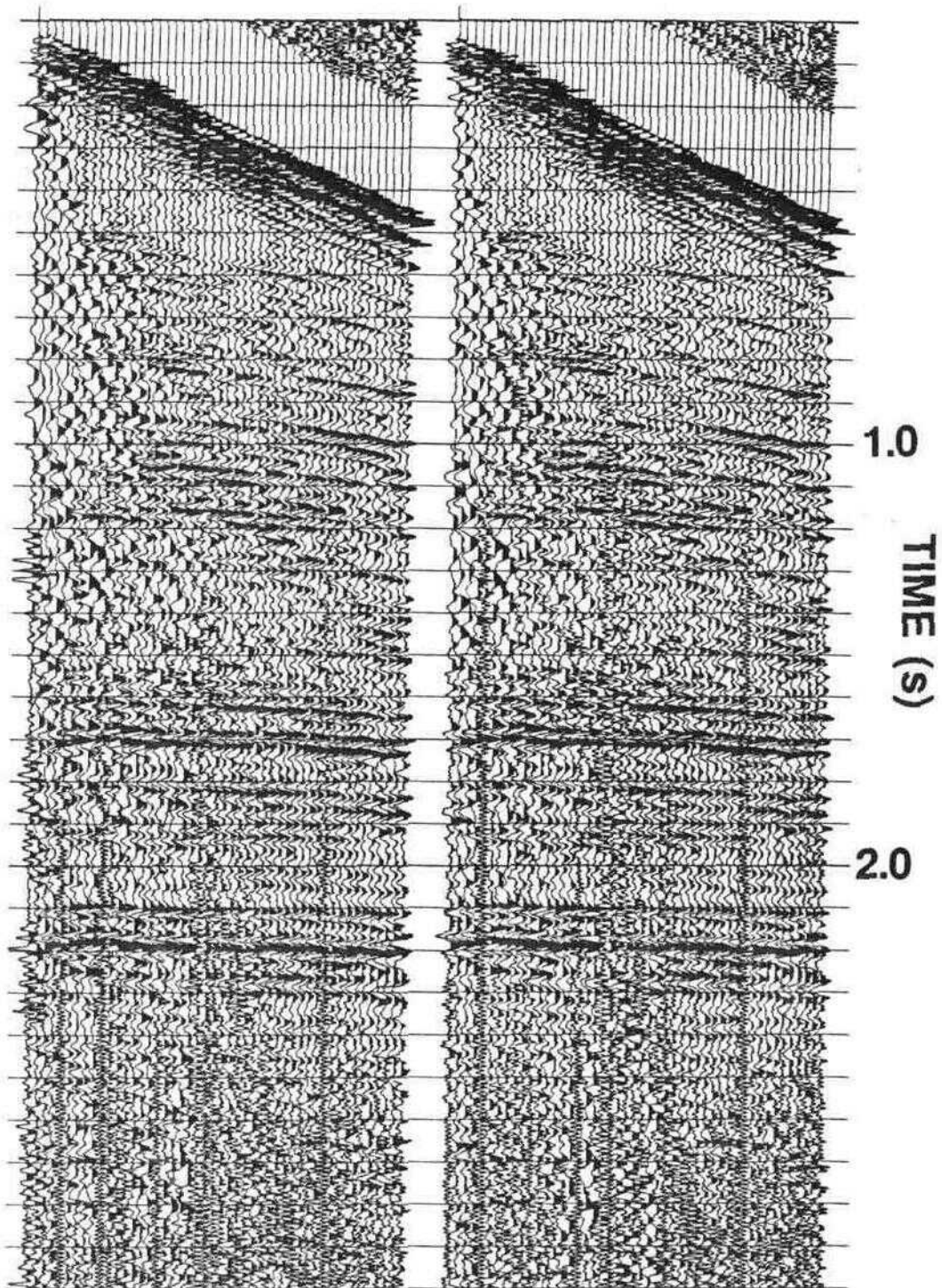


Figure 3.1 Unfiltered shot records from Line FS85-1.

limit beyond which spatial aliasing will occur is calculated to be 42 .

The record length poses limits upon the maximum dip recorded on a zero-offset migrated section. However its effect is not significant for shallow reflectors but progressively increases with increasing depth. The recording-time limit upon dip (θ_{rec}) for a constant velocity medium is quantified by Lynn and Deregowski (1981) as:

$$\theta_{rec} = \cos^{-1}\left(\frac{t_z}{t_{rec}}\right), \quad (3.2)$$

where t_z is the two-way time to a given depth z and t_{rec} is the record length.

The line length (or aperture) similarly has a limiting effect upon the migrated image that is a minimum for the shallow depth, and which progressively increases with increasing depth. Lynn and Deregowski (op. cit.) show this maximum (θ_a) for a constant velocity medium to be:

$$\theta_a = \tan^{-1}\left(2 \cdot \frac{A}{Vt_z}\right), \quad (3.3)$$

where A is the effective aperture or line length, V is the medium velocity, and t_z is the two-way reflection time to the event of interest. Sense of dip (e.g., east dip vs. west dip on a seismic section) and position on line are important in determining the effective aperture. For example, for a given zero-offset trace near the east end of a line, the effective aperture for recording east dips is the length of line to the east of the trace location. For such a trace, the maximum imageable east dip is thus much smaller than the maximum imageable west dip. Furthermore, the maximum imageable east dip will

decrease to zero at the east end of the line, while the imageable west dip will increase to a maximum.

Figure 3.2 shows an example in which the three constraints are compared. In this example, parameters typical for the thesis dataset were used: i.e. a velocity of 4000 m/s, a dominant frequency of 30 Hz, a record length of 4 s, and an aperture of 1000 m. This example shows that at the shallow to medium depths where the steeper dips of the triangle zone are located, the spatial aliasing limit imposed by the station interval is the effective limiting parameter. Furthermore, this example shows the progressive decrease of imageable dip imposed by the aperture at greater depths.

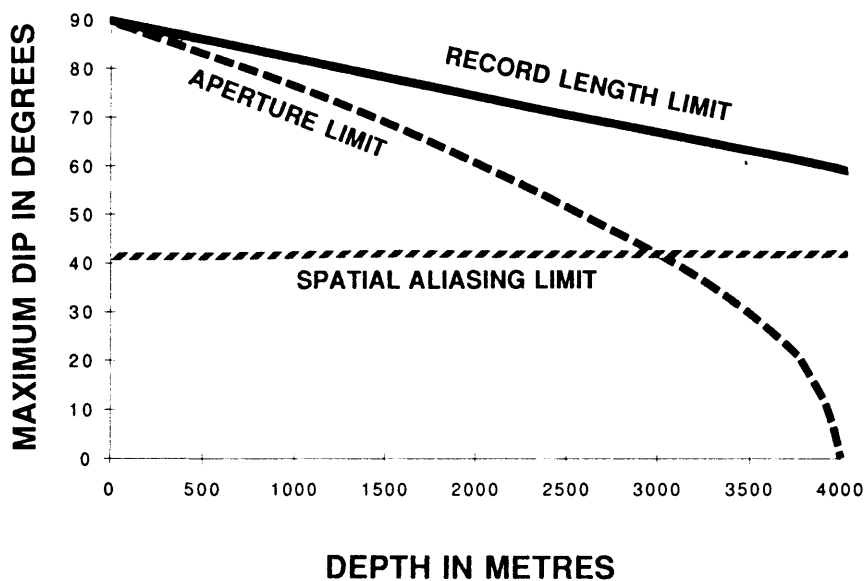


Figure 3.2 Acquisition constraints upon recordable dip. Velocity used is 4000 m/s, frequency is 30 Hz, record length is 4 s, and aperture is 1000 m.

An example of image degradation due to a limited aperture is shown in Figure 3.3. This figure shows that the image quality of easterly dipping events degrades near the east end of Line 12X, while flat reflections remain coherent to the end of the line.

An example of image degradation due to spatial aliasing is shown in Figure 3.4. This is a portion of line CX91, and shows that reflections with low or zero dip are well imaged. However, where the geology is known to contain steeply-dipping reflectors, particularly near the centre of the line, where the triangle zone is located, or near the west end of the line, where west dips dominate, the image is poor. This line has the largest spatial sample interval in the dataset (50 m), which imposes a dip limit of 45° using a velocity of 3500 m/s and a frequency of 25 Hz.

3.3 Processing - General

The data were processed by the author at The University of Calgary. Western Atlas software on an IBM 4381 computer was used for most of the seismic data processing. However, a Perkin Elmer 3240 computer was used for refraction static corrections, which were calculated using a procedure described by Lawton (1989). This computer was also used for beam steering, using a procedure described by Cheadle (1988).

The general flow of the data processing is outlined in Table 3.7. The specific processes that are considered to be most significant in the sequence, which include the static corrections, the beam steering, the velocity analysis, and the post-stack imaging, are

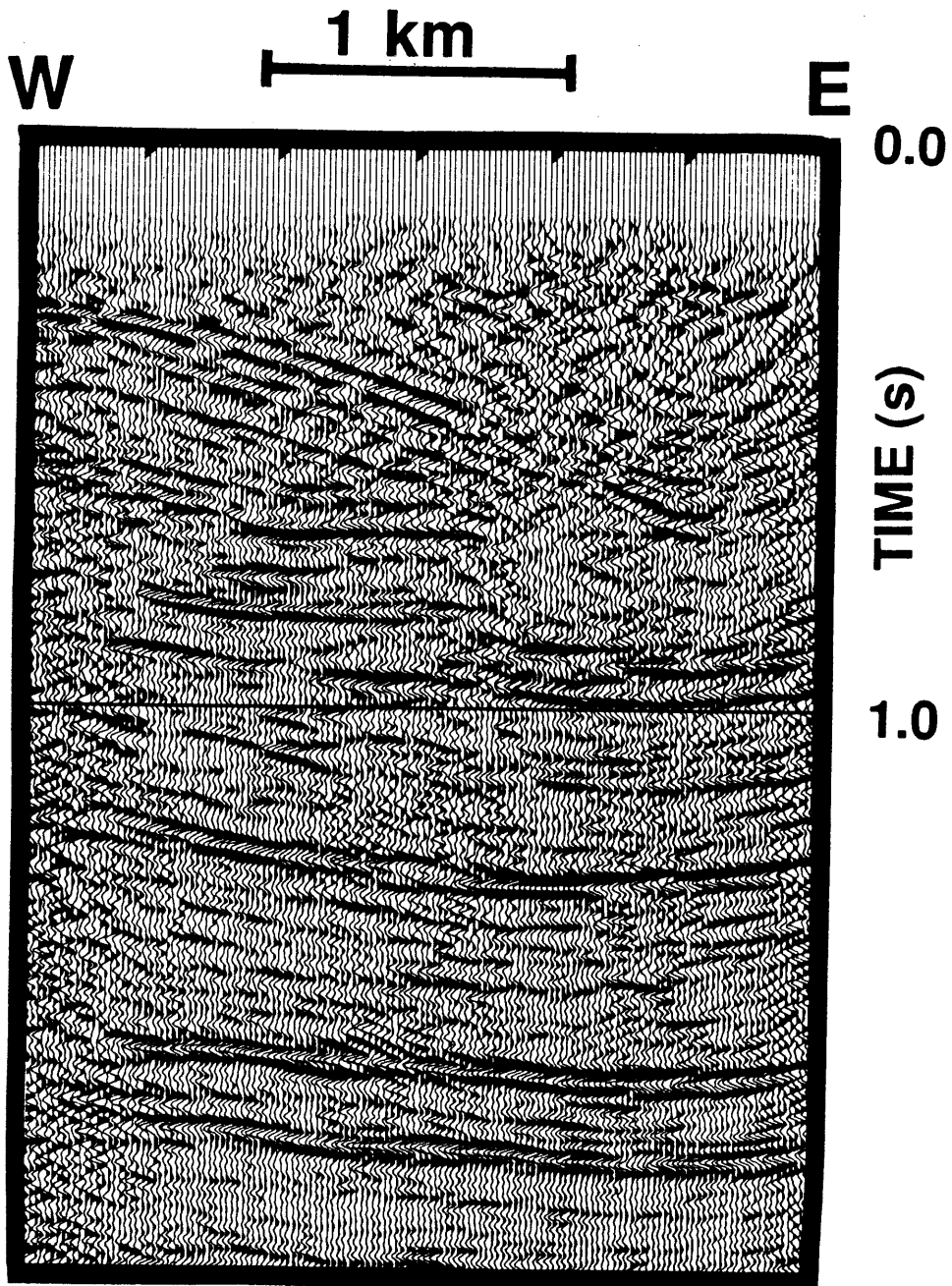


Figure 3.3 East portion of Line 12X that shows image degradation of east dips due to an inadequate aperture.

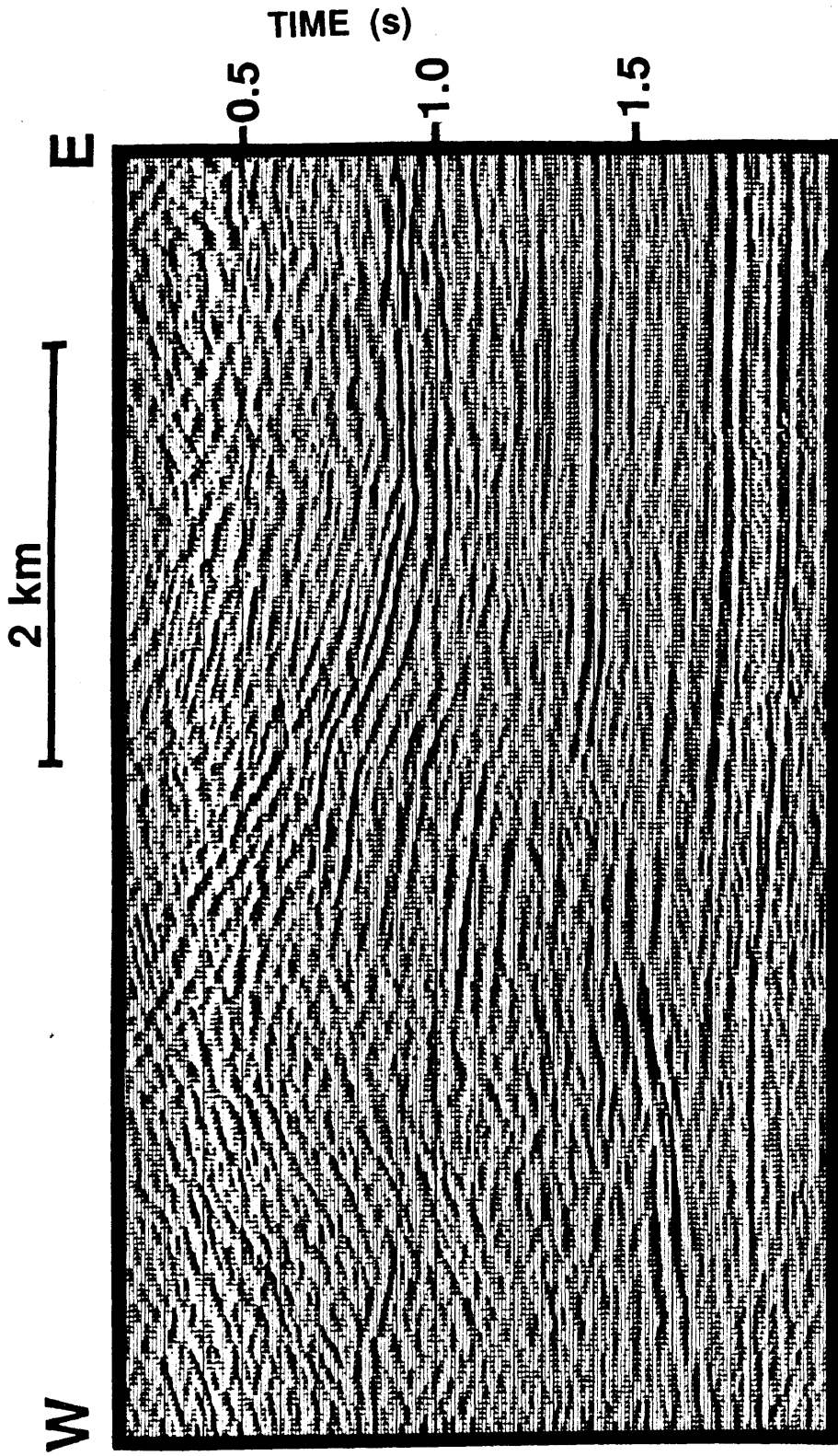
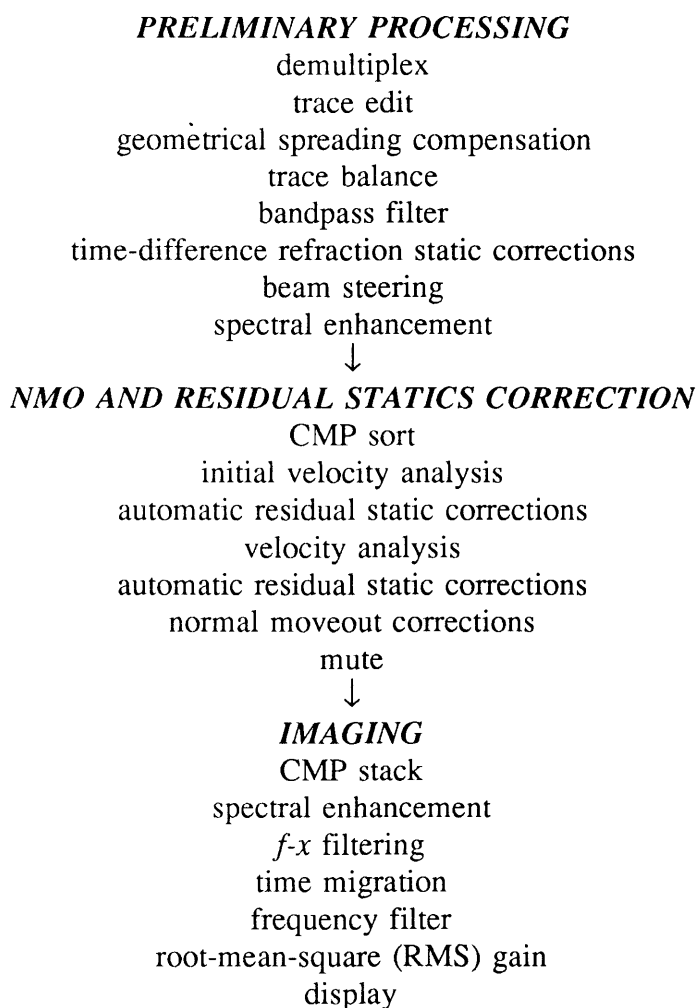


Figure 3.4 Example from Line CX91 of image degradation due to spatial aliasing. Shallow dips in the east are well imaged, while steeper dips in the west poorly resolved. There is no vertical exaggeration.

discussed in detail in the sections that follow in this chapter. The remaining steps are standard in the processing of reflection seismic data, and Yilmaz (1987) provides an excellent reference for their explanation.

Table 3.7 General processing flow



3.4 Preliminary Processing

The objective of the preliminary processing was to make appropriate amplitude corrections and improve the signal-to-noise ratio for the subsequent processing. After demultiplexing the data, which is a simple transposition of the data from the multiplexed recording format to a trace sequential format, the data were edited by visual inspection and included the manual elimination of traces with high-amplitude noise. Bandpass filtering was used to reject noise that was outside the band width of the seismic reflection signal. As an example, Figure 3.5 shows a bandpass filtered version of the shot records shown in Figure 3.1.

An exponential amplitude correction was applied to the data to correct the data for wavefield propagation amplitude losses, followed by a trace balance which was applied to reduce trace-to-trace inconsistencies in event amplitudes. This was particularly important for the beam steering, which examines amplitude similarity across several adjacent traces in order to discriminate against noise.

A spectral enhancement filter was used as a simple deconvolution method to increase the resolution of the reflection data. The filter improved the resolution of the data by balancing the amplitude spectrum of the data in the frequency domain over the bandwidth of the signal. It was important to apply this filter prior to the velocity analysis, as the increased resolution would improve the precision of the subsequent velocity analysis, as well as improve the solution of the residual statics estimations. However, it can also boost the amplitude of high-frequency noise in the data, and thus this process was applied after the beam steering of the data.

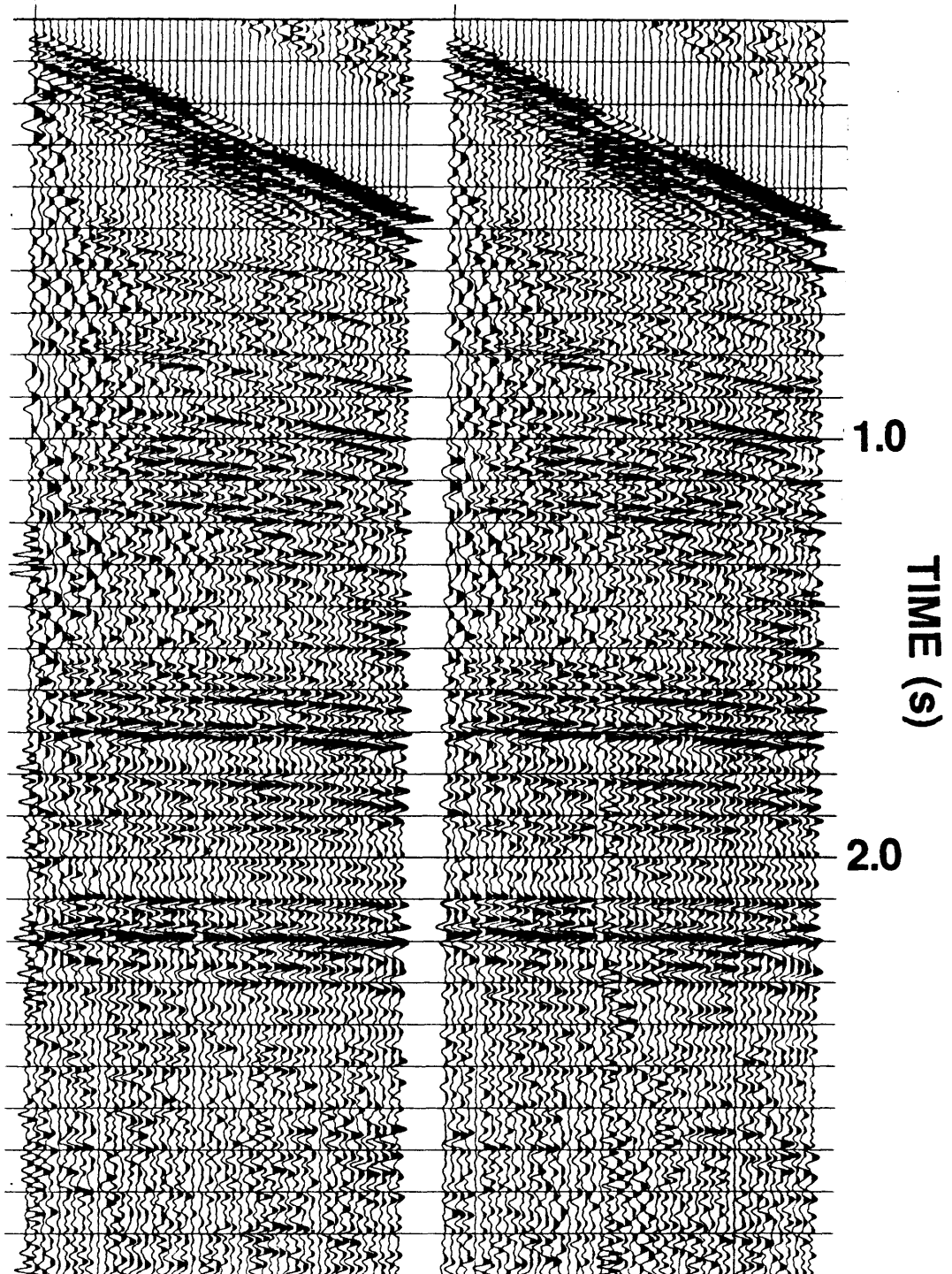


Figure 3.5 Shot records from Line FS85 (shown in Figure 3.1) after application of an 8-12-50-62 Hz bandpass filter.

3.5 Static Corrections

Seismic data must be adjusted to compensate for distortions in reflection traveltimes due to elevation changes along the seismic line and for time delays caused by the low-velocity weathering layer; otherwise degradation of the seismic image can result. Such adjustments are termed static corrections, as each seismic trace is bulk-shifted in time to simulate a common plane of acquisition. The process thus removes unwanted time-delay due to variations in thicknesses and velocities of near-surface layers.

In the study area, there is a veneer of glacial sediments, with thicknesses ranging from 0 m to 100 m, which overlies bedrock. Static variations present are caused by this low-velocity, surface layer whose bounding surfaces are nonplanar, is of varying thickness, and which lies upon a refractor surface that itself has a varying velocity.

The key to successful static corrections is the accurate calculation of the near-surface velocity structure. A time-difference method of statics calculation (Lawton, 1989) was used to calculate static corrections for most seismic lines in the dataset. In this method, delay times at each surface location are calculated by obtaining the time differences at common receivers between adjacent field records. These delay times are then related to the elevation profile and a structural model is constructed using locally determined refractor and near-surface velocities.

Choice of the processing datum type and elevation can be important when processing data that are to be migrated. Preference should be given to a planar horizontal datum that is near the elevation of the acquisition. The large static shifts that may result

from a datum that is much different than the acquisition elevation may alter the shape of the NMO curve away from the hyperbolic curve used during velocity analysis. This is of particular concern when far offset data have been recorded. For this reason a datum of 1200 m above mean sea level was used for all lines processed, this being the average elevation of the seismic profiles recorded.

A reflection event from a shot record from line 12X is shown in Figure 3.6 and shows the improvement in the alignment of the event after application of the static corrections that were calculated by the time-difference method.

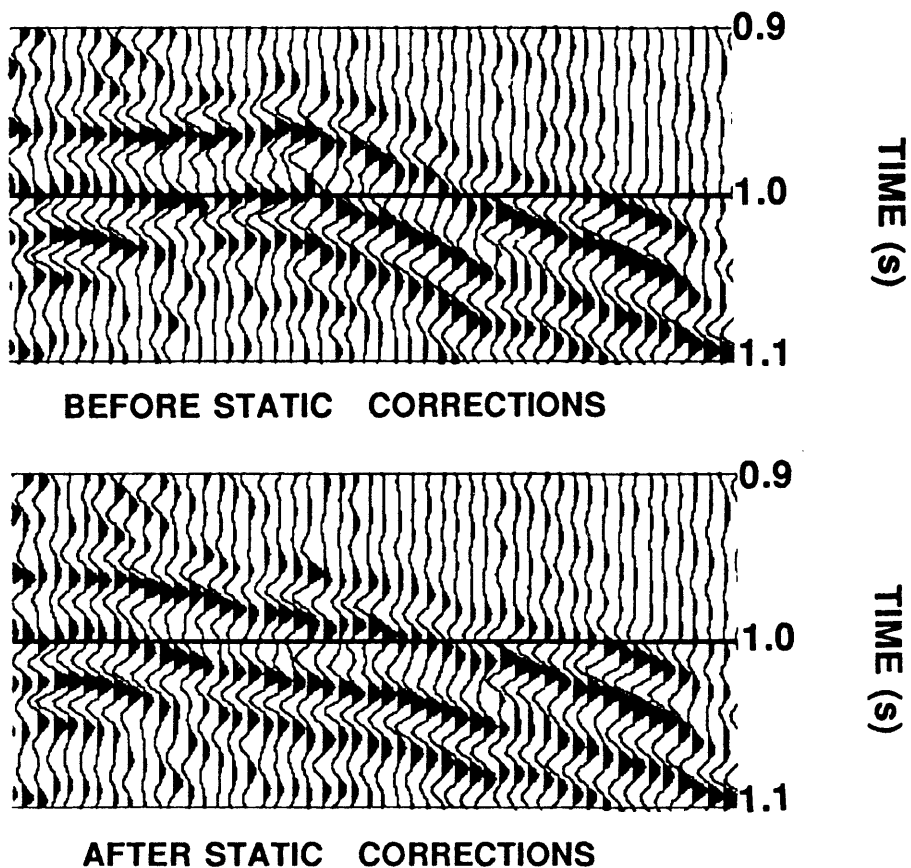


Figure 3.6 Close-up view of a reflection event from a shot of Line 12X that shows the improvement in alignment given by the static corrections.

3.6 Beam Steering

Beam steering of the shot records, one of the first and most important data manipulations done, significantly increased the coherency of the reflection data. Beam steering operates in the time-space domain on a localised basis, and has been shown to be effective in the reduction of noise on multichannel seismic data (Cheadle, 1988). Increasing the signal-to-noise ratio using this technique at an early stage in the processing sequence resulted in cleaner appearing and better resolved images, not only because of the attenuation of noise, but also from the more precise velocity functions and residual statics solutions made possible through the enhanced signal-to-noise ratio.

Beam steering is a type of delay and sum technique, of which Cheadle (1988) gives a thorough treatment. Only a brief description of the main steps of beam steering is offered here. For a given pivot trace, adjacent traces are time shifted in a linear manner and summed to form a time-slowness ($t-p$) panel. Linear events within the data window are mapped into points in the $t-p$ panel so that it represents a decomposition of linear events from the input panel. In this decomposition, a semblance value is calculated for each $t-p$ point (where semblance is defined as the ratio of input-to-output energy). It is used to identify the dominant slope for a given time sample of the pivot trace. The output trace, positioned at the pivot point, is constructed using the $t-p$ values selected by the semblance statistic. The net effect is to enhance those events in the data window that have maximum linear coherence. Furthermore, the rejection of events with a specified slowness is accomplished simply by omitting that slowness value in the initial

decomposition.

The key parameters of beam steering are the decomposition window width (in number of traces), and the maximum dip to pass (slowness or velocity units). Their selection is data dependent. To avoid a smeared appearance of the beam-steered data, smaller windows are preferable for data with significant reflector curvature. A window of less than 100 m width (generally five traces of data) was found to be optimum for the dataset. Data with slopes greater than those of the reflection events are generally noise-related (e.g., ground roll, surface wave, backscattering, etc.). The slope of coherent noise and reflections can be measured directly from the data and used to select a minimum velocity (or maximum dip) to consider in the decomposition. For the data used in this study, the velocity cutoff generally used was 4000 m/s. Prior to beam steering the data, it is important that trace-to-trace irregularities due to unresolved static corrections, or inconsistent trace-to-trace scaling, be removed. Furthermore, filter rejection of random noise will improve the correlations of the coherent signal. Therefore, prior to beam steering, the data were corrected for statics and bandpass filtered and had a trace balancing scalar applied.

The ability of beam steering to enhance coherent energy is illustrated in Figure 3.7 where an unfiltered record, its beam steered output and, for comparison, its $f-k$ filtered output are shown. Beam steering very clearly has improved the signal-to-noise ratio of the data, to an even greater extent than the $f-k$ filter has. This is probably because beam steering is a data-dependent operation, and one that acts on a localised, rather than global basis (as is generally the case with $f-k$ filtering).

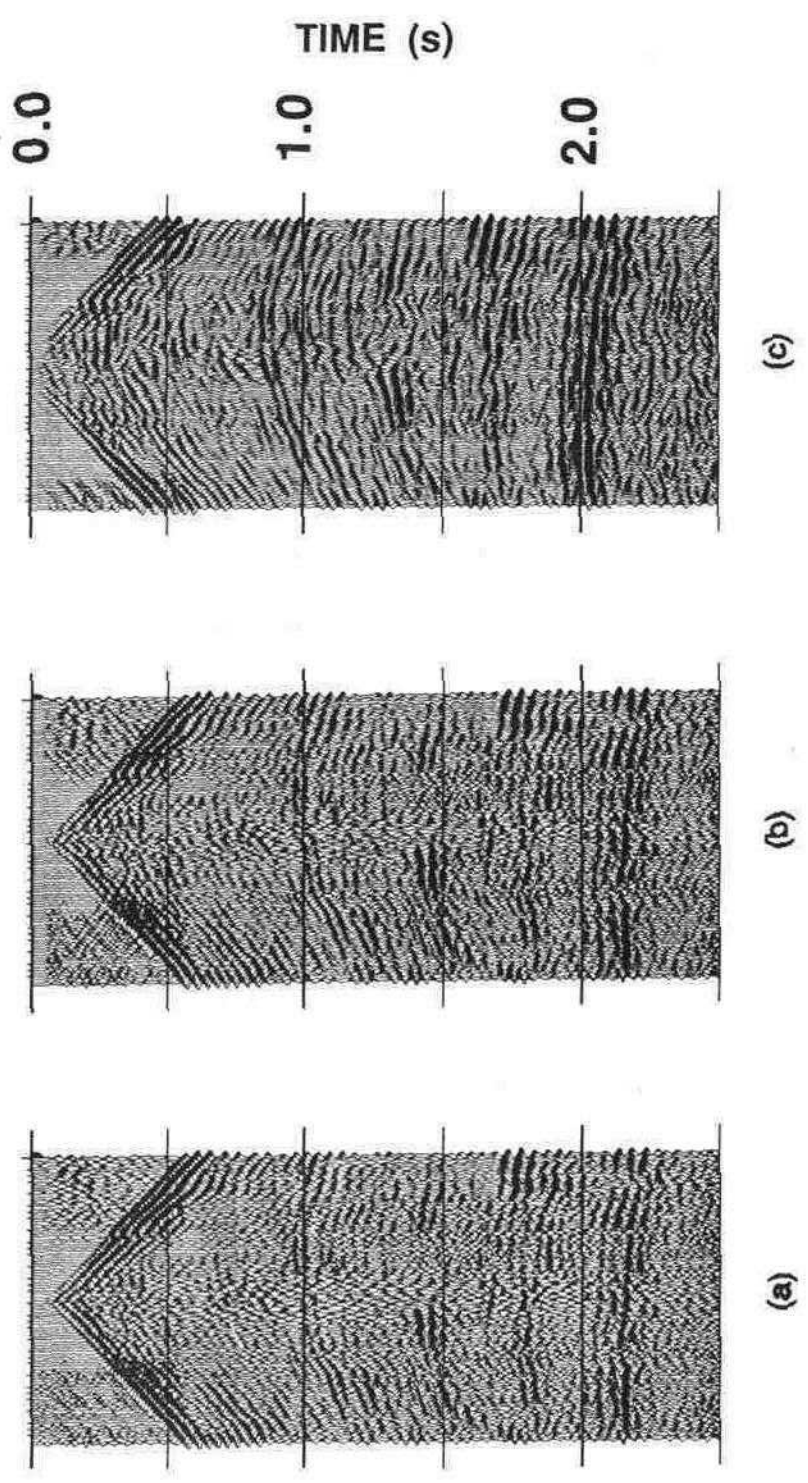


Figure 3.7 Shot record from Line 12X (a) before velocity filtering, (b) after f-k filtering and (c) after static corrections and beam steering, using apparent velocity of 4000 m/s as maximum dip passed.

An effective test of the results of a filtering operation is to compute the difference between the input and filtered output. The difference should only contain the noise targeted for rejection. The difference records corresponding to input and filtered output shown in Figure 3.7 are shown in Figure 3.8. While the $f-k$ filtered difference section has no evidence of signal leakage, some energy inside the passed dip range of the beam-steering process is evident. This is not desirable, and is probably an artefact due to a lack of adequate dip sampling in the beam-steering process, so that some valid components of the signal were not passed in the original decomposition. It may also be due to the large group interval of the filtered data (40 m). Despite this signal leakage, the results of the beam steering are still preferred because of the noise reduction achieved.

3.7 NMO and Residual Static Corrections

Normal moveout (NMO) velocities were picked from contour plots of constant velocity stacks at intervals of fifty common midpoint (CMP) bins. Residual statics were calculated using NMO-corrected CMP gathers. To maximise the accuracy of the velocity and residual statics models, the process was iterated, i.e., a second pass of velocity analysis was done after the initial residual static corrections were applied, and then a second pass of residual statics was run.

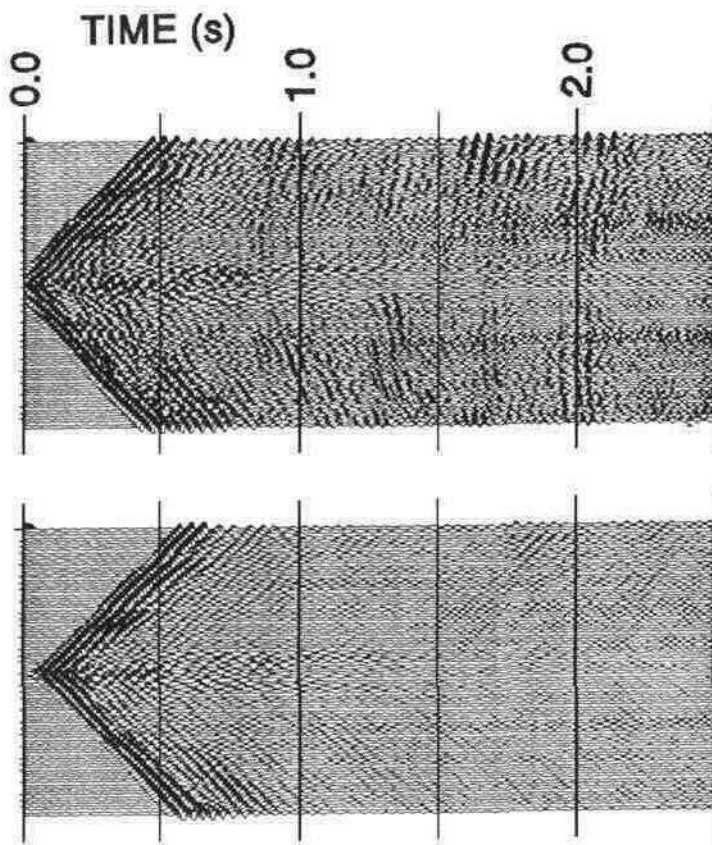


Figure 3.8 Difference records obtained by subtracting (a) $f-k$ filtered and (b) beam steered records, shown in Figure 3.7, from their respective unfiltered versions.

3.8 Imaging

Stacked seismic data give a distorted view of a structurally complex geological section and need to be imaged, or focused, using seismic migration techniques. The seismic data were migrated using a technique described by Stolt (1978) that migrates data in the Fourier domain. The key parameter of seismic migration is the specification of the velocity model. In migrating the data of the triangle zone in the study area, it was found that a simple velocity model gave the best results. Each model was defined by approximately three velocity functions, and each velocity function had a mildly increasing gradient that was based upon the local geology. The velocities used were in general between 60% and 80% of the well-log rock velocities. The simple-model approach is successful in the study area because the velocities do not vary greatly within the triangle zone, despite the complex structure.

Substantial enhancement of the coherent signal of the migrated data was obtained by using f - x linear prediction filtering. This is a method of random-noise attenuation that, on a localised basis, attempts to decompose a window of seismic data into linear events, and then attempts to enhance those events with linear coherency. A review of the method is given by Harrison (1990). Figure 3.9 is an example of migrated data from Line 18XC before and after f - x filtering. It shows the improvement in the clarity of the reflections gained by this filtering operation.

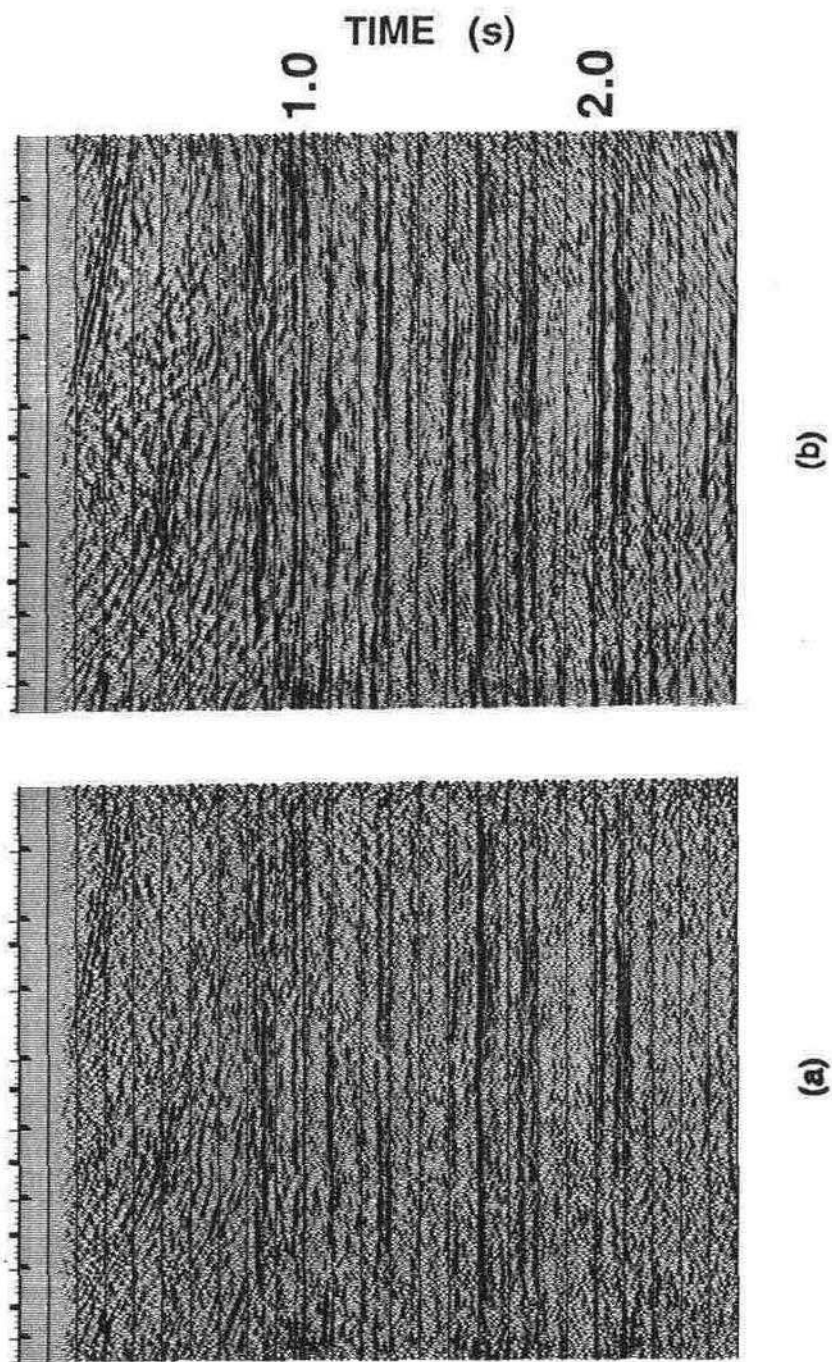


Figure 3.9 Portion of migrated data of Line 18XC before (a) and after (b) linear prediction filtering.

Chapter 4 Seismic Interpretation

4.1 Introduction

In this chapter a line-by-line description and interpretation of the seismic data are presented. The profiles are presented in a south-to-north sequence that follows the triangle zone along the regional structural strike. The data were interpreted by using well control to correlate reflection events where well control was available, surface control from a geology map, and the standard time intervals between the major events shown by the seismic trace synthesised from the sonic log of the at 6-18-27-4W5 well, shown in Figure 4.1.

4.2 Line CX91

The migrated data of line CX91 (Figure 1.2) are displayed, in time, in Figure 4.2. This and the other seismic sections shown in this chapter are displayed with the horizontal scales approximately equal to the corresponding vertical scales for the velocity of 3800 m/s used to plot the data. It can be seen that the overall data quality is good with many strong reflections apparent. Two boreholes located in key locations along this profile give excellent control on the reflection correlations, which are annotated in the interpretation of CX91 shown in Figure 4.3.

The upper detachment is interpreted to underlie gently east-dipping reflections

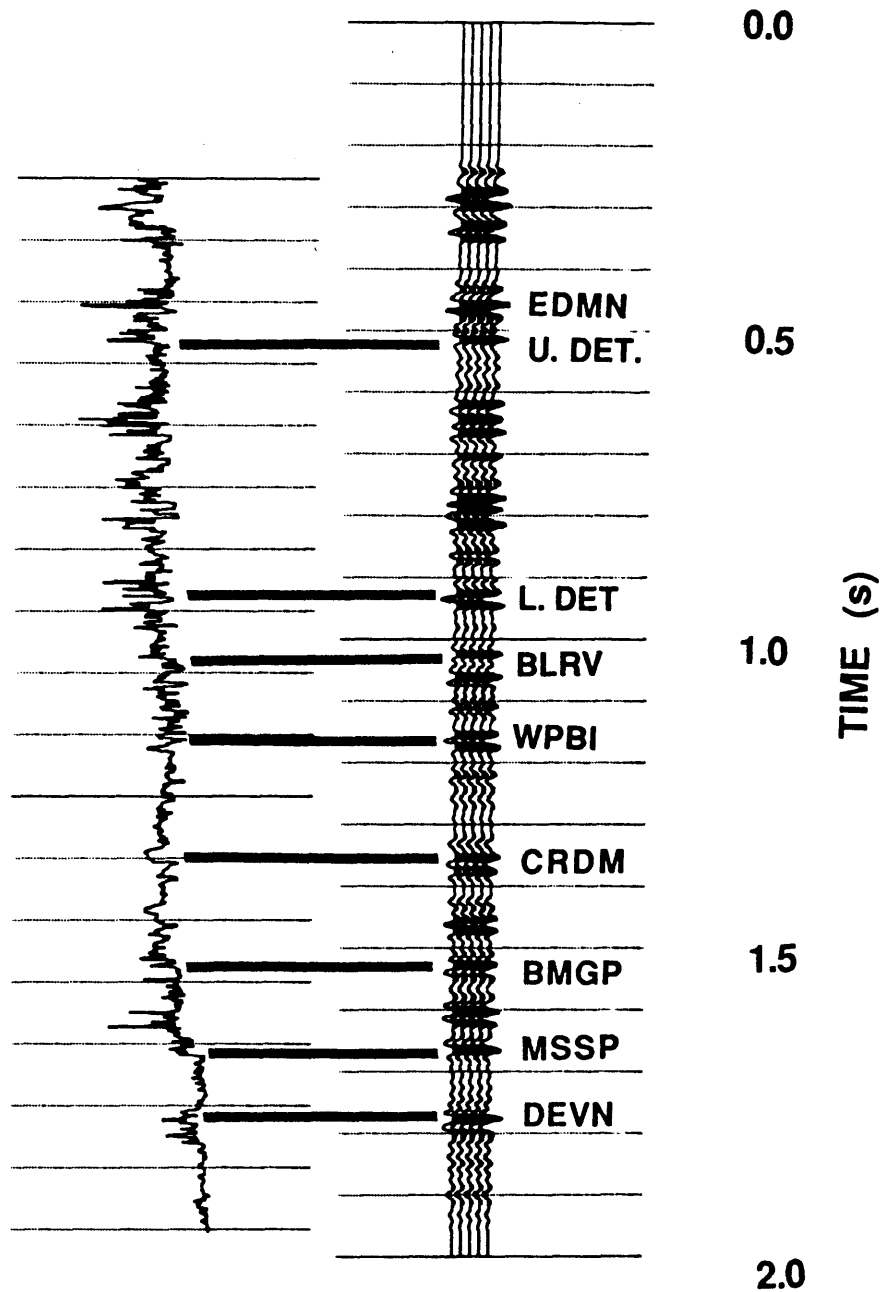


Figure 4.1 Synthetic seismic trace (right) produced from sonic log (left) at well 6-18-27-4W5. EDMN is Edmonton Gp., and WPBI is Wapiabi Fm. See Figure 4.2 for explanation of other abbreviations. *After* Lawton and Spratt (1991).

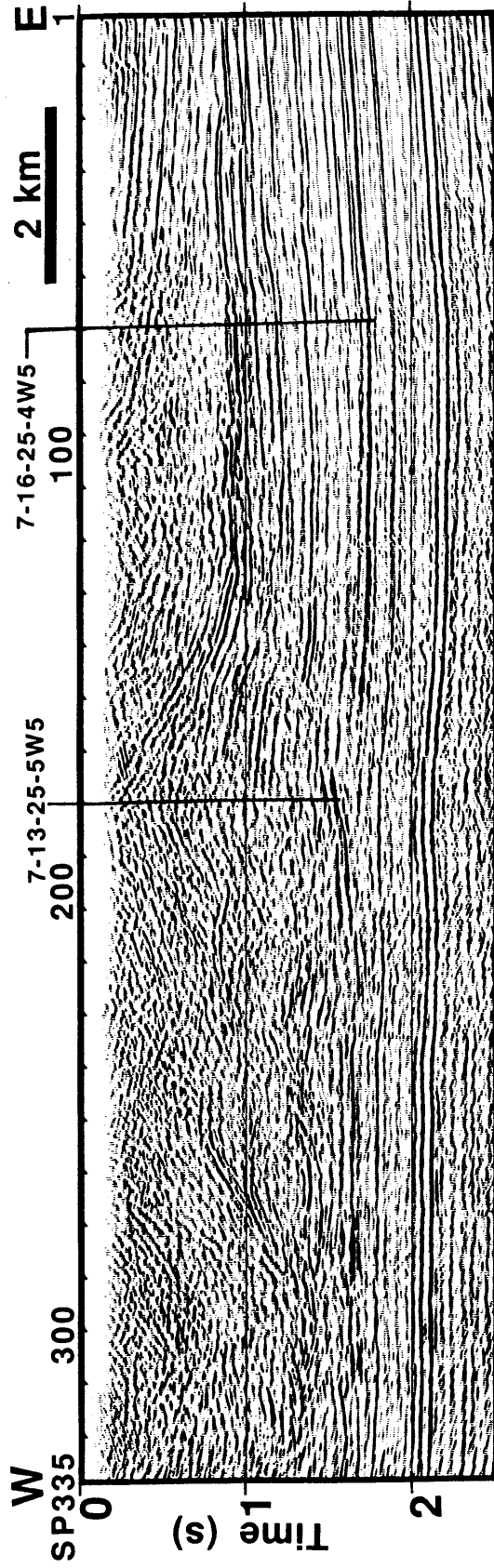


Figure 4.2 Migrated final section of Line CX91. Well locations are annotated.

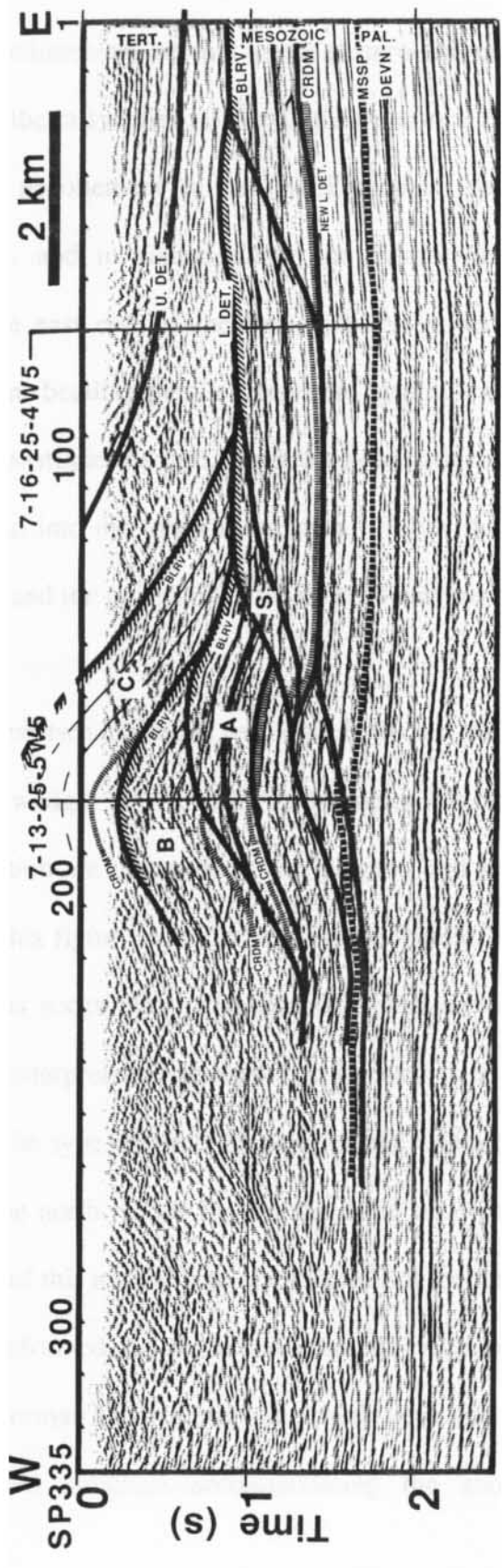


Figure 4.3 Interpretation of Line CX91 (Figure 4.2), with Tert.=Tertiary, U.DET.=Upper Detachment, L.Det.=Lower Detachment, BLRV=Belly River Fm., CRDM=Cardium Fm., MSSP=Mississippian, DEVN=Devonian and PAL.=Paleozoic.

from the Tertiary sedimentary section at the eastern end of the profile. This marks the west flank of the Alberta syncline. Later in the section, a basal fault is interpreted to cut upsection from a decollement in the Mississippian Banff Formation, through the Cretaceous section, and to flatten under the Edmonton Group in the Belly River Formation. At the east end of the line both the upper and lower detachments are interpreted to become bedding-parallel; however, no single branch point is clearly evident. These two faults constitute the two important boundaries of the tectonic wedge of rock that has been forced into the foreland molasse. Below the lower detachment the rocks are autochthonous, and the rocks above the upper detachment have merely been displaced vertically.

Between these two important bounding faults are the somewhat chaotic reflections within the tectonic wedge. Three major fault blocks that include Kootenay Formation to Belly River Formation are interpreted to be present, and are labelled "A", "B", and "C" in Figure 4.3. In this figure is a relatively minor feature labelled "S", which is a small sliver of Cretaceous rocks which has slight displacement in the footwall of the main assemblage. This interpretation is supported by well data (location 7-13-25-5W5), and is consistent with the type of structure seen on the seismic data of Line 12X and Line 18XC, further to the north, which have imaged the structural assemblage much better.

To the east of this assemblage, the footwall of the upper detachment is interpreted to contain highly deformed and thickened Edmonton Group rocks that have been pushed ahead of the antiformal stack along the lower detachment. Given what is clearly a complexly contorted structure accommodating the shortening beneath the upper

detachment, the apparent smoothness of the upper detachment is remarkable.

Near the east side of the line, a fault is interpreted to cut upsection from a flat in the Blackstone Formation to merge with the older lower detachment below the Edmonton Formation. Just east of the main culmination at the level of the Cardium Formation, underthrusting has locally lifted and tilted eastward the footwall cut off by this thrust. Furthermore, the Cardium in the footwall of this thrust fault has been duplicated along a detachment in the Blackstone Formation, indicating that the bedding-parallel thrust continues into the foreland beyond the easternmost thrust ramp.

Visible on the west end of the profile, west of the region of the antiformal stack, are west-dipping reflections typical of the Foothills Belt, although the image is poorly resolved. This can be attributed largely to the wide group interval used in the acquisition of the data (50 m), which has biased against the recording of steep dips from shallow depths.

The case for thin-skinned structuring, generally accepted in the Foothills (Dahlstrom, 1969), appears not to be challenged by the interpretation in this area. Below the basal fault, the reflections are relatively flat and appear undisturbed except for an apparent seismic pull-up anomaly below the main culmination.

4.3 Line 12X

The migrated data of line 12X (Figure 1.2) are displayed, in time, in Figure 4.4, with an interpretation of these data shown in Figure 4.5. The overall data quality is

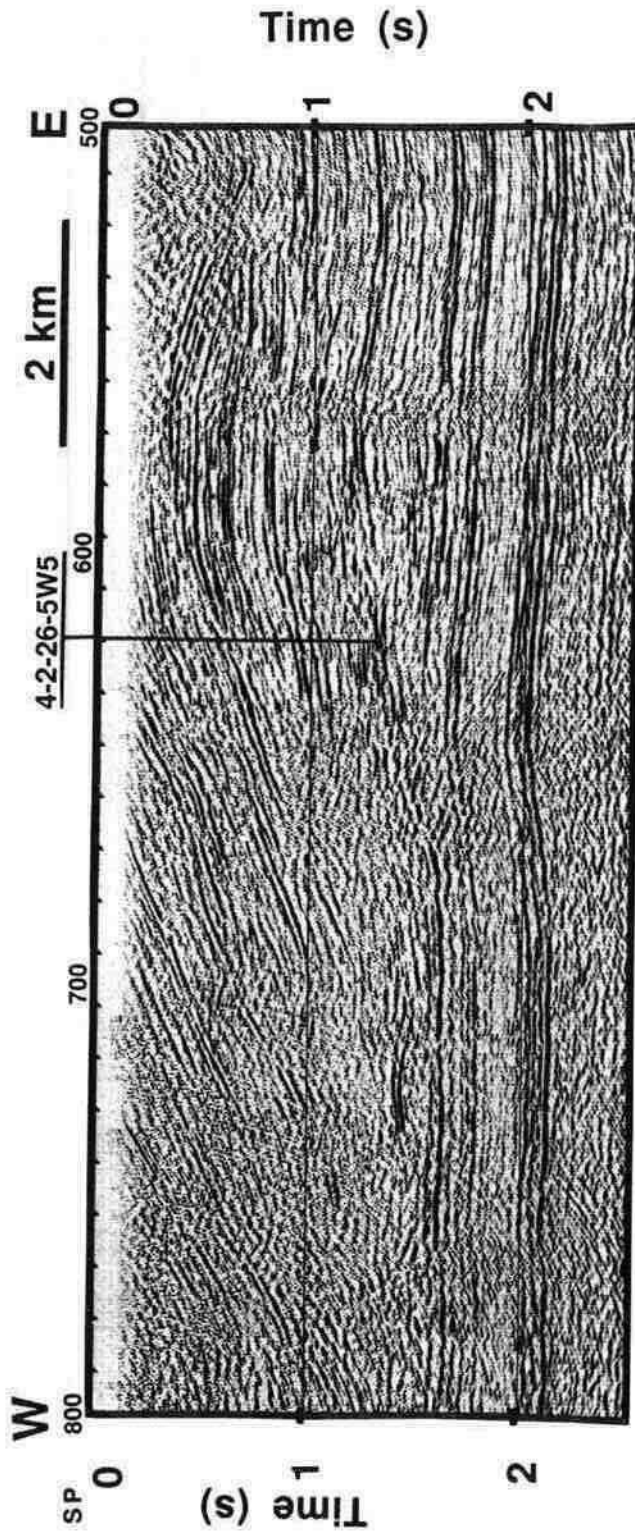


Figure 4.4 Migrated final section of Line 12X.

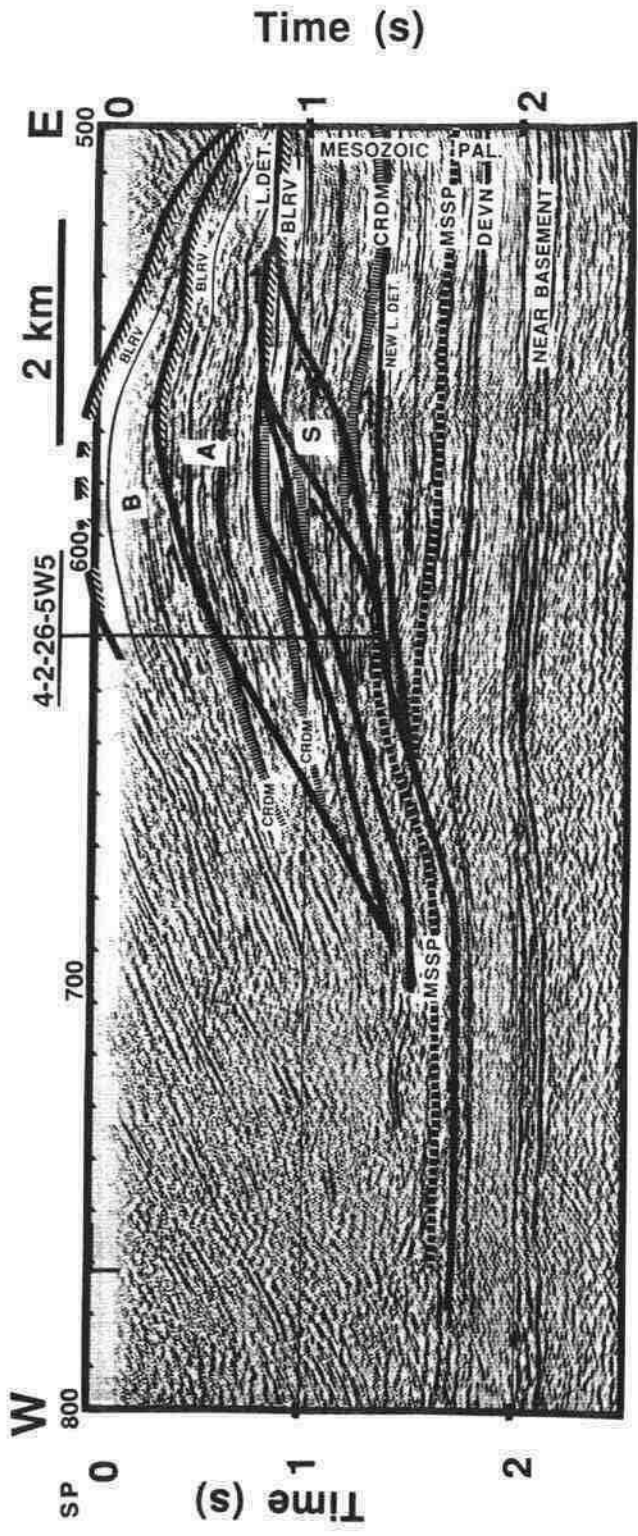


Figure 4.5 Interpretation of Line 12X.

excellent and it can be seen that this line is notable for its clear image of the antiformal stack and the west-dipping reflections on the west side of the frontal structure. Control on the reflection correlations is provided by one well (4-2-26-5W5) just west of the main culmination, as well as surface data, and the known standard time intervals of the major stratigraphic intervals identified from the synthetic trace shown in Figure 4.1.

Strong continuous west-dipping reflections are observed at the west end of the seismic line. These west-dipping reflections gently roll into an antiformal package of reflections towards the eastern end of the section, marking the location of the main culmination. Strong subhorizontal reflections, interpreted to be from autochthonous footwall strata, are visible at the eastern end of the line.

Two major fault blocks are interpreted to constitute the main culmination seen on this line. The "A" and "B" blocks identified on Line CX91 (Figure 4.3) can be correlated with the fault blocks seen in this profile. A small sliver of Cretaceous rocks under the east side of the main culmination (the "S" block) correlates with that seen on the Line CX91. The lowest fault block (that which involves Mississippian rocks) is interpreted to carry Cardium rocks as well, whereas on Line CX91 the roof thrust of the fault block followed near the top of the Blairmore Group. As a result, in Line 12X the "A" fault block carries less Cardium Formation than it does the overlying Belly River Formation.

Underthrusting has locally lifted and rotated the Cardium under the east side of the main culmination, as is also seen on Line CX91. This suggests that a bedding-parallel detachment underlies the Cardium and feeds shortening to the east, as interpreted on Line CX91.

Footwall cutoffs of the "A" thrust sheet in the main culmination are well-imaged below at well 4-2-26-5W5, at approximately 0.5 s allowing for a complete definition of this fault block.

Due to the inadequate eastward coverage of this line, the upper detachment and its hangingwall rocks have not been imaged.

4.4 Line 18XC

The migrated data of the east-west profile, 18XC are displayed, in time, in Figure 4.6 and interpreted in Figure 4.7. This line is located approximately three kilometres north of Line 12X, on the 1A highway just north of the Bow River (Figure 1.2). These data, acquired with the same parameters as line 12X, are noisier than 12X, but their overall data quality is reasonably good. Reflection correlations are controlled by two wells that have been projected approximately 800 m into the line of section (Figure 1.2), as well as from surface data and the known standard time intervals (Figure 4.1). Shotpoint 570 is near the southern end of Line FS86-1.

The seismic section from Line 18XC (Figure 4.7) provides an important image of hangingwall cutoffs against the lower detachment in the region of the tectonic wedge - one that is not as clearly visible on the other dip lines of this dataset. These hangingwall cutoffs can be seen as east-dipping reflections of the "B" sheet (Figure 4.7) that terminate against flat reflections at approximately 0.8 s, in the region of shotpoint 550. The two sheets labelled "A" and "B" correlate with the two sheets seen on Lines CX91 (Figure

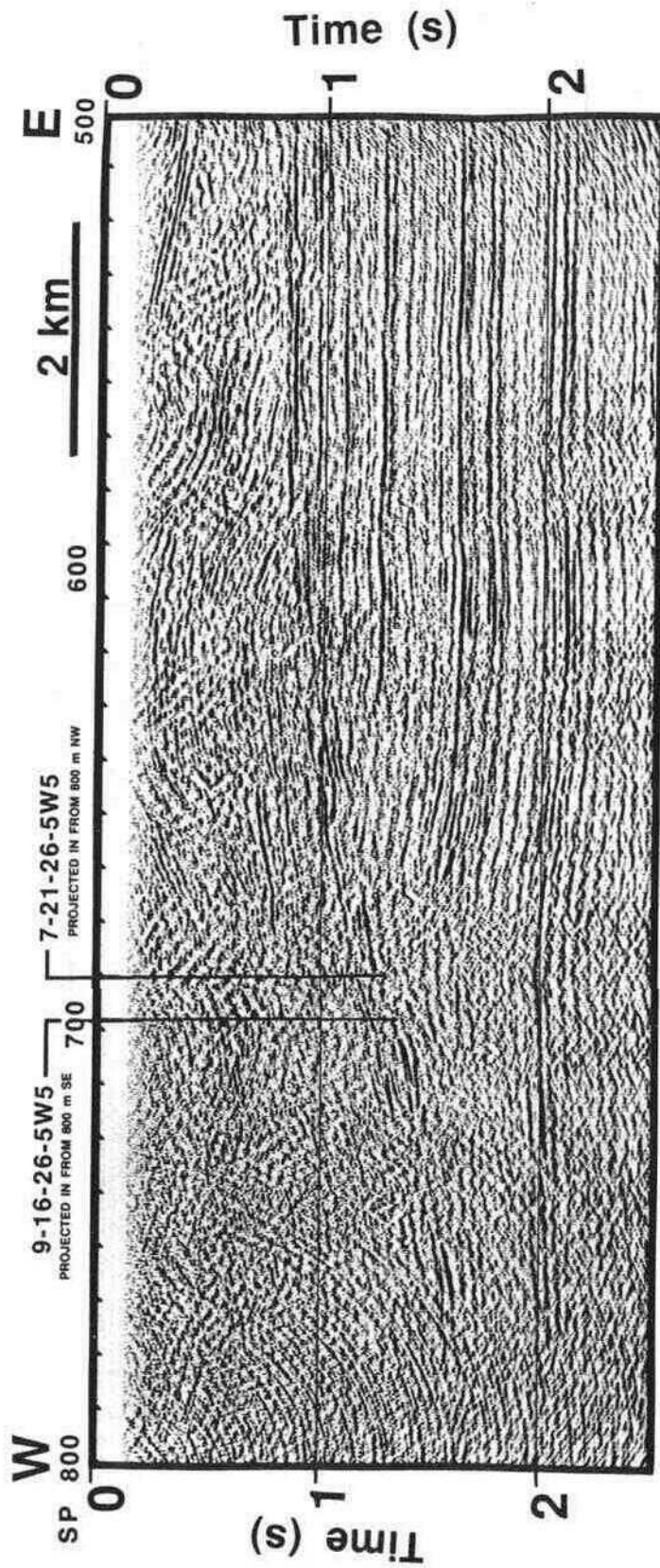


Figure 4.6 Migrated final section of Line 18XC.

Time (s)

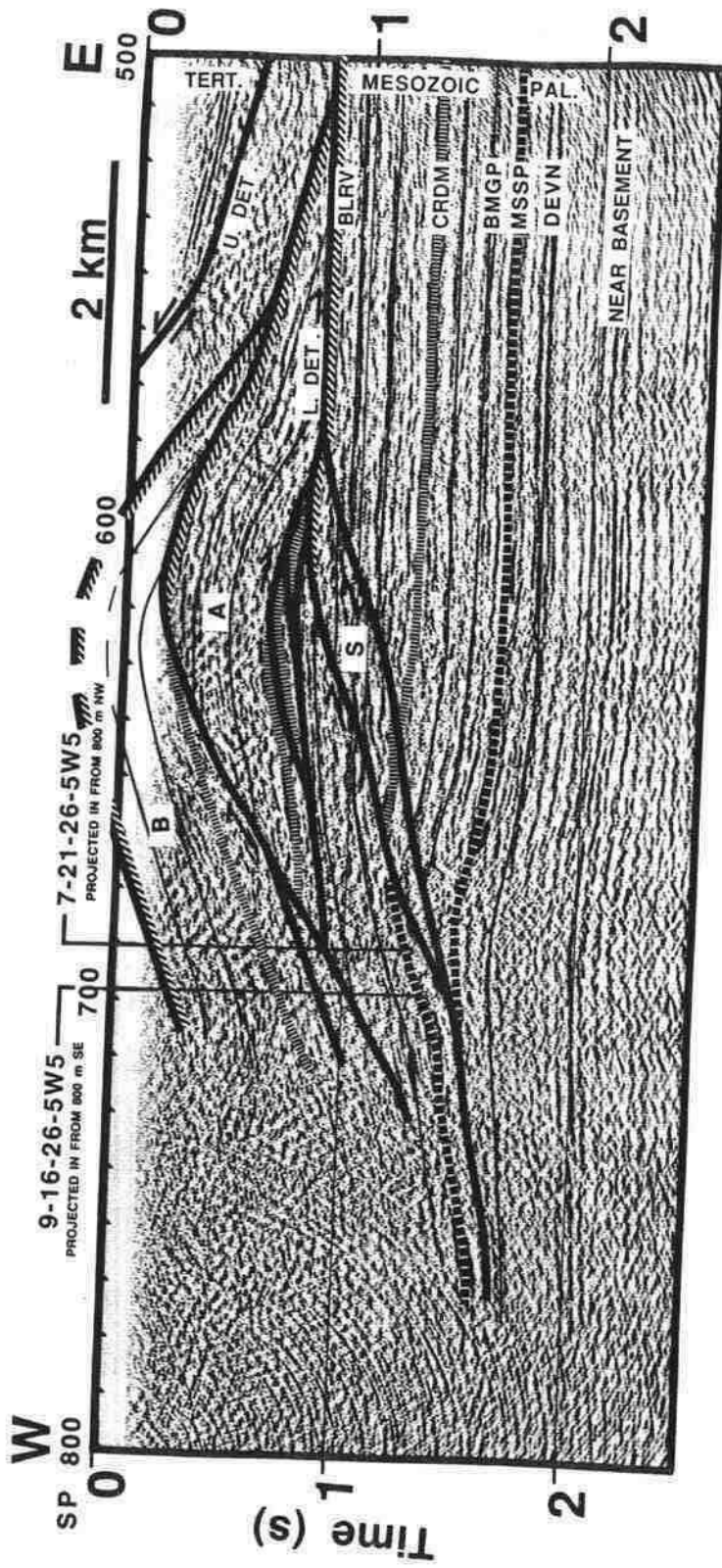


Figure 4.7 Interpretation of Line 18XC.

4.3) and 12X (Figure 4.5), as does a small sliver of Cretaceous section, labelled with an "S".

Strong parallel reflections interpreted to represent relatively unstructured strata are observed at the eastern end of the seismic section. Unlike Lines CX91 and 12X, there is no evidence for a bedding-parallel detachment in the Blackstone Formation east of the main culmination. Early in the section at the east end of the line, high-amplitude east-dipping reflections of the Tertiary strata can be seen. Between these two packages there is a zone of discontinuous reflections representing part of the tectonic wedge which is interpreted to comprise highly deformed Edmonton Group strata. Reflections that terminate against the planar Belly River event (near shotpoint 550 at 0.8 s) are interpreted to be hangingwall cutoffs of the Wapiabi through Belly River formations.

4.5 Line FS86-3 and FS84-1

Figure 4.8 from Lawton and Spratt (1991) shows a seismic profile that was composed by splicing together lines FS86-3 and FS84-1. The profile crosses the Wildcat Hills, approximately five kilometres north of Line 18XC (Figure 1.2). This line was processed in part by the author, and is included in this thesis because it is located in the study area. The structure is interpreted to be broader here, which is consistent with an overall south-to-north broadening of the triangle zone in the thesis area. Mississippian rocks have not been imaged as they are no longer directly involved in the main culmination.

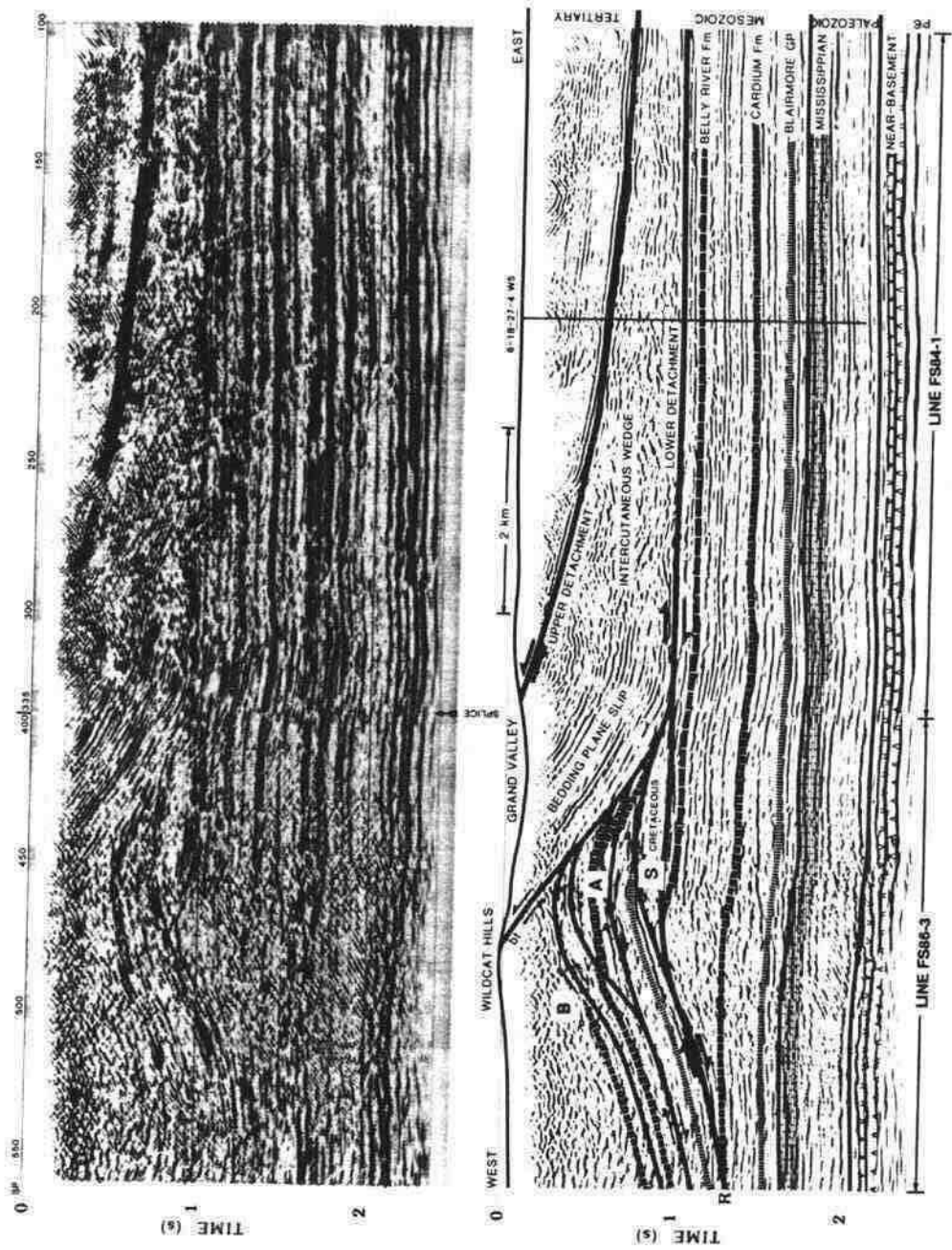


Figure 4.8 Migrated seismic data and interpretation of Lines FS86-3 and FS84-1, from Lawton and Spratt (1991).

The "A" thrust sheet seen on Line 18XC correlates with the main thrust sheet constituting the main culmination on this line. This thrust has considerably more displacement here, however, with the Blairmore Formation interpreted to rise above the Belly River Formation. The sliver of Cretaceous rocks interpreted on the other three dip profiles, CX91 (Figure 4.3), 12X (Figure 4.5) and 18XC (Figure 4.7), labelled with an "S", is interpreted to lie in the footwall of this main thrust sheet.

As with Line CX91 (Figure 4.3), the upper and lower detachments do not merge at a branch point within the eastward extent of the seismic profile. Similar to Line 18XC (Figure 4.7) and Line CX91 (Figure 4.3), there is no evidence of a Blackstone level detachment to the east of the main culmination.

4.6 Line FS86-1

This line, shown in Figure 4.9 with an interpretation shown in Figure 4.10, is a very good-quality strike line that ties at its southern end with Line 18XC and at its northern end with Line FS86-3. It images a longitudinal cross-section along regional strike in front of the main culmination. It shows that the intercutaneous wedge, which contains Wapiabi to Belly River Formation strata, sits on the lower detachment and maintains a profile free of variation along the strike of the structure.

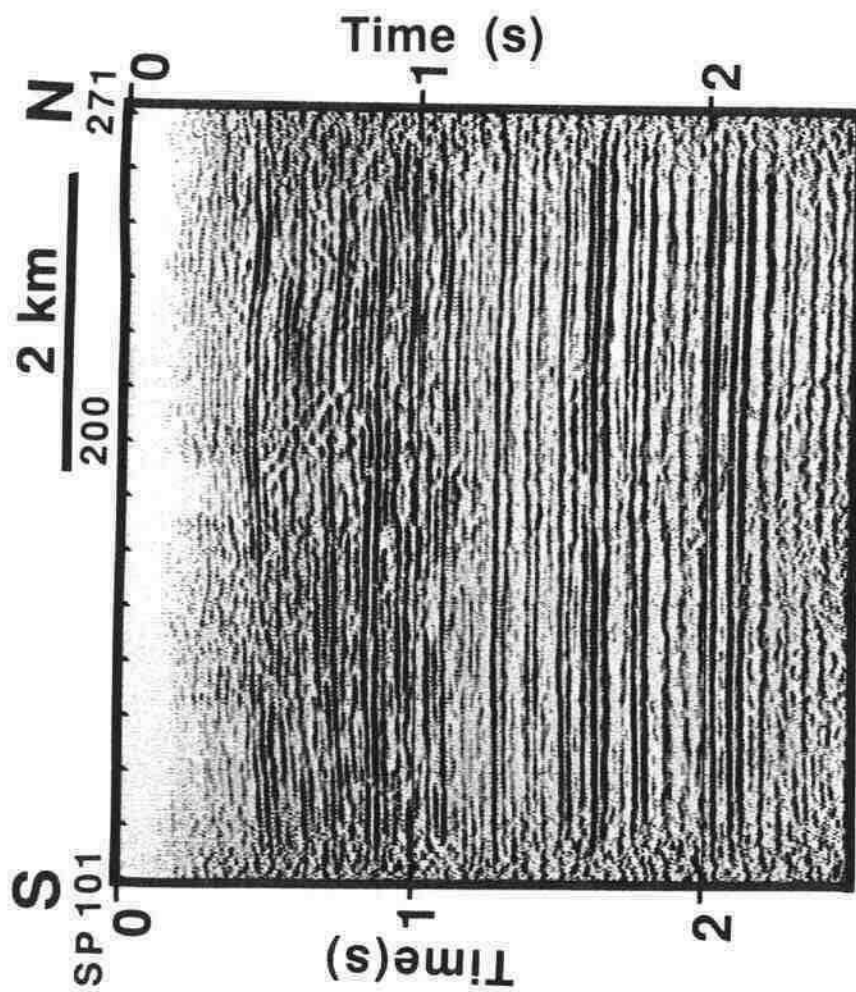


Figure 4.9 Migrated final section of Line FS86-1.

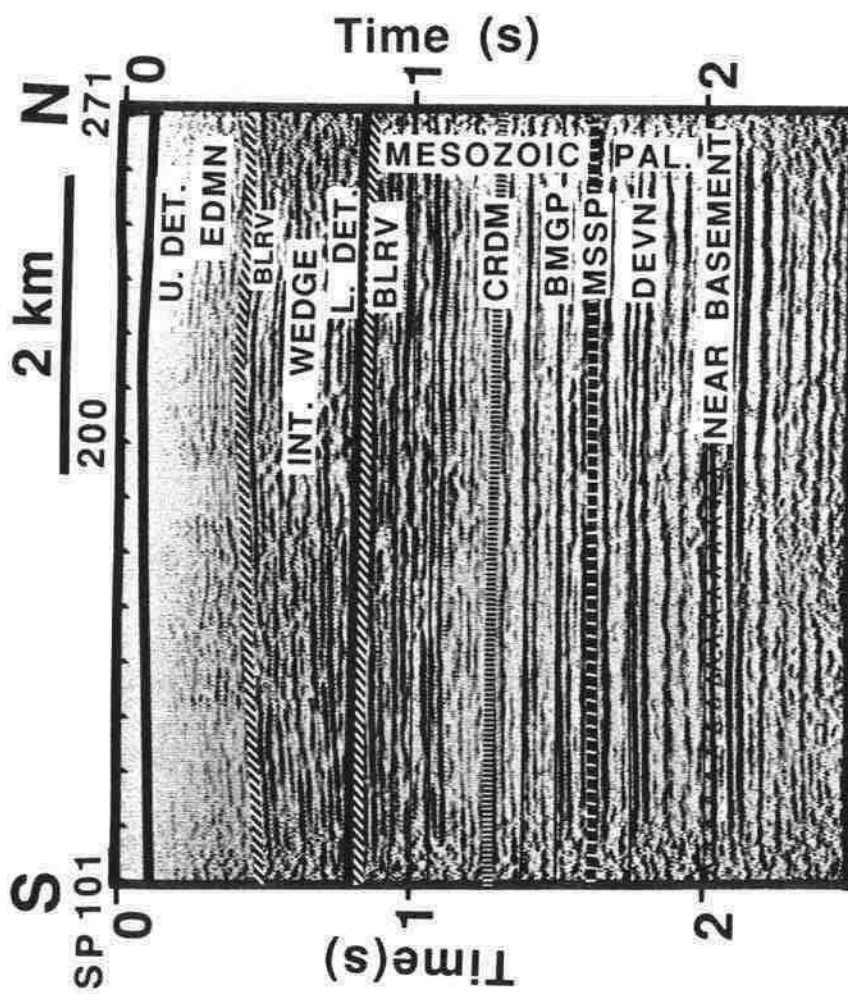


Figure 4.10 Interpretation of Line FS86-1

4.7 Line FS85-1

This is a good-quality line that continues along strike from FS86-1 (Figure 1.2). It is shown in Figure 4.11 (with an interpretation shown in Figure 4.12) and ties the west end of line FS84-1 at shotpoint 291. The Cardium and deeper reflections appear flat and continuous across the section. Some deformation is apparent at the shallower depths within the intercutaneous wedge, at the northern end of the line. However, the wedge displays little structural variation along the southern end of the line. This is important, because it suggests that the splicing of Lines FS86-3 and FS84-1 (the interpretation of which is given in section 4.4) should not have introduced errors in the structural interpretation.

4.8 Line FS86-2

This short north-south line (Figure 1.2) is shown in Figure 4.13, with an interpretation shown in Figure 4.14. It is oriented obliquely to regional strike, and it images the upper and lower detachments, the intercutaneous wedge, and autochthonous Mesozoic and Paleozoic stratigraphy. As the profile is oblique to the regional strike, a component of the true NE dip of the upper detachment has been imaged.

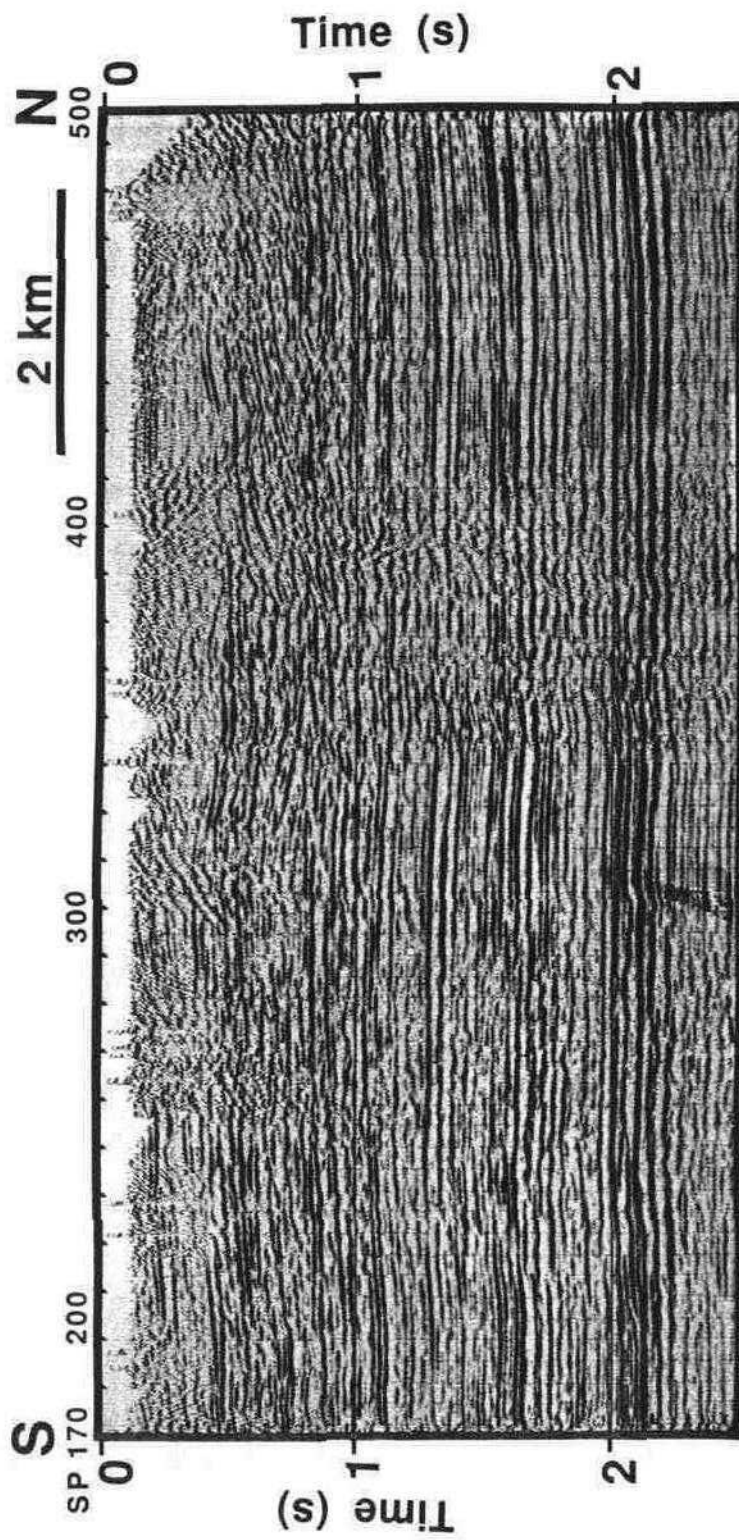


Figure 4.11 Migrated final section of Line FS85-1.

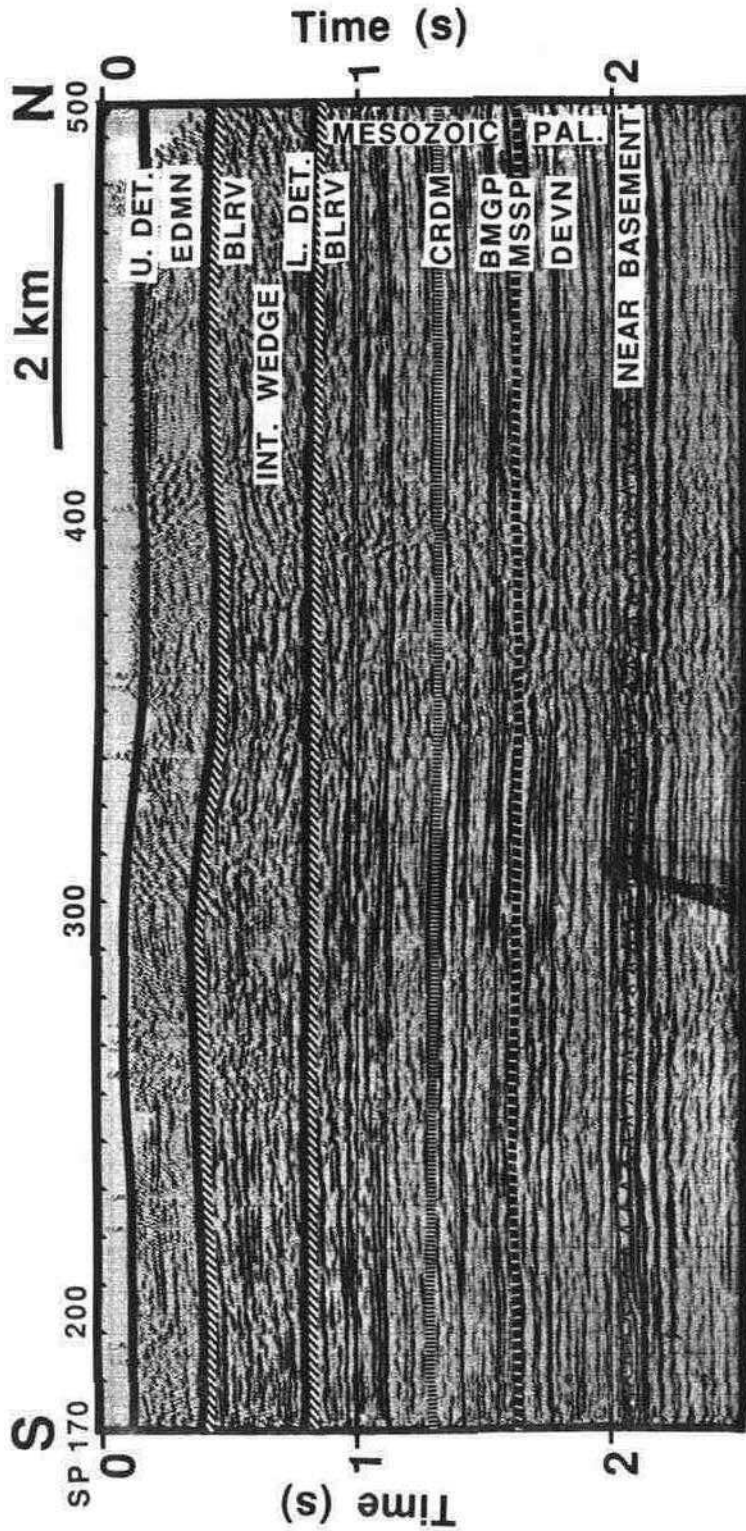


Figure 4.12 Interpretation of Line FS85-1.

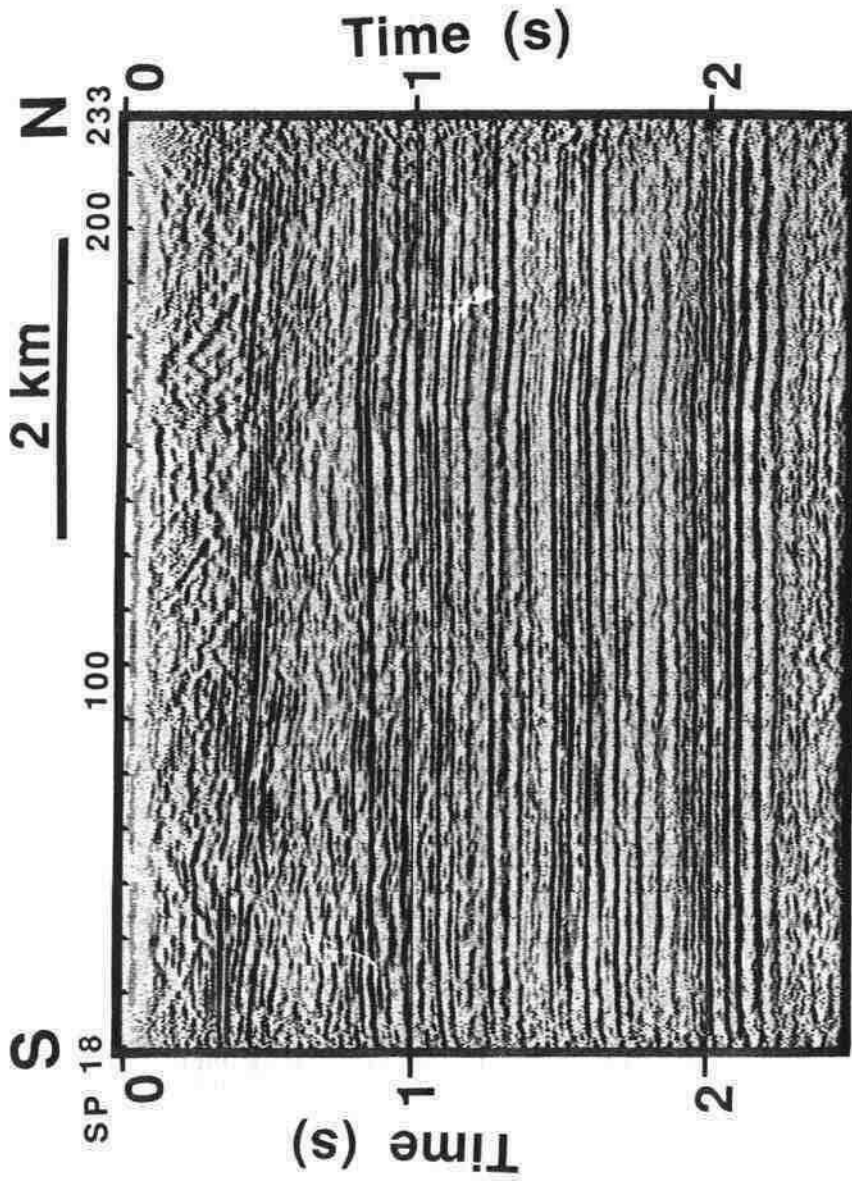


Figure 4.13 Migrated final section of Line FS86-2.

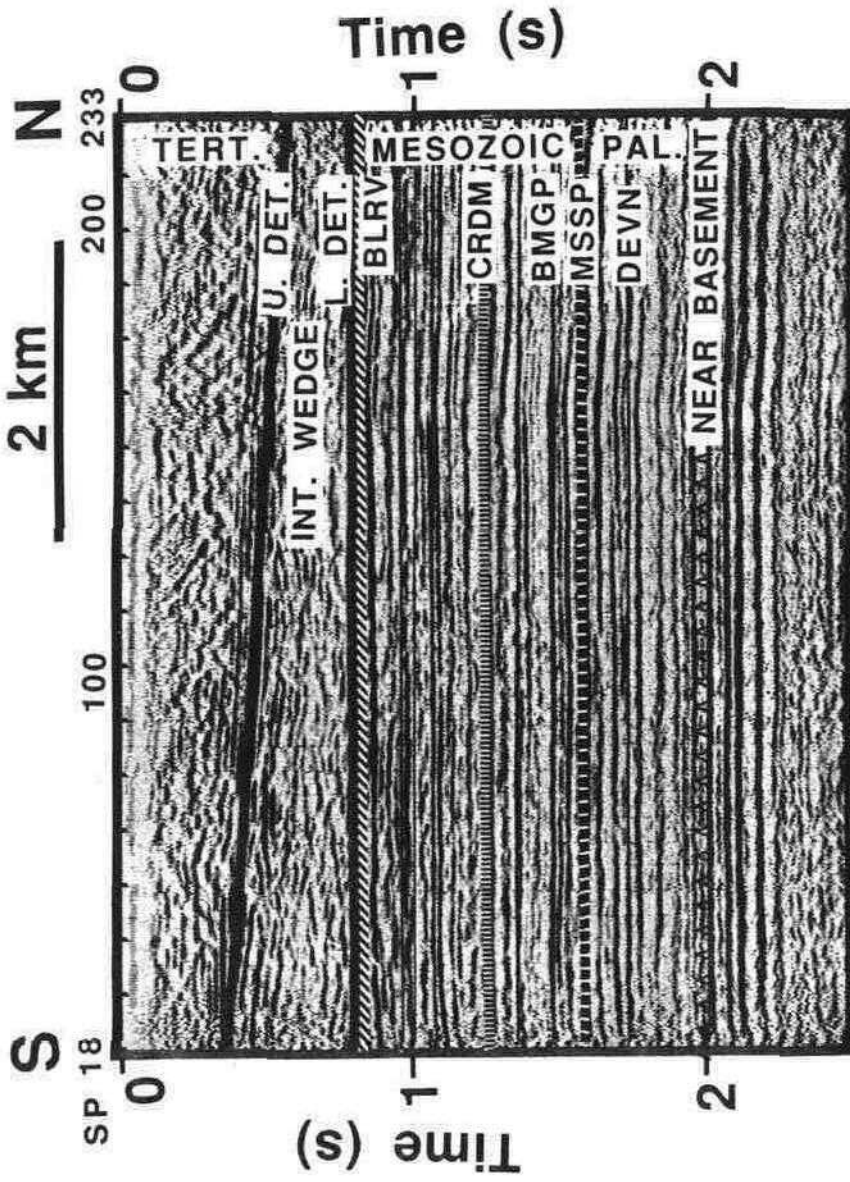


Figure 4.14 Interpretation of Line FS86-2.

4.9 Pull-up Anomalies

Pull-up anomalies provide important evidence for duplication of the carbonate rocks in the Alberta Foothills. The pull-up anomaly visible beneath the main culmination seen on Lines CX91 (Figure 4.3), 12X (Figure 4.5), and 18XC (Figure 4.7) is attributed to both duplication of the carbonate rocks of the Paleozoic section and to duplication of rocks of Lower Cretaceous and early Upper Cretaceous age, which have higher velocities than the overlying Upper Cretaceous and Tertiary sedimentary section (Figure 2.1).

Equation 4.1 is a simple equation that relates seismic reflection traveltime anomalies to velocity and the thickness of duplication for a dual-velocity medium:

$$\Delta t = 2\Delta d \left(\frac{V_2 - V_1}{V_1 V_2} \right) \quad (4.1)$$

where Δt is the traveltime anomaly, Δd is the thickness of the interval causing the velocity anomaly, and V_1 and V_2 are the velocities of normal and structured intervals respectively. Given $V_1 = 4000$ m/s and $V_2 = 6000$ m/s, Equation 4.1 can be rearranged to give a useful guide for estimating the amount of carbonate duplication from the corresponding velocity pull-up in the southern Alberta Foothills:

$$\Delta d = 6000 \Delta t. \quad (4.2)$$

Using a value of 0.050 s for the typical velocity anomaly due to the carbonate rocks in the hanging wall of the basal thrust, the duplication is calculated to be 300 m. The velocity anomaly observed on Lines CX91 (Figure 4.3), 12X (Figure 4.5) and 18XC (Figure 4.7) is up to 0.110 s. This additional velocity anomaly is attributed to the erosion of the Tertiary layer. The velocity anomaly due to Cretaceous strata replacing Tertiary strata across the profile can similarly be calculated. Using values of 3500 m/s and 4000 m/s for the velocities of the Tertiary and Cretaceous rocks, respectively, and a thickness of 1000 m for the uplifted and eroded Tertiary, a velocity anomaly of 0.070 s is calculated. It is interesting to note that a seismic velocity anomaly of approximately this magnitude can be observed on the Wildcat Hills profile (Line FS86-3) where no allochthonous carbonate rocks are imaged. Therefore, in the interpretation of seismic data from the triangle zone it is important to exercise caution when interpreting the source of velocity anomalies.

Chapter 5 Gravity Analysis

5.1 Introduction

Interpretation of the short-wavelength characteristics of the Earth's gravitational field can provide information about subsurface density distributions. In the Alberta Foothills, there exists a significant contrast of density between the predominantly calcareous rocks of Paleozoic age and the predominantly clastic rocks of Mesozoic age. Two gravity surveys were acquired, processed, and interpreted with the aim of evaluating the utility of the gravity method for delineation of Mississippian carbonate rocks carried in thrusts in the Foothills. In this chapter, gravity data are interpreted to reveal carbonate involvement in the Jumpingpound-Wildcat structure. Furthermore, it is shown that gravity measurements are most useful when used to supplement other more detailed data (e.g., seismic data) for Foothills exploration.

The discussion of the gravity work is divided into four main components: acquisition of approximately eighteen kilometres of gravity data along two cross-strike profiles, completed in the autumns of 1988 and 1989; reduction of the data to relative Bouguer Anomaly status; development of Fortran computer programs designed to isolate the anomaly of interest, and; interpretation of the data, primarily by iterative computer-aided modelling.

This chapter presents, in the following order: a density tabulation; the field procedure; the data reduction; the anomaly isolation; an interpretation; an error analysis;

and a discussion of the results.

5.2 Study Area Density Values

Well data show a significant separation between the densities of the Cretaceous clastic rocks and the Paleozoic carbonate rocks. Averaged densities of 2400 kg/m^3 and 2640 kg/m^3 were estimated for the Cretaceous and Paleozoic rocks, respectively, and were used in the gravity modelling. Using a large database of wells in the western Canadian basin, Maxant (1975) published similar mean values: 2420 kg/m^3 for sandstones, 2460 kg/m^3 for siltstones, 2430 kg/m^3 for shales, and 2630 kg/m^3 for limestones. Paukert (1982) also determined similar values from southern Alberta: 2250 kg/m^3 (Upper Cretaceous clastics above Milk River sandstone), 2490 kg/m^3 (Upper Cretaceous clastics below Milk River Sand and Lower Cretaceous clastics), and 2650 kg/m^3 (Paleozoic carbonates).

5.3 Fieldwork Description

Relative gravity measurements were made using a Worden Master Gravity meter. Elevation data were acquired using a Wild theodolite and EDM instrument and were converted to absolute elevations above mean sea level using local Geodetic Survey of Canada bench marks.

Data were acquired at ninety metre intervals, primarily along road allowances or

across pasture. The locations of the profiles are indicated in Figure 1.2. A minimum of three measurements were made at each station, from which an average value was used. Base station readings were taken every two hours for instrument drift and tidal corrections. Terrain corrections were necessary due to the nonhorizontal terrain in the study area (maximum relief is approximately 125 m). Topography was therefore estimated in concentric compartments of radii 17 metres, 50 metres, and 150 metres for subsequent terrain corrections at each station.

5.4 Gravity Reduction

Static and dynamic variations were removed in three steps to reduce the data to relative Bouguer Anomaly status, the standard for interpreting land-based gravity data. The data analysis procedure used is summarised in Table 5.1.

Table 5.1 Gravity profile data analysis sequence.

field measurements
(average of three measurements used)

dynamic variation correction
(normalisation using base station readings)

terrain corrections

reduction to Bouguer Anomaly

regional-residual anomaly separation

interpretation

Prior to their interpretation, gravity data must be reduced to remove the static and dynamic fluctuations inherent in their acquisition, as they can overwhelm the gravity responses of interest. Dynamic variations result from field conditions, and some important examples are instrument drift, and earth and moon tides. Important examples of sources of static deviations are variations of elevation, latitude, and terrain.

Base station readings were used to normalise and thus remove the dynamic variations. Terrain corrections were applied using the technique of Hammer (1939). For each compartment for which the terrain was estimated, the gravity effect was calculated using the relationship:

$$\delta g = G\rho\phi[r_2 - r_1 + \sqrt{r_1^2 + z^2} - \sqrt{r_2^2 + z^2}] \quad (5.1)$$

where δg is the calculated terrain effect, G is the gravitational constant ($6.672 \times 10^{-11} \text{ N}\cdot\text{m}^2/\text{kg}^2$), ρ is the density of the terrain material, ϕ is the angle subtending the compartment's arc, r_1 and r_2 are the inner and outer radii of the compartment, and z is the estimated elevation difference between the gravity station and the terrain. The calculated corrections were generally very small, with a typical total terrain correction for a station having been less than 0.05 mGal.

After terrain corrections were applied to the data, the data were reduced to relative Bouguer status. The anomaly was calculated as follows:

$$g_B = g_{obs} - dg_l + dg_f - dg_b + dg_t \quad (5.2)$$

where g_B = relative Bouguer anomaly value;

g_{obs} = drift corrected gravity measurement;

dg_l = latitude correction relative to the base station
($0.8122 \sin \phi$ mGal/km, ϕ =latitude of base station in degrees);

dg_f = free air correction ($0.3086 \cdot h$ mGal/m, where h is the elevation in m);

dg_b = Bouguer correction ($0.0419 \cdot h \cdot \rho$ mGal/m, where h is the elevation in m and ρ is the density in 10^3kg/m^3);

dg_t = terrain correction (in mGal).

A value of 2690 kg/m^3 , given by the method of Parasnis (1972) applied to Profile 89G, was used as the reduction density for both Profile 88G and Profile 89G. The method of Parasnis (op. cit.) uses the measured gravity data in an iterative manner to estimate the optimal reduction density. In this method, the density value which results in the least correlation between the calculated Bouguer Anomaly values and the topography, taken as the reduction density, is determined from the relationship:

$$\rho = \rho_o + \frac{\sum (g_B - g_{Bave}) \cdot (h - h_{ave})}{0.0419 \cdot \sum (h - h_{ave})^2} \quad (5.3)$$

where ρ_o is the initial assumed density (in kg/m^3), g_B is the calculated Bouguer gravity (in mGal) using ρ_o , g_{Bave} is the mean of g_B values, h is elevation (in m), and h_{ave} is the mean elevation.

The method assumes that there are no anomalies below the topography (that is,

the topography is the result of erosion only). However, there are indeed anomalies below the topography here due to the thrust faulting. This may explain why the calculated density is higher than the average value of the Cretaceous rocks (given in section 5.2) that persist to a depth of three kilometres. The inconsistency between the value used in the reduction and the expected value of rocks at shallow depth is not large enough to negatively impact the quality of the reduction.

The reduced gravity data are tabulated in Appendix I, and their profiles are displayed in Figure 5.1 and Figure 5.2. They both show that the Bouguer field is

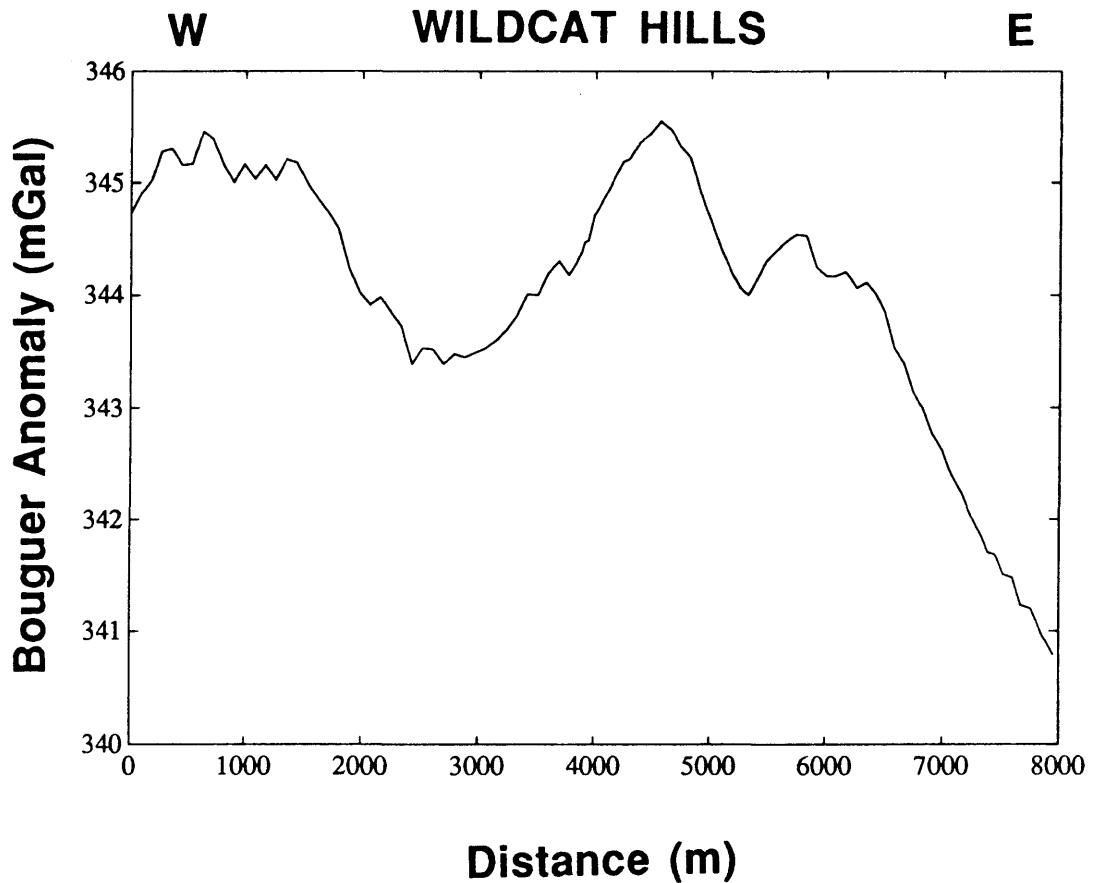


Figure 5.1 Gravity Line 89G Bouguer anomaly.

dominated by a regional west-to-east decrease in gravity values. This west-to-east decrease in the regional field is a localised anomaly that runs contrary to the west-to-east increase of the regional field that is typical for the Alberta Foothills. However, it is consistent with that observed on the GSC regional Bouguer gravity grid.

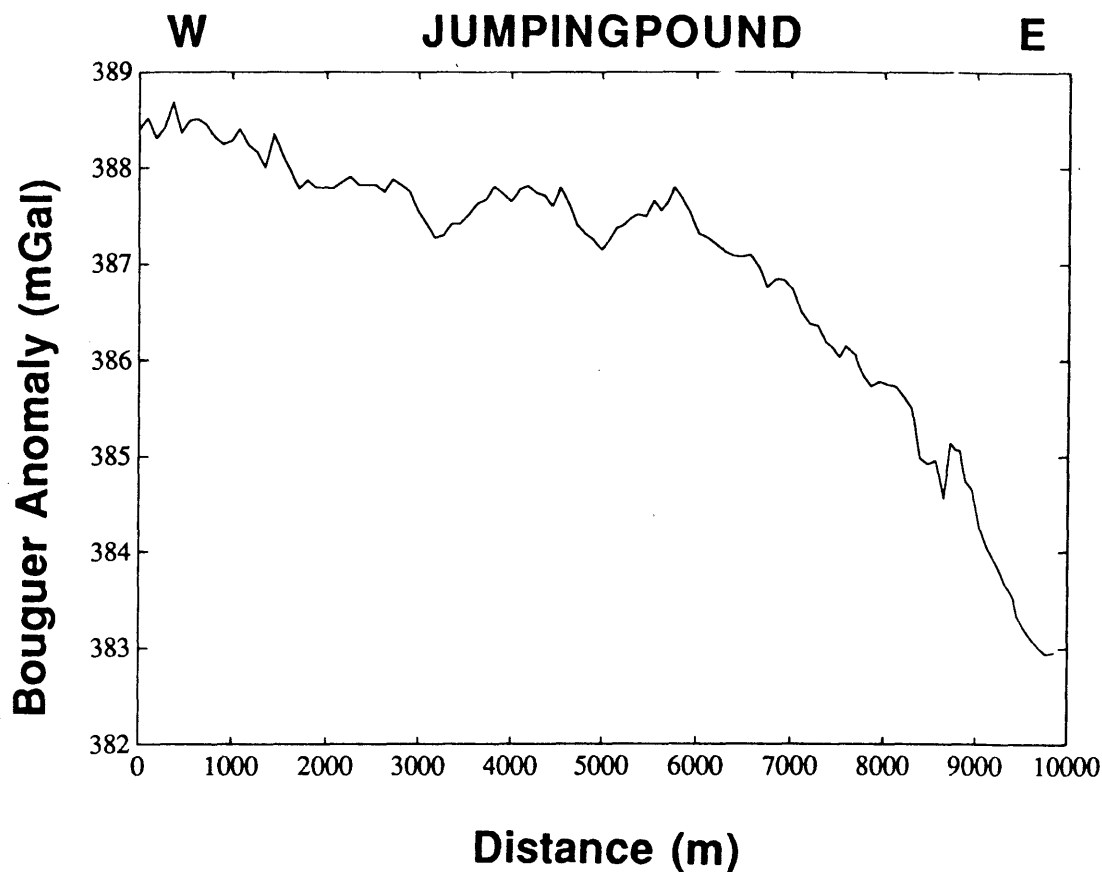


Figure 5.2 Gravity Line 88G Bouguer anomaly.

The Jumpingpound reduced gravity profile was transformed into the Fourier domain, where the number of sources contributing to the anomaly was interpreted and their depths and wavelength bands estimated. Figure 5.3 shows this logarithm-power spectrum, with three distinct slopes interpreted, shown in Figure 5.4. The transformation

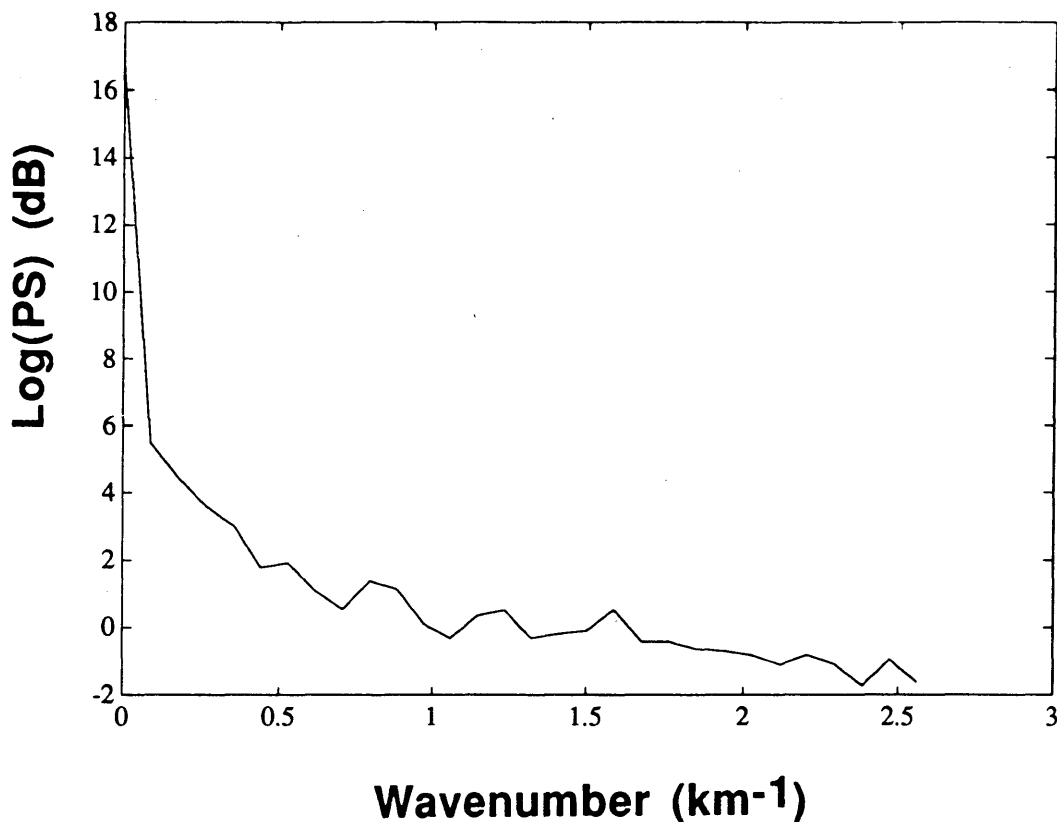


Figure 5.3 Logarithmic-power spectrum of profile 88G.

of the Wildcat Hills profile gave similar results. Treitel et al. (1971) showed that provided that the density contrasts between the anomaly-causing bodies are significant and that each source occurs at a single discrete level, the anomaly for each source will have a distinct slope on a logarithm-power spectrum. Furthermore, Treitel (op. cit.) quantified a relationship between the slope of the anomaly in logarithm-power domain to the top of the anomaly-causing body in the logarithm-power domain as:

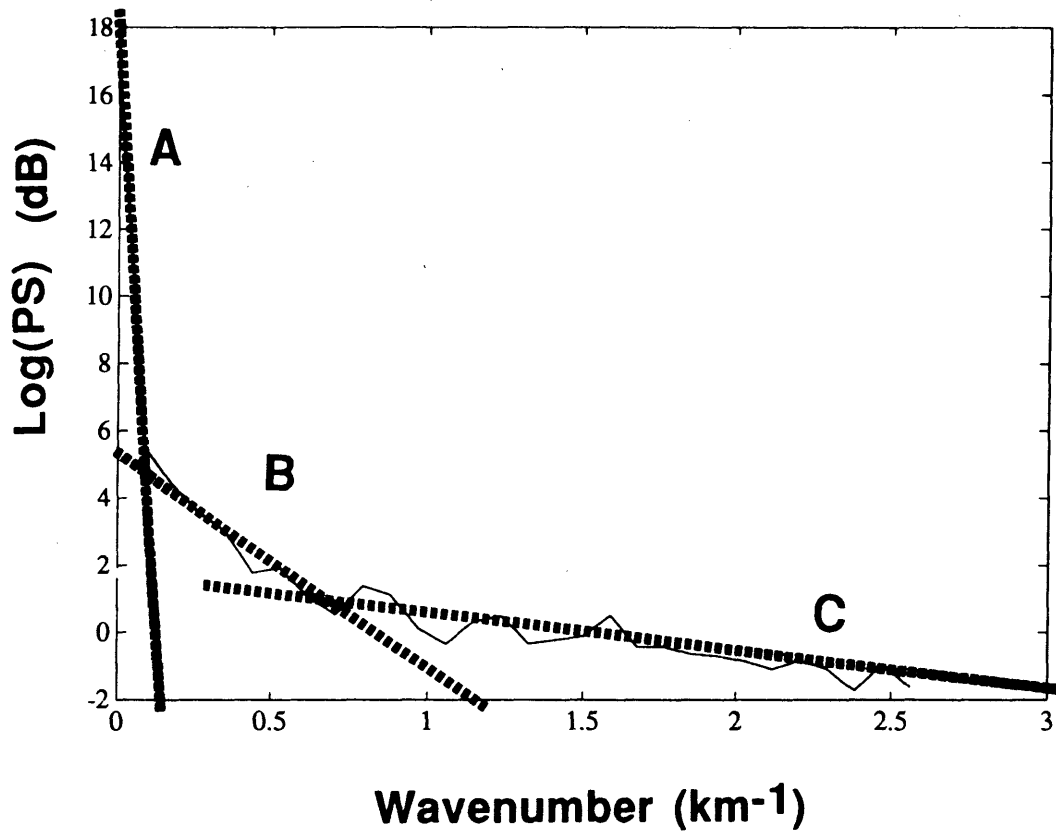


Figure 5.4 Interpretation of Logarithm-Power spectrum: depth estimated from A is 62 km, from B is 3.55 km, and C is 0.59 km.

$$d = \frac{m\tau}{2} \quad (5.4)$$

where d is the depth to the anomaly-causing source, m is the slope measured from the logarithmic-power plot, and τ is the spatial sample interval.

The depths to the top of three anomaly-causing bodies in the study area were calculated to be 0.59 km, 3.55 km, and 62 km respectively, using Equation 5.4. It can be seen that anomalies due to deeper sources tend to be observed at the

lower wavenumbers (higher wavelengths) with higher slopes, while the shallow sources tend to be observed at the higher wavenumbers with lower slopes. The intermediate depth estimate corresponds well with the known top of the carbonate succession of Paleozoic rocks, the anomaly of interest. The wavelength band of the spectrum that this key anomaly occupies is approximately 1.25 to 6.0 km. Anomalies with wavelengths of 1.25 km or less exist, and the shallow depth estimate that is based upon the slope of the spectrum through these lower wavelengths suggests that these are due to the structural deformation of the Cretaceous section. The very deep estimate of the regional field places the source deep into, and possibly below, the crust, with wavelengths of 6 km and more. However, this depth estimate is greater than that expected, as the crust here is likely less than 60 km (Kanasewich, 1966). A possible explanation for this is that a significant component of the gravity field in the high wavelength (low wavenumber) range is likely due to the far field pull of the Rocky Mountains, approximately 30 km to the west of the field area.

5.5 Anomaly Isolation

From the previous section it can be seen that the effects of the shallow and deep sources are substantial. As the anomaly due to the source at the intermediate depth (3 km) is very subtle, it is important to remove as much of these shallow- and deep-sourced anomalies as possible in order to isolate the anomaly from the intermediate depth. This was done in two steps. First, the regional field was estimated and removed, and then

the remaining anomaly was smoothed in order to attenuate the effects of the shallow field.

Several important approaches to anomaly separation include: the subtraction of trends that have been estimated by polynomial fitting; wavelength filtering of data transformed into the Fourier domain; or subtraction of forward models of unwanted anomalies. Subtraction of forward modelled anomalies can be effective, but it requires a detailed knowledge of the source of the anomaly being subtracted. Wavelength filtering, a commonly used method, is simple and can be effective. However, wavelength filtering can result in the loss of important data because the wavelength bands of regional and residual gravity anomalies often overlap. Subtraction of polynomial fit fields is another commonly used technique that can give good results. The subtraction of a polynomial-fit field is much like bandpass filtering, but there is more allowance for overlap in the wavenumber spectrum (Thurston, 1991). The regional field was estimated from and subtracted from the Bouguer Anomalies using a second-order polynomial approximation. In order to minimise the short-wavelength contribution of the near surface, the remaining data were smoothed graphically along inflection point nodes. The resulting residual anomalies are shown, with the theoretical response of the known structure at depth, in the next section.

5.6 Interpretation

The gravity responses of simple numerical models were calculated using a computer program based on the algorithm of Talwani et al. (1959). Models of the

Paleozoic structure, interpreted from seismic and well-log and seismic data, were constructed. A density contrast of 240 kg/m^3 was used. As the effects of the shallow and deep sources were considered to have been minimised, they were not modelled.

The final models, their theoretical gravity anomalies, and the corresponding residual anomalies are displayed in Figures 5.5 and 5.6. The theoretical anomalies have

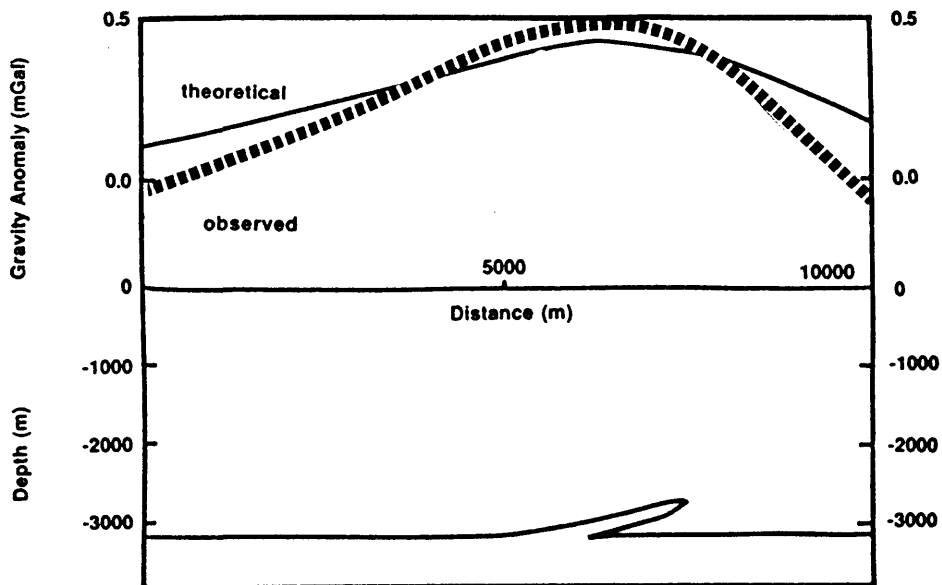


Figure 5.5 Observed and theoretical gravity responses corresponding to Line 88G.

a maximum that is between 0.3 and 0.4 mGal. They have a slightly asymmetrical appearance, with the east side of the anomaly having a steeper slope than the west side. The general shape of the observed anomalies mimics that of the theoretical anomalies from the known structure, and their respective maxima are close. However, the flanks

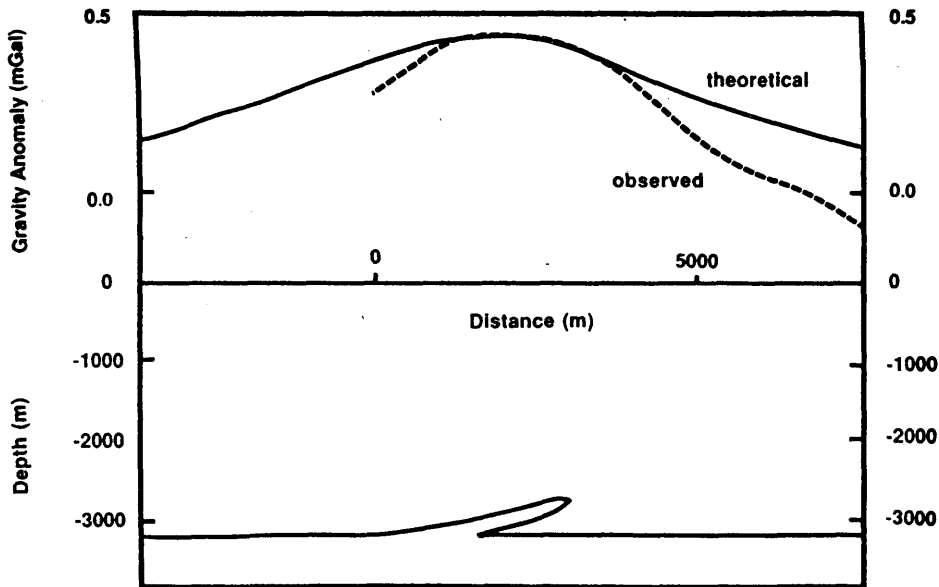


Figure 5.6 Observed and theoretical responses corresponding to Line 89G.

of the theoretical and observed anomalies do not match exactly. This likely indicates a suboptimal separation of the anomaly due to the Paleozoic structure from the shallow- and deep-sourced anomalies, with too much of the low wavenumber spectrum having been filtered away with the removal of the polynomial-fit field.

The Turner Valley structure, which is located south of the study area, is a structure that has a considerable volume of carbonate rocks involved in the deformation. Figure 5.7 is a simplified model of the structure based upon the interpretation of MacKay (1991). This model, in which a density contrast of 240 kg/m^3 was used, has a theoretical anomaly that is nearly 2 mGal in magnitude. Such an anomaly should be readily discernable in field observations.

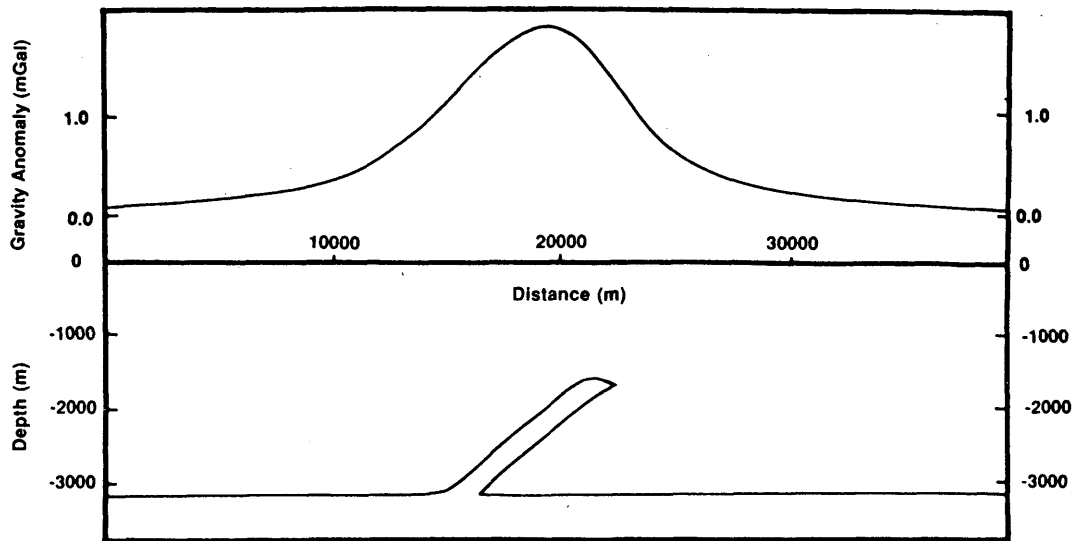


Figure 5.7 Theoretical gravity response of the Turner Valley structure.

5.7 Error Analysis

Error in the reduced gravity data is affected primarily by observational errors, but also errors in the positioning survey (both errors in the elevations and latitudes), and in the estimation of the terrain. The aggregate error can be estimated using the following relation of McCollum (1952):

$$pe = 0.3452 \cdot \frac{\sum_{j=2}^{n-1} |g_b(j+1) - 2g_b(j) + g_b(j-1)|}{n-2} \quad (5.5)$$

where pe is the probable error, g_b is the Bouguer Anomaly value, and n is the number of measurements. The probable error of the Bouguer Anomalies of Lines 88g and 89G were

calculated to be 0.045 mGal, and 0.056 mGal respectively.

5.8 Discussion

From the data presented in this chapter it is clear that it is possible to detect the structural involvement of carbonate rocks on Foothills structures using the gravity data. However, special effort is required to isolate the gravity field from the intermediate depths. Furthermore, since the anomaly of a carbonate-involved structure is small, the data are not capable of uniquely resolving the subtle characteristics of the structure. It is therefore suggested that while investigating such structures in the Foothills, gravity data are useful to detect carbonate duplication, but not for determining structural details. Where it is thought the crystalline basement rock is uniform, the gravity method is probably best suited as a fill-in tool between seismic lines, or where seismic data are sparse.

Chapter 6 Structural Interpretation

6.1 Introduction

The locations of a series of balanced cross-sections that were constructed through the study area are shown in Figure 6.1. These cross-sections, which were constructed using the seismic interpretations, well data, and surface geological data, illustrate the geometry of the structure in the Jumpingpound-Wildcat Hills area. The seismic interpretations were projected along regional strike into the cross-sections to control the locations of the key structural features such as hangingwall and footwall cutoffs, and the well data were used to control the actual depths and thickness of the stratigraphic units. The cross-sections were palinspastically restored into their respective undeformed states, showing that they are line balanced and are viable restorable sections. They were reconstructed by measuring line length of each marker and sequentially restoring that line length of the marker into its undeformed state. It is assumed that the strain was within the plane of the cross-sections.

6.2 Structure

Figures 6.2 - 6.4 show three cross-sections through the study area in their deformed and palinspastically reconstructed states. Figure 6.5 shows a cross-section and reconstruction through the Wildcat Hills (from Kubli et al., 1992) that is based upon the

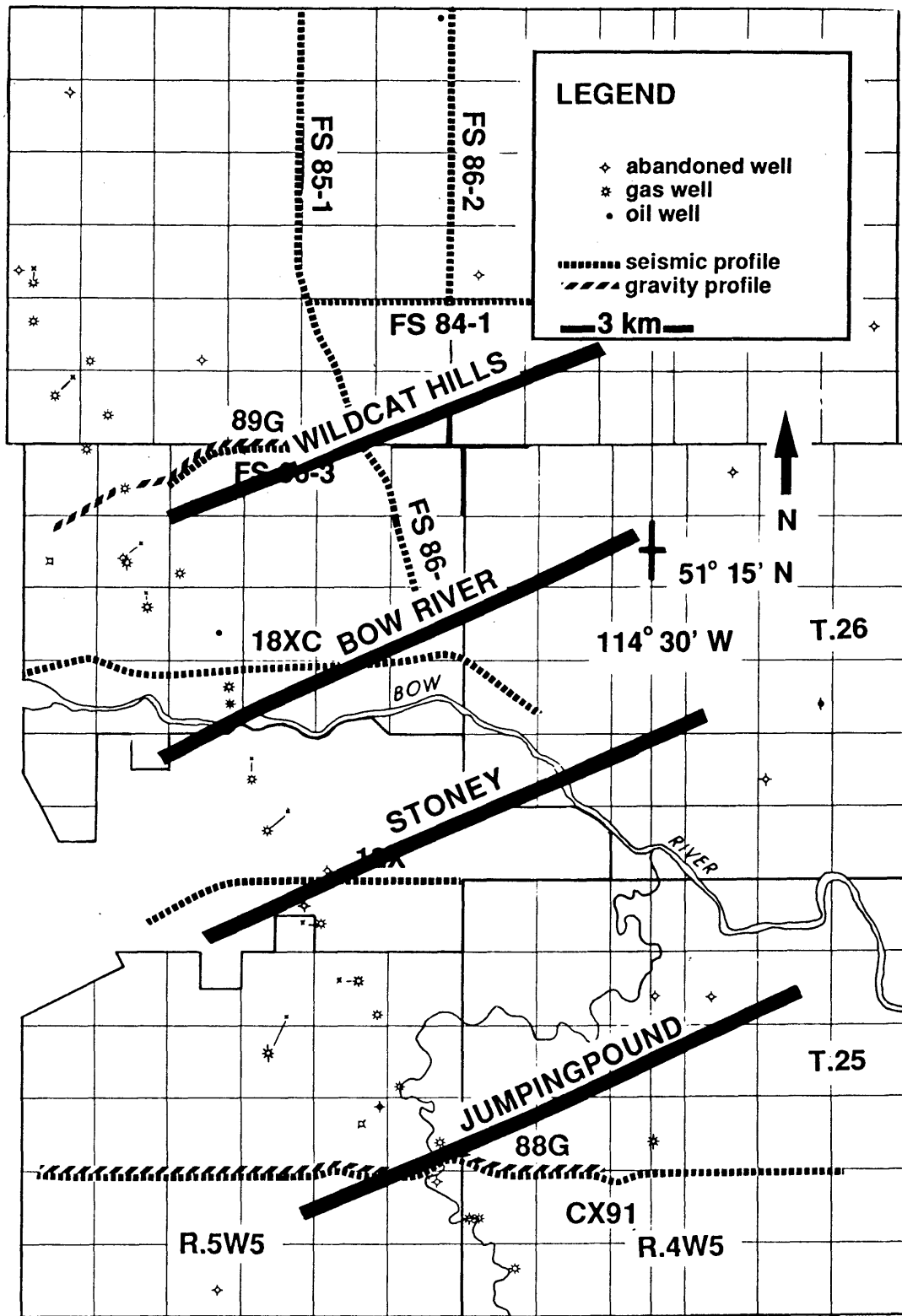


Figure 6.1 Locations of cross sections constructed through the study area.

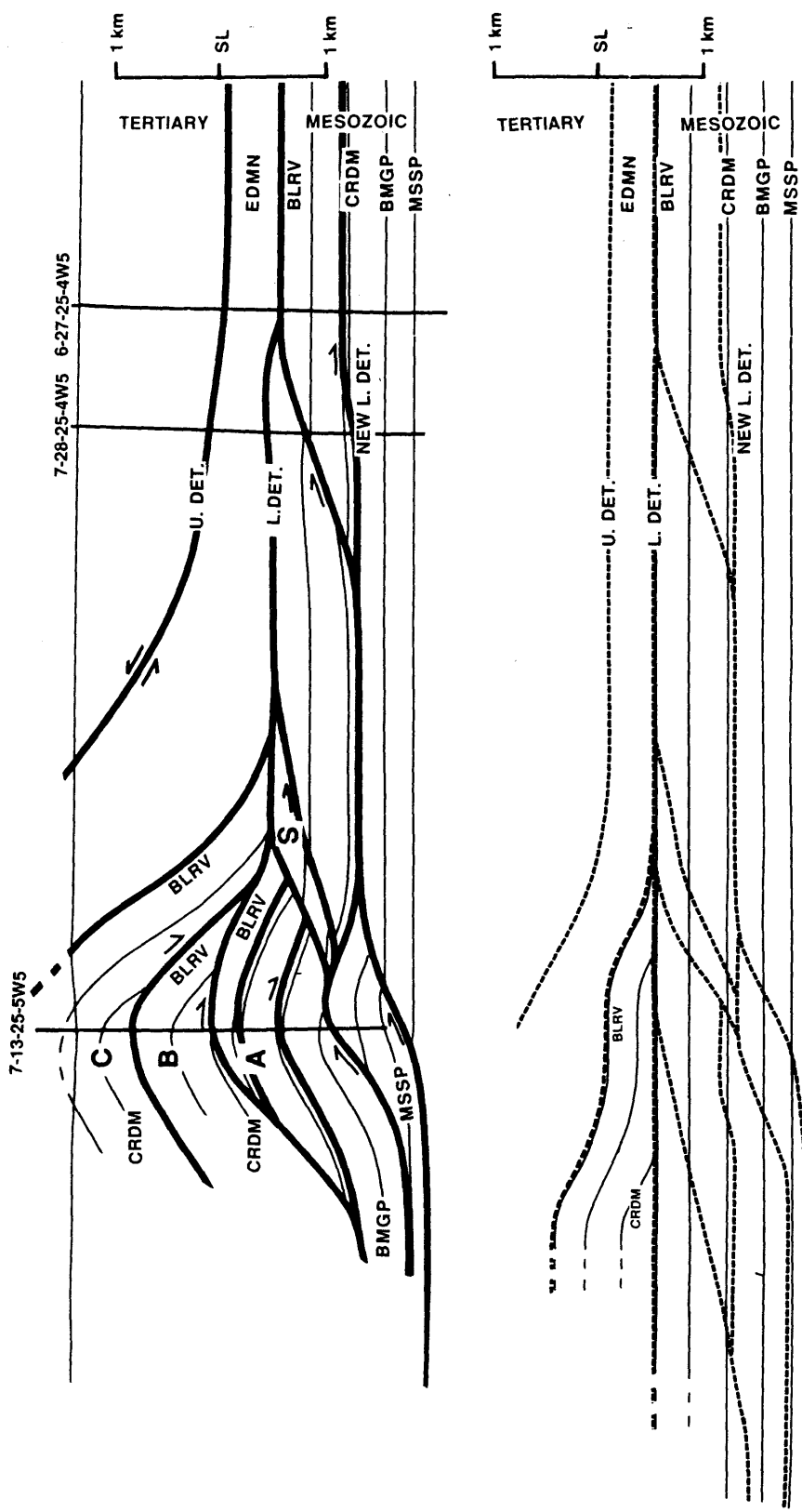


Figure 6.2 Vertical cross section and reconstruction through Jumpingpound profile.

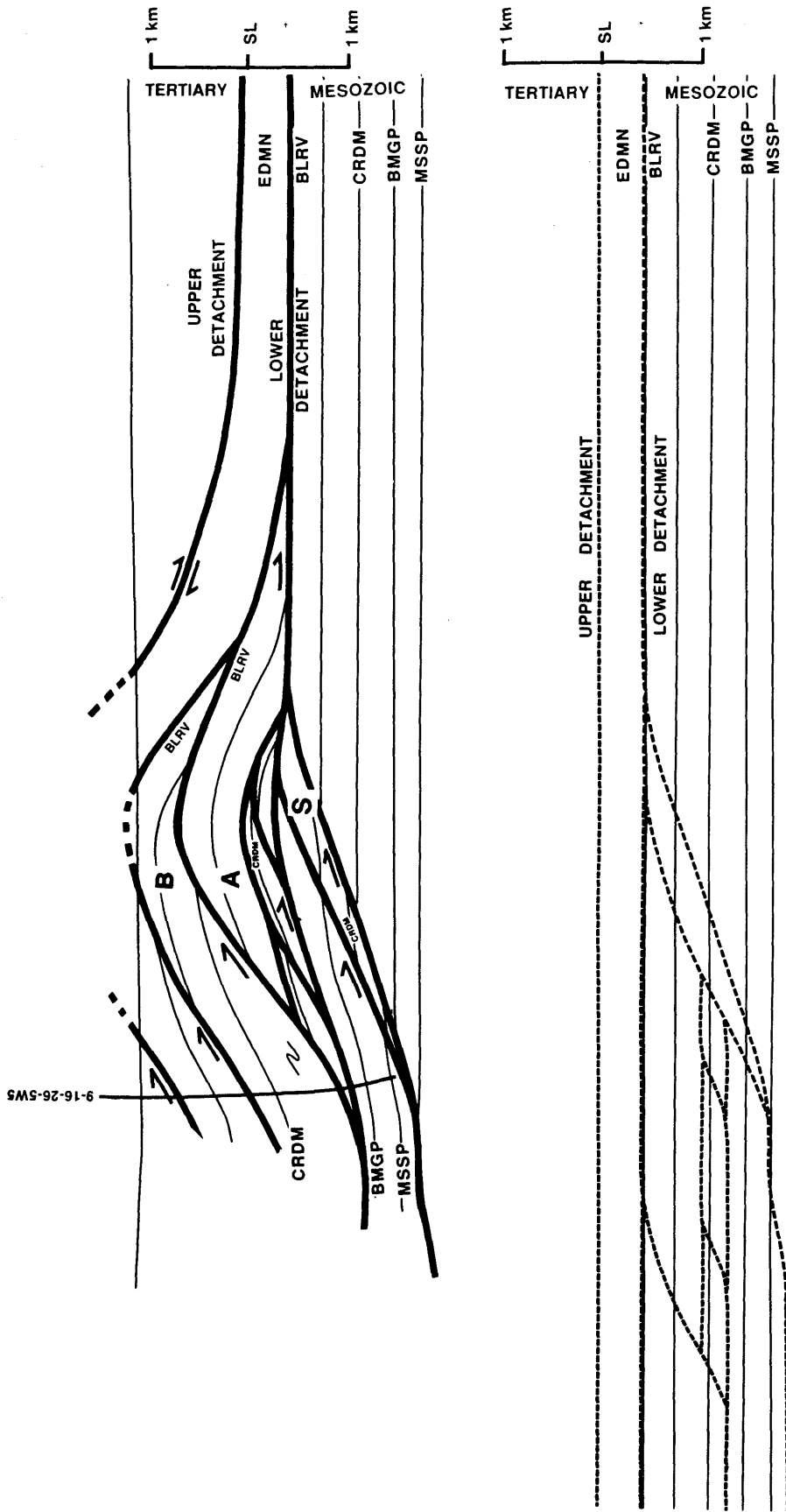


Figure 6.4 Vertical cross section and reconstruction through Bow River Profile.

STRUCTURAL CROSS-SECTION WILDCAT HILLS

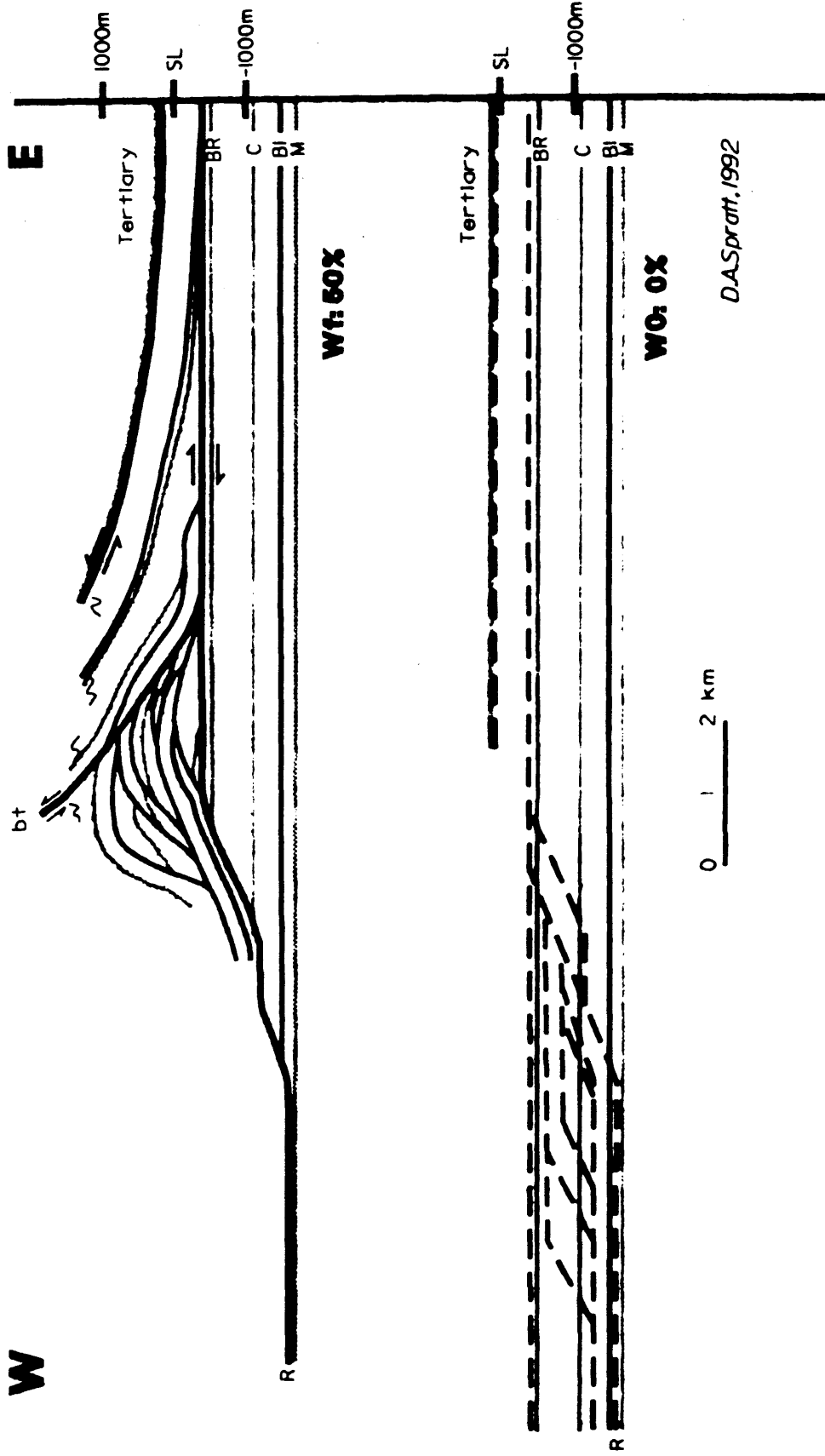


Figure 6.5 Vertical cross-section and reconstruction through the Wildcat Hills. After Kubli et al., 1992.

seismic interpretation shown in Figure 4.8. The profiles show the structure to be an antiformal stack of duplexes involving Cretaceous rocks that trends NW-SE and that has been forced into foreland strata between two bedding-parallel detachments.

Carbonate rocks of Mississippian age are carried in the hanging wall of the lower detachment to a maximum observed displacement of approximately 1.5 km, and rise to 500 m above its regional elevation, as seen in Figure 6.3. This shortening is significantly less than that of the Mesozoic section, which implies considerable shortening must be taken up by the Paleozoic rocks west of the study area, likely in the Jumpingpound West and Moose Mountain culminations. The lower detachment rises from a flat near the middle of the Banff Formation and flattens out beneath the Edmonton Group, near the top of the Belly River Formation. The upper detachment rides within the Edmonton Group, and the two detachments are not observed to merge at a simple branch point near the triangle zone.

The detachment below the Edmonton Group is the roof thrust of the duplexes of Cretaceous rocks that have been stacked to build the main culmination. The floor thrust is less persistent, with the Fernie Formation generally containing the most important detachment, followed by the Wapiabi Formation.

The duplexes are stacked and folded at Jumpingpound in the south and provide a narrower culmination than in Wildcat Hills to the north. At Jumpingpound, there are fewer thrust blocks, but they are larger and have experienced greater displacement on each thrust fault, creating a broader structure. The total shortening for each cross-section averages between 40 and 50 percent at the level of the Cardium Formation, along faults

which generally dip less than 30°.

The primary elements of the structure can be correlated from cross-section to cross-section. The basal fault block, labelled with an "A", shows increasing displacement toward the north and grows in length. In each cross-section, the details of the minor faulting within this fault block varies, with important detachments riding in the Wapiabi and Blackstone Formations. The fault block labelled with a "B" has displacement with respect to the underlying "A" block that appears to be relatively constant from cross-section to cross-section, except on the Wildcat Hills cross-section, where it appears to have gained displacement. Interpreted on the Stoney Profile (Figure 6.3) is a thrust fault that splits the "B" block. This fault was not interpreted on the corresponding seismic section (Figure 4.5), and was interpreted in order to satisfy mass balance constraints. The fault block labelled with a "C" is an important part of the main culmination on the Jumpingpound cross-section, but it progressively loses displacement northward, presumably as displacement is picked up on the lower thrust faults. In the footwall of the "A" thrust block is a thin sliver of Cretaceous rocks, labelled with an "S". This sliver becomes increasingly deformed northward, until it is only recognizable as contorted rock in the footwall of the overlying duplex (Figure 6.5).

East of the main culmination and below the Upper detachment, there is a zone of intensely deformed rocks. These are interpreted to be rocks of the Edmonton Group that have been shortened by folding and faulting as they were pushed ahead of the main culmination and thrust below the upper detachment.

On the Jumpingpound cross-section (Figure 6.2), a bedding-parallel fault in the

Blackstone Formation is seen to extend the structural shortening well ahead of the main culmination. This thrust appears to have lost all displacement at Wildcat Hills. However, under-thrusting below the Cardium, seen on the Soney Profile (Figure 6.3) just to the north of Jumpingpound, suggests that displacement persists along this fault at that location.

Duplexing is observed to occur at several levels and scales. The antiformal stack is built from large fault blocks that include rocks from the Blairmore Formation to the Belly River Formation. Smaller-scale structures are observed at the seismic scale (where generally only features larger than 100 m can be resolved), primarily in the Cardium level where small displacement faults (less than 500 metres) are common. This manifests the lithology contrast between the encasing shales of the Blackstone and Wapiabi formations and the more competent sandstones of the Cardium Formation. These encasing shales tend to accommodate shortening through folding whereas the Cardium rocks are more rigid and therefore more prone to faulting. As a result, the Wapiabi and Blackstone formations act as effective roof and floor detachments which accommodate Cardium level duplexing.

Figure 6.6 shows a simple map that illustrates the structural elements as interpreted on the seismic data and cross-sections. It is of interest to compare this map with the geological map that was made by field mapping, which is shown in Figure 2.2. It can be seen that the main characteristics of the two maps are consistent, i.e. the strike of the structure is the same, and the location of the main culmination is the same. However, there is a clear difference in the scale of the two maps, with the map based upon mapping

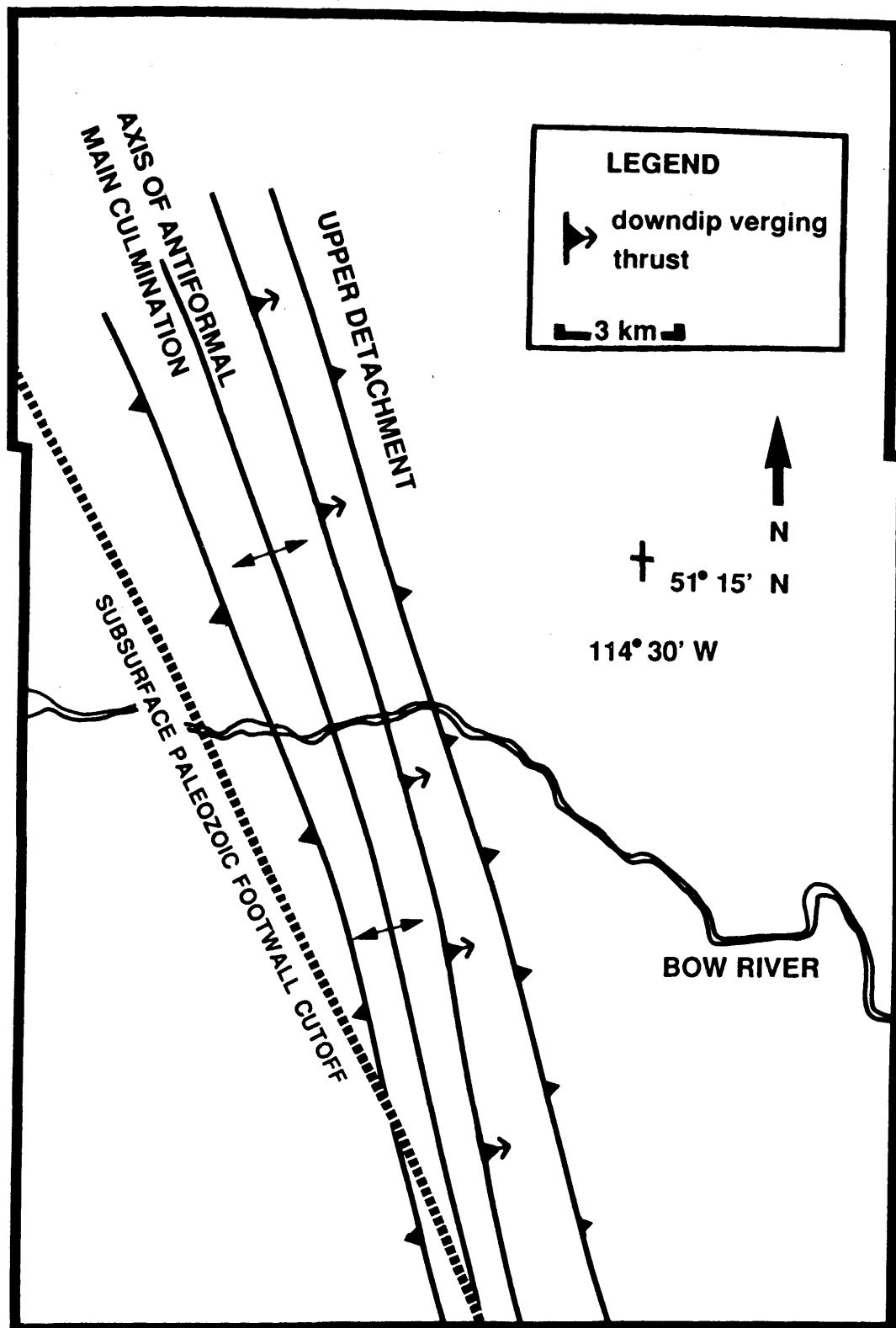


Figure 6.6 Structural elements map constructed from seismic data and cross sections.

of the seismic data being more coarse than the map based upon the surface mapping, with none of the minor features interpreted on the geological map, which may indeed be present. The accuracy in the locations of certain features, however, such as the surface location of the upper detachment, are more accurate on the seismic-based map, due to the subsurface control provided by the seismic data in areas that lack good surface exposure.

6.3 Discussion

The smoothness of the upper detachment seen here is a peculiarity of the triangle zone which is observed in other areas (MacKay, 1991; Teal, 1983). It seems puzzling that it does not simply conform to the shape of the complex structure in its footwall. It is suggested that this smoothness indicates that the upper detachment is an active roof thrust, that is, it is acting as a boundary constraint, and not a passive-roof as suggested by Jones (1982) in his model or by other passive roof duplex models (Banks and Warburton, 1986). This seems to indicate that the Charlesworth model (Charlesworth and Gagnon, 1985) is preferred for the structure in the study area, although evidence of a backthrust origin of the upper detachment is not seen.

The long distance that the strain has extended into the foreland is interesting for two reasons. For the exploration of structural hydrocarbon traps, the main culmination cannot be considered the limit of deformation, as subtle duplex traps can exist along the bedding-parallel detachments that propagate into the foreland (also seen by Skuce et al., 1992). An example is shown in the Jumpingpound cross-section (Figure 6.2), and another

was documented by MacKay (1991, Figure 6).

This eastward extent of strain is also important, as it suggests that a pin line, a point at which strain ceases, cannot be placed directly to the foreland of the antiformal stack. However, for a triangle zone to be abandoned as a new back thrust develops in the foreland, as in the Charlesworth et al. (1985) model, displacement must extend a considerable distance ahead of the main culmination. This is consistent with what is seen in the study area.

The large fault block seen ahead of the antiformal stack at Jumpingpound appears to be in a stage incipient to the development of a new antiformal stack. This suggests that the current detachment was about to be abandoned, but does not necessarily mean that the entire triangle zone was about to be abandoned, which would require a new backthrust to develop in the foreland. However, with east dips well developed on the east side of the main culmination, such an abandonment could create a syncline, with Cretaceous rocks in its core. Such synclines are seen in the Foothills, e.g. the Jumpingpound

syncline west of the study area, and their development may be as shown in the schematic diagram in Figure 6.7. This presents an alternative to Jones' (1982) model for the development of synclines in the fold belt, where the synclines are the remnants of passively folded upper detachments.

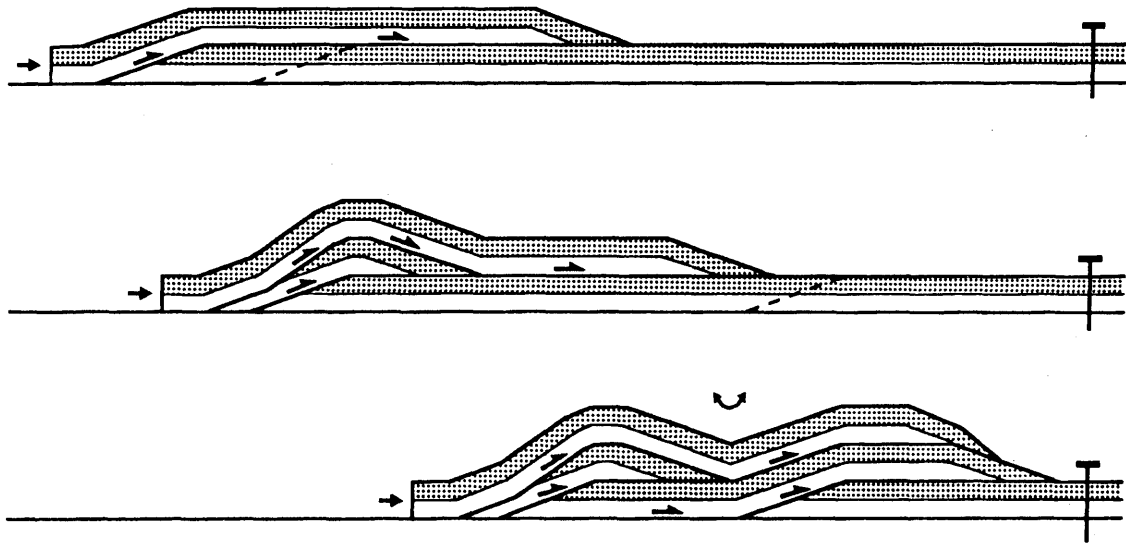


Figure 6.7 Schematic diagram illustrating possible development of surface synclines in the Foothills belt.

Chapter 7 Conclusions

Seismic, well, and surface data have been acquired, processed, and interpreted to reveal the triangle zone in the Jumpingpound-Wildcat Hills area to be a NW-SE trending antiformal stack of duplexes involving Cretaceous rocks that have been forced eastward into foreland deposits between two detachments. The interpretations present the geometry of the structure in greater detail than has been previously published. A new observation of this structure is that there is no simple branch point directly in front of the main culmination, and that tectonic shortening likely propagates a considerable distance in the foreland. This challenges the thesis that a pin line can be placed directly in front of the triangle zone. It has been proposed that the well-constrained observation that the upper detachment has remained smooth, despite the complex structure it sits upon, contradicts the notion that the upper detachment is a passive surface, and likely is active, as suggested by Charlesworth et al. (1987). Finally, based upon the observation of a long thrust sheet in the area, a sequence for the development of synclines that is based upon the development of long thrust sheets has been proposed.

It has been shown that the steep dips of the triangle zone are difficult to record, and that it is important to record data using a wide aperture, a small group interval and an adequate record time in order to record those steep dips. In the processing of the seismic data in this work, reduction of random noise using a beam steering technique early in the processing of the data resulted in good-quality seismic images because of the improved statics solutions and stacking velocities that were made possible.

It is apparent from this work that for this generalised geologic setting, long wavelength, subtle gravity anomalies measured at the surface can be due to carbonate duplication. An anomaly of less than 0.5 mGal was interpreted from the gravity profiles acquired in the study area, after considerable effort to remove the relatively substantial effects of the regional and near-surface sources. It is apparent that at the depth in question, details of the structure are not uniquely resolved by gravity data. Rather, they serve to confirm carbonate duplication within the structure. This suggests that the method is well suited to provide a simple method of correlating structural features between seismic profiles. Furthermore, as the anomalies occupy the low-wavenumber (high-wavelength) end of the spectrum, large station intervals (e.g., 250 m) should be adequate in the acquisition of gravity data for the purpose of delineating carbonate-involved structures. Furthermore, long profile lengths are desirable in order to capture the long wavelength components of the anomaly due to a carbonate-involved structure. For a geological cross-section such as that found in the Jumpingpound-Wildcat Hills area, a profile length of 15 km or more is desirable.

References

- Bally, A.W., Gordy, P.L., and Stewart, G.A., 1966, Structure, seismic data and orogenic evolution of the Southern Canadian Rocky Mountains, *Bull. Can. Petrol. Geol.*: **14**, 337-381.
- Banks, C.J., and Warburton, J., 1986, "Passive roof" duplex geometry in the frontal structures in the Kirthar and Sulaiman mountain belts, Pakistan, *J. Struct. Geol.*: **8**, 229-237.
- Charlesworth H.A.K., and Gagnon L.G., 1985, Intercutaneous wedges, the triangle zone and structural thickening of the Mynheer coal seam at Coal Valley in the Rocky Mountain Foothills of central Alberta: *Bull. Can. Petrol. Geol.*: **33**, 22-30.
- Charlesworth H.A.K., Johnston S.T. and Gagnon L.G., 1987, Evolution of the triangle zone in the Rocky Mountain Foothills near Coalspur, central Alberta: *Can. J. Earth Sci.*: **24**, 1668-1678.
- Cheadle, S., 1988, Applications of physical modeling and localized slant stacking to a seismic study of subsea permafrost: PhD thesis, University of Calgary, Calgary, Alberta, Canada, 237 p.
- Dahlstrom, C.D.A, 1969, Balanced cross-sections: *Can. J. Earth Sci.*: **6**, 743-757.
- Dahlstrom, C.D.A, 1970, Structural geology in the eastern margin of the Canadian Rocky Mountains: *Bull. Can. Petrol. Geol.*: **18**, 332-406.
- Fox F.G., 1959, Structure and accumulation of hydrocarbons in southern Foothills, Alberta, Canada: *Bull. Amer. Assoc. Petrol. Geol.*, **43**, 992-1025.
- Gordy, P.L., Frey, F.R., and Ollerenshaw, N.C., 1975, Road log, Calgary - Turner Valley - Jumping Pound - Seebe: in Evers, H.J., and Thorpe, J.E., eds.: *Structural geology of the Foothills between Savanna Creek and Panther River, S.W. Alberta, Canada; Guidebook*, *Can. Soc. Petrol. Geol. / Can. Soc. Expl. Geoph.*, Calgary, 35-61.
- Gordy, P.L., Frey, F.R., and Norris, D.K., 1977, Geological guide for the Canadian Society of Petroleum Geologists and the 1977 Waterton-Galcier Park Field Conference: *Can. Soc. Petrol. Geol.*, Calgary: 93 p.
- Hammer, S., 1939, Terrain correction for gravity meter stations: *Geophysics*, **4**, 184-194.

Harrison, M.P., 1990, F-X linear prediction filtering of seismic images: the CREWES Project, Research report, **2**, University of Calgary, Calgary, Alberta, 147-165.

Hiebert S.N. and Spratt, D.A., 1991, Study of the Triangle Zone and Foothills structures near Pincher Creek, Alberta: in Current Research, Part B, Geol. Surv. Canada, Paper 91-1B, 41-46.

Hume, G.S., 1927, Turner Valley oil area, Alberta: Geol. Surv. Canada, Summary Report, 1926, pt. B, 1-14.

Jones, P.B., 1982, Oil and gas beneath east-dipping underthrust faults in the Alberta Foothills, Canada: in R.B. Powers, ed., Geologic studies of the Cordilleran thrust belt: Denver, Rocky Mountain Assoc. Geol., **1**, 61-74.

Jones, P.B., 1989, Structural geology of the Alberta Foothills Front in the Calgary region, A Field Guide.

Kanasewich, E.R., 1966, Deep crustal structure under the plains and Rocky Mountains: Can. J. Earth Sci.: **3**, 937-945.

Kubli, T.E. and Leibel, J.L., 1992, Geology of the Foothills and Front Ranges west of Calgary: AAPG Student Chapter Field Trip 24, 93 p.

Lawton, D.C., 1989, Computation of refraction statics using first-break traveltimes differences: Geophysics, **54**, 1289-1296.

Lawton, D.C. and Spratt D.A., 1991, Geophysical and geological aspects of the triangle zone, Rocky Mountains Foothills: C.S.E.G. Continuing Education Field Trip, 33 p.

Link, T.A., 1949, Interpretations of Foothills structures, Alberta, Canada: Bull. Amer. Assoc. Petrol. Geol., **33**, 1475-1501.

Lynn, H.B., and Deregowski, S., 1981, Dip limitations on migrated sections as a function of line length and recording time: Geophysics, **46**, 1392-1397.

MacKay, P.A., 1991, A geometric, kinematic and dynamic analysis of the structural geology at Turner Valley, Alberta: PhD thesis, University of Calgary, Calgary, Alberta, Canada, 138 p.

Maxant, J., 1975, Distribution and regional variation of density in the Western Canada Basin from density logs, Geophysics, **45**, 1061-1076.

McCollum, E.V., 1952, Quality of geophysical measurements: Geophysics, **17**, 56-59.

McCrossan, R.G., 1964, Geologic History of Western Canada, Alberta Society of Petroleum Geology.

Monger, J.W.H., Price R.A., and Tempelman-Kluit D.J., 1982, Tectonic accretion and the origin of the two major metamorphic and plutonic belts in the Canadian Cordillera: *Geology*, **10**, 70-75.

Morley, C.K., 1986, A classification of thrust fronts: *Bull. Amer. Assoc. Petrol. Geol.*, **70**, 12-25.

Ollerenshaw, N.C., 1976, Jumpingpound Creek (East Half), Alberta, *Geology: Geol. Surv. Canada*, Map 1419A.

Parasnis, D.S., 1972, Principles of applied geophysics: Chapman and Hall, London, 214 p.

Paukert, G.W., 1982, Geophysical study of Precambrian basement fault structure and related Cretaceous stratigraphic variation in Southern Alberta: MSc. thesis, University of Calgary, Calgary, Alberta, Canada, 128 p.

Sanderson, D.A., and Spratt D.A., 1992, Triangle zone and displacement transfer structures in the Eastern Front Ranges, Southern Canadian Rocky Mountains: *Bull. Amer. Assoc. Petrol. Geol.*, **76**, 828-839.

Skuce, A.G., Goody, N.P., and Maloney, J., 1992, Passive-roof duplexes under the Rocky Mountain Foreland Basin, Alberta: *Bull. Amer. Assoc. Petrol. Geol.*, **76**, 67-80.

Stolt, R.H., 1978, Migration by Fourier transform: *Geophysics*, **43**, 23-48.

Stott, D.F., 1963, The Cretaceous Alberta Group and equivalent rocks, Rocky Mountain Foothills, Alberta: *Geol. Surv. Canada Memoir*, **317**, 306 pp.

Syberg, F.J.R., 1972, A fourier method for the regional-residual problem of potential fields: *Geophysical Prospecting*, **20**, 47-45.

Talwani, M., Worzel, J.L., and Landisman, M., 1959, Rapid gravity computations for two-dimensional bodies with application to the Mendocino submarine fracture zones: *J. Geophys. Res.*, **64**, 49-59.

Teal, P.R., 1983, The triangle zone Cabin Creek, Alberta, *in* A.W. Bally, ed., Seismic expressions of structural styles: *AAPG Studies in Geology* **15**, **3**, 3.4.1-48-3.4.1-53.

Thurston, 1991, Formulation of digital filters using polynomial approximation methods

with applications to Bouguer gravity data from northern Alberta: MSc thesis, University of Calgary, Calgary, Alberta, Canada, 130 p.

Treitel, S., Clement, W.G., and Kaul, R.K., 1971, The spectral determination of depths to buried magnetic basement rocks: *Geophys. J. R. Astr. Soc.*, **24**, 415-428.

Vann, I.R., Graham, R.H., and Hayward, A.B., 1986, The structure of mountain fronts: *J. Struct. Geol.*, **8**, 215-227.

Workum, R.H., 1978, Stratigraphy of the Central Foothills, in Jones, P.B., and Workum, R.H., eds., *Geological guide to the central Foothills and eastern Rockies, Field Trip Guide Book*, CSPG, 61 p.

Yilmaz, O., 1987, Seismic data processing, Series: Investigations in geophysics, Volume 2, Society of Exploration Geophysicists, Tulsa, Oklahoma, 526 pp.

Appendix I - Gravity Data

Line 88G (Jumpingpound Profile)

Station Number	Distance (x) (metres)	Elevation (metres)	Bouguer Anomaly (mGal)
100	0.000	1316.384	388.39
103	90.000	1316.325	388.52
106	180.000	1316.153	388.31
109	270.000	1314.269	388.41
112	359.850	1310.434	388.68
115	449.660	1305.194	388.36
118	539.370	1298.920	388.49
121	628.810	1291.174	388.51
124	718.740	1285.164	388.45
127	808.400	1279.541	388.32
130	898.310	1277.571	388.24
133	988.300	1277.090	388.28
136	1078.115	1279.370	388.40
139	1168.080	1280.177	388.23
142	1258.100	1281.404	388.16
145	1347.600	1281.352	388.00
148	1437.600	1278.172	388.35
151	1527.400	1278.140	388.14
154	1617.000	1283.345	387.96
157	1706.900	1284.486	387.78
160	1796.900	1286.075	387.87
163	1886.700	1286.003	387.79
166	1976.600	1284.744	387.79
169	2068.300	1285.883	387.78
172	2160.000	1285.586	387.85
175	2252.000	1284.247	387.91
178	2344.000	1281.741	387.82
181	2435.400	1279.448	387.82
184	2527.000	1277.700	387.82
187	2619.000	1273.493	387.74
190	2710.000	1266.744	387.88
193	2801.000	1257.576	387.82
196	2893.000	1251.508	387.75
199	2984.000	1242.849	387.55
202	3077.000	1248.182	387.42
205	3168.000	1248.477	387.27
208	3260.000	1248.488	387.29

211	3352.000	1248.749	387.42
214	3444.000	1248.502	387.42
217	3536.000	1248.716	387.51
220	3627.000	1248.177	387.63
223	3720.000	1248.105	387.67
226	3811.000	1250.209	387.80
229	3900.000	1254.230	387.73
232	3995.000	1255.331	387.65
235	4090.000	1254.310	387.77
238	4178.000	1251.412	387.81
241	4269.000	1248.317	387.74
244	4362.000	1244.646	387.71
247	4452.000	1242.377	387.60
250	4542.000	1240.736	387.79
253	4632.000	1239.755	387.63
256	4722.000	1240.806	387.41
259	4812.000	1241.889	387.31
262	4902.000	1242.822	387.25
265	4992.000	1243.518	387.14
268	5080.000	1241.304	387.25
271	5154.000	1238.624	387.37
274	5210.000	1237.144	387.39
277	5301.000	1238.254	387.47
280	5377.000	1243.511	387.51
283	5465.000	1250.102	387.49
286	5548.371	1256.288	387.66
289	5625.000	1259.549	387.55
292	5694.000	1259.057	387.64
295	5766.000	1254.755	387.79
298	5844.000	1248.333	387.68
301	5934.000	1242.358	387.52
304	6024.000	1239.338	387.31
307	6114.000	1239.181	387.27
310	6204.000	1241.517	387.21
313	6294.000	1245.880	387.12
316	6384.000	1247.419	387.08
319	6474.000	1245.234	387.07
322	6564.000	1241.351	387.09
325	6654.000	1237.841	386.97
328	6745.000	1236.000	386.76
331	6835.000	1237.843	386.84
334	6925.000	1239.811	386.83
337	7015.000	1239.688	386.74
340	7105.000	1236.887	386.50

343	7195.000	1233.096	386.38
346	7284.000	1227.960	386.36
349	7368.000	1220.390	386.19
352	7443.000	1213.020	386.13
355	7510.000	1207.788	386.03
358	7576.000	1205.285	386.15
361	7686.000	1203.270	386.06
364	7710.000	1200.403	385.96
367	7774.000	1211.169	385.84
370	7855.000	1219.765	385.73
373	7944.000	1228.054	385.78
376	8034.000	1235.283	385.75
379	8124.000	1241.571	385.73
382	8214.000	1247.918	385.63
385	8302.000	1254.172	385.50
388	8390.000	1265.176	384.99
391	8477.000	1271.889	384.92
394	8565.000	1273.893	384.96
397	8652.000	1270.823	384.56
400	8720.000	1267.608	385.14
403	8775.000	1260.470	385.07
406	8823.000	1252.859	385.06
409	8878.000	1245.046	384.75
412	8953.000	1238.760	384.65
415	9041.000	1231.550	384.24
418	9131.000	1223.262	384.02
421	9221.000	1218.900	383.87
424	9311.000	1216.240	383.67
427	9401.000	1214.797	383.52
430	9443.000	1215.110	383.33
433	9582.000	1217.824	383.12
436	9671.000	1217.609	383.02
439	9762.000	1213.096	382.94
442	9852.000	1209.576	382.96
445	9942.000	1210.172	382.89
448	10032.000	1211.607	383.11

Line 89G (Wildcat Hills Profile)

Station Number	Distance (x) (metres)	Elevation (metres)	Bouguer Anomaly (mGal)
1	0.000	1239.233	340.79

2	90.093	1235.812	340.98
3	179.845	1233.986	341.20
4	270.209	1232.124	341.23
5	359.565	1229.052	341.48
6	449.406	1223.388	341.51
7	540.209	1220.721	341.69
8	629.888	1220.720	341.71
9	719.847	1222.198	341.89
10	809.668	1225.227	342.03
11	898.996	1225.680	342.25
12	989.328	1232.316	342.40
13	1079.455	1236.207	342.63
14	1169.869	1239.982	342.77
15	1259.542	1243.123	343.00
16	1349.875	1246.120	343.14
17	1439.424	1249.311	343.40
18	1529.515	1253.670	343.53
19	1619.290	1258.769	343.85
20	1708.883	1264.132	344.02
21	1798.203	1269.279	344.11
22	1888.664	1276.061	344.06
23	1978.587	1285.948	344.21
24	2069.992	1298.104	344.17
25	2159.246	1309.698	344.17
26	2249.523	1315.167	344.25
27	2339.713	1319.738	344.53
28	2429.851	1324.358	344.54
29	2518.843	1330.109	344.47
30	2608.631	1339.101	344.39
31	2699.015	1346.596	344.29
32	2789.388	1354.927	344.14
33	2878.421	1364.475	344.00
34	2968.188	1373.703	344.06
35	3057.915	1375.314	344.19
36	3147.978	1369.023	344.41
37	3237.607	1357.654	344.66
38	3325.673	1346.094	344.91
39	3414.074	1338.200	345.22
40	3503.977	1331.795	345.33
41	3594.747	1328.827	345.48
42	3684.656	1327.797	345.56
43	3768.269	1325.510	345.44
44	3834.346	1322.565	345.36
45	3882.441	1317.931	345.21

46	3907.405	1312.014	345.19
47	3936.230	1305.251	345.07
48	3991.718	1297.636	344.94
49	4053.896	1293.846	344.82
50	4116.598	1291.168	344.71
51	4178.707	1286.638	344.48
52	4240.016	1282.805	344.47
53	4292.660	1284.027	344.39
54	4382.410	1287.343	344.28
55	4473.836	1293.473	344.18
56	4560.895	1292.115	344.30
57	4648.781	1293.475	344.20
58	4736.289	1297.333	344.00
59	4822.324	1298.938	344.01
60	4911.813	1291.008	343.82
61	5001.742	1288.315	343.69
62	5092.438	1287.396	343.60
63	5188.258	1287.985	343.53
64	5261.355	1287.921	343.49
65	5334.113	1287.699	343.45
66	5406.789	1288.632	343.48
67	5479.148	1290.159	343.39
68	5565.020	1290.077	343.52
69	-986.334	1289.379	343.53
70	5741.543	1287.085	343.39
71	5829.027	1282.697	343.72
72	5915.637	1274.933	343.85
73	6003.625	1266.131	343.98
74	6075.988	1263.209	343.91
75	6170.258	1259.855	344.03
76	6262.457	1258.766	344.24
77	6343.328	1255.307	344.59
78	6421.477	1252.191	344.74
79	6504.445	1250.831	344.86
80	6584.309	1251.169	345.00
81	6665.453	1249.080	345.18
82	6746.836	1248.408	345.21
83	6825.688	1250.114	345.02
84	6907.801	1249.740	345.16
85	6989.457	1253.084	345.03
86	7071.816	1254.956	345.17
87	7155.102	1258.179	345.00
88	7242.293	1257.742	345.16
89	7313.152	1255.848	345.39

90	7386.387	1252.260	345.46
91	7445.473	1253.933	345.17
92	7520.430	1246.242	345.16
93	7597.582	1238.115	345.31
94	7670.117	1237.479	345.28
95	7759.965	1237.590	345.02
96	7849.246	1239.185	344.91
97	7952.750	1242.411	344.73